Cytoarchitectonic, receptor distribution and functional connectivity analyses of the macaque frontal lobe

Lucija J. Rapan[1], Sean Froudist-Walsh[2], Meiqi Niu[1], Ting Xu[3], Ling Zhao[1], Thomas Funck[1], Xiao-Jing Wang[2], Katrin Amunts[1,5] and Nicola Palomero-Gallagher[1,4,5]

[1]Institute of Neuroscience and Medicine (INM-1), Research Centre Jülich, Jülich, Germany

[2]Center for Neural Science, New York University, New York, New York

[3]Center for the Developing Brain, Child Mind Institute, New York, New York

[4]Department of Psychiatry, Psychotherapy, and Psychosomatics, Medical Faculty, RWTH Aachen, and JARA - Translational Brain Medicine, Aachen, Germany

[5]C. & O. Vogt Institute for Brain Research, Heinrich-Heine-University, 40225 Düsseldorf, Germany

Corresponding author: Lucija J. Rapan
Institute of Neuroscience and Medicine (INM-1)
Research Centre Jülich
52425 Jülich
Germany
Phone: +49-2461-96746
Fax: +49-2461-612820
E-Mail: l.jankovic-rapan@fz-juelich.de

Keywords: prefrontal, motor, cytoarchitecture, receptor, functional connectivity, hierarchy

Abstract

Based on quantitative cyto- and receptor architectonic analyses, we identified 35 prefrontal areas and introduced a novel subdivision of Walker's areas 10, 9, 8B and 46. Statistical analysis of receptor densities revealed regional differences in lateral and ventrolateral prefrontal cortex. Since structural and functional organization of subdivisions encompassing areas 46 and 12 demonstrated significant differences in the interareal levels of α_2 receptors. Furthermore, multivariate analysis included receptor fingerprints of previously identified 16 motor areas in the same macaque brains, and revealed five clusters encompassing frontal lobe areas. Based on the functional connectivity analysis, clustered areas showed similar connectivity distribution pattern. In particular, rostrally located areas (in clusters 1-2) were characterized by bigger fingerprints, i.e., higher receptor densities, and stronger regional interconnections. Whereas, more caudal areas (in clusters 3-5) had smaller fingerprints, but showed a widespread connectivity pattern with distant cortical regions. Taken together, present study provides a comprehensive insight into the molecular structure underlying the functional organization of the cortex and, thus, reconcile discrepancies between the structural and functional hierarchical organization of the primate frontal lobe. Finally, our data are publicly available via the EBRAINS and BALSA repositories for the entire scientific community.

1 Introduction

The anterior portion of the primate frontal lobe, known as the prefrontal cortex (PFC), is a region notably involved in the higher cognitive functions (Fuster, 2008). It has been a focus region of numerous functional studies in human and monkey brains. Research involving non-human primates plays a vital role in the medical progress and scientific applications due to their close evolutionary relation to humans, but also due to ethical standards which do not allow all the vital material and data to be acquired directly from human brains (DeFelipe, 2015). In particular, macaque monkeys are the most widely used primate species in neurobiological research (Passingham, 2009). As a series of comparative analyses have shown, they share a similar basic architectonic plan to that of the human brain (Petrides et al., 2012; Petrides and Pandya, 1994; 1999; 2002; 2009).

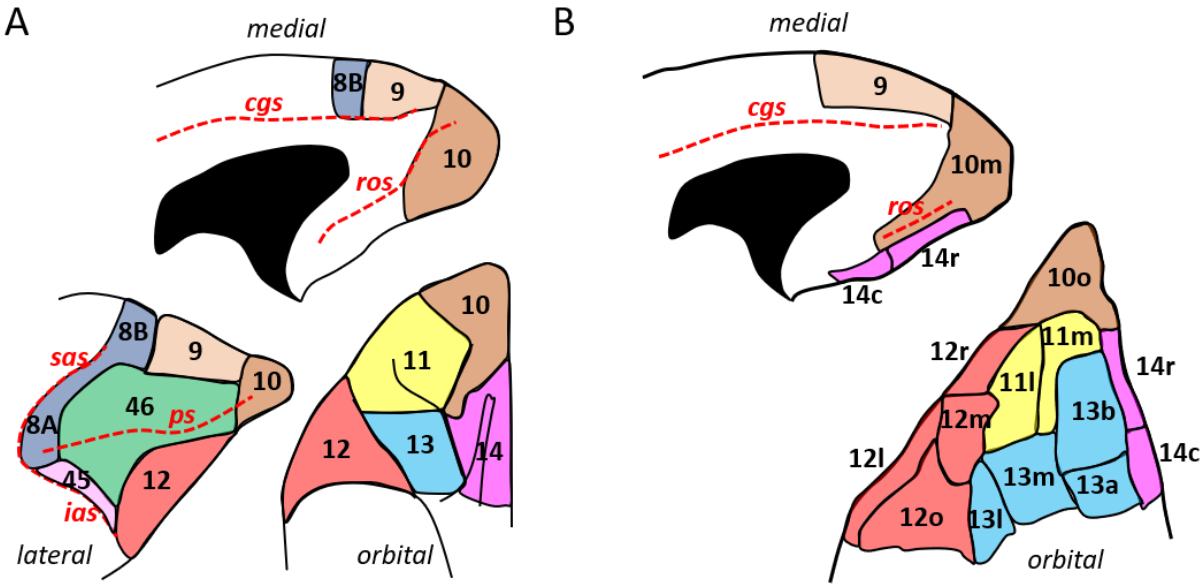

Figure 1 Schematic drawing of the medial, lateral and orbital surfaces of the macaque prefrontal cortex depicting parcellations according to A) Walker (1940), and B) Carmichael and Price (1994). Macroanatomical landmarks are marked with red dashed lines; *cgs* – cingulate sulcus; *ias* – inferior arcuate sulcus; *ps* – principal sulcus; *ros* – rostral orbital sulcus; *sas* – superior arcuate sulcus.

Early cytoarchitectonic studies of the monkey cerebral cortex encountered the same issues and limitations as those of the human cortex with regard to both methodological and nomenclatural issues. Methodological limitations include small

sample size, usually single of only few cases, analysis of a single modality, and a subjective approach to detection of cortical borders due to their identification by pure visual inspection. The nomenclature issue seems to be problematic as well, since it doesn't only affect comparability between different maps, but also translational analyses and identification of the homolog areas in the human brain. Brodmann's (Brodmann, 1909) map of the human brain is one of the most famous parcellation schemes and many modern neuroanatomists still refer to it. However his map of the monkey (Cercopithecus) cortex (Brodmann, 1905) did not accomplish the same success. The most influential cytoarchitectonic map of the monkey prefrontal cortex was published by Walker (Walker, 1940), who used the numerical nomenclature introduced by Brodmann in his human brain map, although he did not compare the cytoarchitecture of the human and macaque monkey prefrontal regions in detail. Walker (Walker, 1940) labelled the frontopolar cortex of the monkey as area 10 and added areas 46 and 45 (**Fig. 1**), which were not indicated in Brodmann's map of the monkey frontal cortex. Thus, Walker's (Walker, 1940) parcellation scheme became the basis for future microparcellation and anatomical-connectional studies with anterograde and retrograde tracers, as well as in physiological microstimulation studies (e.g., Barbas and Pandya, 1989; Carmichael and Price, 1996; Morecraft et al., 2012; Petrides and Pandya, 2006). This research led to a "golden era" of experimental neuroanatomy with various research groups focused on the analysis of a specific region of interest (ROI) in the monkey brain, e.g., the orbitofrontal (Barbas, 2007; Carmichael and Price, 1994), dorsolateral prefrontal (Petrides 2005; Petrides and Pandya 1999; Preuss and Goldman-Rakic 1991), and ventrolateral prefrontal cortex (Gerbella et al. 2007; Petrides and Pandya 2002; Preuss and Goldman-Rakic 1991).

The development of a quantitative approach to the analysis of cytoarchitecture in entire human brain sections enabled statistical validation of visually detectable cortical borders and thus an objective approach to brain mapping (Schleicher et al. 2009; Schleicher and Zilles 1990). Furthermore, an implementation of the analyses, which include multiple architectonical modalities, also enabled a more comprehensive characterization of the cortical parcellation. Specifically, quantitative *in vitro* multi-receptor autoradiography has been revealed as powerful tool to describe important aspects of the brain's molecular and functional organization, since neurotransmitters and their receptors are known to play an important role in a signalling process (Impieri

et al. 2019; Palomero-Gallagher et al. 2009; Zilles et al. 2002). Concentrations of receptors for classical neurotransmitter systems vary between different cortical areas, hence, the area-specific balance of different receptor types ("receptor fingerprint") subserves its distinct functional properties. Quantification of heterogeneous receptors distribution throughout the cerebral cortex enables the identification and characterization of principal subdivisions such as primary sensory, primary motor, and hierarchically higher sensory or multimodal areas (Palomero-Gallagher and Zilles 2019; Zilles and Palomero-Gallagher 2017). Multivariate analyses of the receptor fingerprints demonstrates, not only structural, but also functionally significant clustering of cortical areas (Zilles and Amunts, 2009). Therefore, this multimodal approach to cortical mapping provides detailed insights into the relationship between cytoarchitecture (which highlights the microstructural heterogeneity) and neurotransmitter receptor distributions (which emphasize the molecular aspects of signal processing) in the healthy nonhuman primate brain. It constitutes an objective and reliable tool which provides basic information of functional networks and precisely defined anatomical structures. Finally, combined cyto- and receptor architectonic analyses can be used to facilitate establishment of homologies between human and non-human primate brains (Impieri et al. 2019; Niu et al. 2021; Rapan, Niu, et al. 2021), since the organizational principles of receptor distribution patterns throughout primary sensory areas were found to be conserved in eutherian mammals (Zilles and N. Palomero-Gallagher 2017).

Recently, *in-vivo* neuroimaging of the non-human primates has been advancing rapidly due to increased collaboration and data sharing (Milham et al. 2018, 2020). Primate imaging is a promising approach to link between precise electrophysiological and neuroanatomical studies of the cortex and distinct functional networks observed in humans. However, integration of neuroimaging data with high-quality postmortem anatomical data has been problematic, since these results have not been conveyed in a common coordinate space. Also, macaque maps, that are currently available to the *in-vivo* neuroimaging researchers, do not contain information about receptor densities. Such information enables identification of the chemical underpinnings of functional activity and connectivity observed in-vivo.

The aim of the present study is to define prefrontal areas based a quantitative cyto- and receptor architectonic approach, combined with a functional connectivity analysis of identified areas, to create statistically testable parcellation that can be transformed into stereotaxic space. Furthermore, to reveal (dis)similarities in the shape and/or size of receptor fingerprints across the macaque frontal lobe, a multivariate analysis was conducted, which include not only receptor fingerprints of prefrontal areas, but also fingerprints of previously identified (pre)motor subdivisions (Rapan, Froudist-Walsh, et al. 2021). Thus, it will be interesting to discuss how hierarchical cluster analysis of frontal areas (based on receptor architectonic data) resonates with results from functional connectivity analysis. All data are made available to the community in standard Yerkes 19 surface via the EBRAINS repository of the Human Brain Project and the BALSA platform.

2 Material and methods

2.1 Tissue processing

Both hemispheres of an adult macaque monkey (*Macaca mulatta*; male; brain ID DP1; 8 years; obtained as a gift from Professor Deepak N. Pandya) were used for cytoarchitectonic analysis in histological sections of a paraffin embedded brain. Sodium pentobarbital was applied to deeply anesthetize the monkey, followed by a transcardial perfusion with cold saline and then 10% buffered formalin. The brain was removed and stored in a buffered formalin solution until further processing.

The brains of three adult macaques (*Macaca fascicularis*; males; brain IDs 11530, 11539, 11543; 6±1 years of age; obtained from Covance Laboratories, Münster, Germany) were processed for both, cyto- and receptor architectonic analysis. Monkeys were sacrificed by means of a lethal intravenous injection of sodium pentobarbital. However, since receptor proteins are delicate in nature, only unfixed, deep frozen tissue can be used for receptor autoradiography (Herkenham et al. 1990; Zilles et al. 2002). Thus, the brains were immediately removed from the skull together with meninges and blood vessels, to avoid further damage of superficial layers. The cerebellum, together with the brainstem, was separated from the rest of the brain. Each hemisphere was further divided into an anterior and a posterior slab at the level of the most caudal portion of the central sulcus. In the present study, we examined all left hemispheres, except for brain 11539, where both hemispheres were analyzed. The slabs were carefully placed on an aluminum plate to avoid any further deformation and slowly introduced into N-methylbutane (isopentane) at -40°C, where they were left for 10 - 15 minutes. Frozen slabs were stored in air-tight plastic bags at -80°C until used for sectioning. Animal care was provided in accordance with the NIH Guide for Care and Use of Laboratory Animals, and the European local Committee, and complied with the European Communities Council Directive.

2.2 Identification of cortical areas

Starting point for the present parcellation was visual and microscopic inspection of our sectioned brains and previously published cytoarchitectonic literature of the macaque

prefrontal cortex. Specifically, analysis of the orbitofrontal cortex and ventrolateral areas 10, 11, 12, 13 and 14 was based on the parcellation scheme and nomenclature proposed by Carmichael and Price (Carmichael and Price 1994). Nomenclature of prefrontal areas 9, 8B, 8A, 46 and 45 is based on Walker's (Walker 1940) original parcellation scheme, though integrating later modifications (Morecraft et al. 2012; Petrides 2005; Preuss and Goldman-Rakic 1991).

Since the identification of neighboring areas, based on a pure visual inspection, has previously resulted in maps that differ in terms of number, localization and shape of cortical areas, in the present study we applied a quantitative and statistically testable approach to test the localization and existence of all visually identified cytoarchitectonic borders (Schleicher et al. 2000, 2009; Zilles et al. 2002). Furthermore, cytoarchitectonically identified areas were further confirmed by differences in the regional and laminar distribution patterns of multiple neurotransmitter receptors, i.e., by differences in receptor architecture.

2.3 Processing postmortem brain and analysis of cytoarchitecture

DP1 brain was dehydrated in ascending graded alcohols (70% to 100% propanol), completed by a step-in chloroform. The brain was then embedded in paraffin and serially cut in the coronal plane with a large-scale microtome, resulting in 3305 20-µm-thick whole-brain sections. Every fifth section was mounted on gelatine coated slides. Paraffin was removed and sections were rehydrated by a two-step washing (each of 10 minutes) with Xem-200 („Xylol-Ersatz-Medium", Vogel, Diatec Labortechnik GmbH) followed by graded washes in alcohol (10 minutes each in 100%, 96% and 70% propanol) and finally a rinse in a pure water.

Sections were stained with a modified silver method (Merker 1983; Uylings, Zilles, and Rajkowska 1999), which provides a high contrast between cell bodies and neuropil. In short, sections were pretreated 4 hours in 4% formic acid, then overnight in a 10% formic acid/30% peroxide solution. Sections were thoroughly washed, immersed twice for 5 minutes in 1% acetic acid, placed in a physical developer under constant movement until they become greyish, and then further developed with constant monitoring under the microscope until cell bodies were dark grey/black. The developer was prepared immediately before use by adding 30ml of stock solution B (2g $AgNO_3$,

2g NH_4NO_3 and 10g SiO_2•12WO_3•26H_2O dissolved in 1l distilled water; stored at room temperature) and then 70ml of stock solution C (2g $AgNO_3$, 2g NH_4NO_3, 10g SiO_2•12WO_3•26H_2O and 7.3ml of a 37% formaldehyde solution dissolved in 1l distilled water; stored at room temperature) to 100 ml of stock solution A (50g Na_2CO_3 dissolved in 1l distilled water; stored at 4°C) under vigorous stirring, and development was terminated by two 5 minute washes in 1% acetic acid. Sections were then fixed 5 minutes in a T-Max fixative (Kodak, 2 parts of T-Max and 7 parts of distilled water), dehydrated in ascending grades of alcohol (70%, 96%, 100%) for 5 minutes in each dilution followed by two 5-minute immersions in xylene before coverslipping with DePex mounting medium.

Regions of interest (ROI) were scanned with a light microscope (Axioplan 2 imaging, ZEISS, Germany) equipped with a motor-operated stage controlled by the KS400® and Axiovision (Zeiss, Germany) image analyzing systems applying a 6.3 x 1.25 objective (Planapo®, Zeiss, Germany) and a CCD camera (Axiocam MRm, ZEISS, Germany). Digitalized images are produced by stitching individual frames of 524 x 524 µm in size, 512 x 512-pixel spatial resolution, and in-plane resolution of 1 µm per pixel and eight-bit grey resolution.

The quantitative approach to cytoarchitectonic analysis relies on the volume fraction of cell bodies as estimated by the grey level index (GLI) in square measuring field, which is of fixed size (Schleicher et al. 2009). For each identified area, GLI images were generated from three neighboring sections in the rostro-caudal direction. GLI profiles of each ROI were extracted perpendicularly to the cortical surface by measuring the changes in grey values in the GLI images along equidistant traverses to quantify the laminar pattern characteristic of a cortical area (Schleicher et al. 2009). Therefore, profiles were defined between an outer contour, drawn along the border between layers I and II, and an inner contour, at the border between layer VI and the white matter (for details see Palomero-Gallagher and Zilles 2019; Zilles et al. 2002). The shape of the profile can be parametrized, i.e., presented as a frequency distribution of ten features, which quantitatively describe the laminar distribution of the volume fraction of the cell bodies, constitute a feature vector of each profile, and can be standardized using different scales to set equal weight to each of the values used for multivariate analyses (Schleicher et al. 2005; Zilles et al. 2002).

Assuming that each area has a distinctive laminar pattern, areal borders would be located at the transition of the laminar pattern of one area to that of the neighboring area. Therefore, the Mahalanobis distance (MD; Mahalanobis et al. 1949) was applied to quantify differences in the shape of two profiles and enable detection of the position of borders (Schleicher et al. 2005; Zilles et al. 2002). Adjacent profiles were grouped into blocks to operate as a sliding widow shifting along the cortical ribbon by the distance of one profile, whereby the MD between immediately adjacent blocks was calculated and plotted as a distance function for all block positions. This process was repeated, but with systematically increasing block sizes from 10 to 24 profiles in order to control the stability of a distance function that changes with a number of profiles in a block. If two blocks belong to the same area, MD values are expected to be small, since their laminar pattern coded by the profiles being compared is similar. To confirm and accept MD maxima as architectonically relevant borders, we applied Hotelling's T^2 test in combination with a Bonferroni adjustment of the P-values for multiple comparisons (Schleicher et al. 2005; Zilles et al. 2002). Finally, main maxima identified with numerous block sizes in one histological section were evaluated by comparison with corresponding maxima in three consecutive sections to exclude biologically meaningless maxima which may be caused by artifacts (e.g., ruptures, folds) or local discontinues in microstructure due to blood vessels or untypical cell clusters.

In order to visualize the relationship between identified areas and macroanatomic landmarks we created a 2D flat map and a 3D model of the macaque prefrontal cortex. For the 2D flat map we generated a framework based on the sulcal anatomy of the DP1 brain, whereby every 40th section was represented as a line with indentations representing characteristic sulci and dimples and cytoarchitectonic borders were positioned relative to the corresponding macroscopic landmarks. Thus, the ensuing flat map enables visualization of borders even when they are located inside sulci (for more details see (Rapan, Froudist-Walsh, et al. 2021). To compute the 3D model, the positions of borders relative to macroanatomic landmarks (i.e., the fundus of sulci or dimples and the apex of gyri) were transferred by means of the connectome workbench software (https://www.humanconnectome.org/software/connectome-workbench) to the surface representation of the Yerkes19 template brain (Donahue et al. 2016), thus also bringing our parcellation scheme into stereotaxic space.

2.4 Processing unfixed brains and analysis of receptor architecture

We used quantitative *in vitro* receptor autoradiography to visualize binding sites of native receptors expressed on the cell membrane of neurons and glia cells. The advantage of this method is that it can be carried out on a large number of large sections, alongside the possibility of precise quantification and a high specificity (Palomero-Gallagher and Zilles 2018; Zilles et al. 2002).

Unfixed frozen slabs were serially sectioned in the coronal plane using a cryostat at -20°C, into 20µm-thick sections, which were thaw-mounted on gelatin-coated glass slides. Sections were left to air dry and stored overnight in air-tight plastic bags at -20°C. Serial sections were used for the visualization of 14 distinct receptors types, i.e., for glutamate (AMPA, kainate, NMDA), gamma-aminobutyric acid - GABA ($GABA_A$, $GABA_B$, $GABA_A$ associated benzodiazepine binding sites-BZ), acetylcholine (M_1, M_2, M_3), noradrenalin (α_1, α_2), serotonin ($5HT_{1A}$, $5HT_2$) and dopamine (D_1), as well as for the visualization of cell bodies (see previous section) using previously published protocols (Palomero-Gallagher et al. 2009; Zilles et al. 2002); see **Tab. 1**), in three subsequent steps: a preincubation, a main incubation and a rinsing step. The preincubation is carried out to rehydrate sections and to remove endogenous ligands that could block the binding sites. During the main incubation, two parallel experiments are conducted to test the specific binding ability of each ligand. In one, sections were incubated in a buffer solution with tritiated ligand to identify total binding of each ligand type. In the second, neighboring sections were incubated in buffer solution containing the tritiated ligand and a receptor type-specific displacer in a 1000-fold higher concentration to visualize non-specific binding of the same ligand. Finally, the difference between total and non-specific binding demonstrates the specific binding ability for each ligand. In this study, specificity of ligands used resulted in a non-specific binding of less than 5% of the total binding. In the rinsing step, the binding process was stopped and free ligand and buffer salts removed. Air-dried, radioactive sections were then co-exposed with plastic tritium-standards (calibrated for protein density, and with known increasing concentrations of radioactivity) against β radiation-sensitive films (Hyperfilm®, Amersham) for 4-18 weeks depending on the analyzed ligand. A densitometric analysis (Palomero-Gallagher and Zilles 2018; Zilles et al. 2002) was

carried to measure binding site concentrations in the ensuing receptor autoradiographs.

Autoradiographs were digitized with an image analysis system consisting of a source of homogenous light and a CCD-camera (Axiocam MRm, Zeiss, Germany) with an S-Orthoplanar 60-mm macro lens (Zeiss, Germany) corrected for geometric distortions, connected to the image acquisition and processing system Axiovision (Zeiss, Germany). Spatial resolution of the resulting images was 3000x4000 pixels; 8-bit gray value resolution). The gray values of the digitized autoradiographs code for concentrations of radioactivity. To transform gray values into fmol binding sites/mg protein, a linearization of the digitized autoradiographs had to be performed in a two-steps process, carried out with in house developed Matlab (The MathWorks, Inc. Natrick, MA) scripts. First, the gray value images of the plastic tritium-standards were used to compute the calibration curve, which defines the non-linear relationship between gray values and concentrations of radioactivity. Then radioactivity concentration R was then converted to binding site concentration C_b in fmol/mg protein using following equation (1):

$$C_b = \frac{R}{E \cdot B \cdot W_b \cdot S_a} \cdot \frac{K_D + L}{L} \qquad (1)$$

where E is the efficiency of the scintillation counter used to determine the amount of radioactivity in the incubation buffer (depends on the actual counter), B is the number of decays per unit of time and radioactivity (Ci/min), W_b the protein weight of a standard (mg), S_a the specific activity of the ligand (Ci/mmol), K_D the dissociation constant of the ligand (nM), and L the free concentration of the ligand during incubation (nM) (Palomero-Gallagher and Zilles 2018; Zilles et al. 2002). For visualization purposes, a linear contrast enhancement and pseudo-color coding of autoradiographs was applied, using a specter of eleven colors with equally spaced density ranges (red color for highest and black for lowest receptor concentration levels).

Measurement of receptor binding sites was performed by computing the surface below receptor profiles, which were extracted from the linearized autoradiographs using in house developed scripts for Matlab (The MathWorks, Inc. Natrick, MA) in a manner comparable to the procedure described above for GLI profiles. However, for receptor profiles the outer contour line was defined following the pial surface, and not the border between layers I and II. Thus, for each of the four hemispheres examined, mean

341 **Table 1** Receptor labelling protocols

Transmitter	Receptor	Ligand (nM)	Property	Displacer (μM)	Incubation buffer	Pre-incubation	Main incubation	Final rinsing
Glutamate	AMPA	[^{3}H]-AMPA (10)	Agonist	Quisqualate (10)	50mM Tris-acetate (pH 7.2) [+ 100 mM KSCN]*	3x 10 min, 4° C	45 min, 4° C	1) 4x 4sec 2) Acetone/glutaraldehyde (100 ml + 2,5 ml), 2x 2sec, 4° C
	NMDA	[^{3}H]-MK-801 (3.3)	Antagonist	(+)MK-801 (100)	50mM Tris-acetate (pH 7.2) + 50 μM glutamate [+30 μM glycine + 50 μM spermidine]*	15 min, 4° C	60 min, 22 ° C	1) 2x 5min, 4° C 2) distilled water, 1x 22 ° C
	KAINATE	[^{3}H]-Kainate (9.4)	Agonist	SYM 2081 (100)	50mM Tris-acetate (pH 7.1) [+10 mM Ca^{2+}-acetate]*	3x 10 min, 4° C	45 min, 4° C	1) 3x 4sec 2) Acetone/glutaraldehyde (100 ml + 2,5 ml), 2x 2sec, 22 ° C
GABA	$GABA_A$	[^{3}H]-Muscimol (7.7)	Agonist	GABA (10)	50mM Tris-citrate (pH 7.0)	3 x 5 min, 4° C	40 min, 4° C	1) 3x 3 sec, 4° C 2) distilled water, 1x 22 ° C
	$GABA_B$	[^{3}H]-CGP 54626 (2)	Antagonist	CGP 55845 (100)	50mM Tris-HCl (pH 7.2) + 2,5 mM $CaCl_2$	3 x 5 min, 4° C	60 min, 4° C	1) 3x 2 sec, 4° C 2) distilled water, 1x 22 ° C
	Bz	[^{3}H]-Flumazenil (1)	Antagonist	Clonazepam (2)	170 mM Tris-HCl (pH 7.4)	15 min, 4° C	60 min, 4° C	1) 2x 1 min, 4° C 2) distilled water, 1x 22 ° C
Acetylcholine	M_1	[^{3}H]-Pirenzepine (1)	Antagonist	Pirenzepine (2)	Modified Krebs buffer (pH 7.4)	15 min, 4° C	60 min, 4° C	1) 2x 1 min, 4° C 2) distilled water, 1 x 22 ° C
	M_2	[^{3}H]-Oxotremorine-M (1.7)	Agonist	Carbachol (10)	20 mM HEPES-Tris (pH 7.5) + 10 mM $MgCl_2$+ 300 nM Pirenzepine	20 min, 22° C	60 min, 22° C	1) 2x 2 min, 4° C 2) distilled water, 1 x 22 ° C
	M_3	[^{3}H]-4-DAMP (1)	Antagonist	Atropine sulfate (10)	50 mM Tris-HCl (pH 7.4) + 0.1 mM PSMF + 1mM EDTA	15 min, 22° C	45 min, 22° C	1) 2x 5 min, 4° C 2) distilled water, 1 x 22 ° C
Noradrenaline	α_1	[^{3}H]-Prazosin (0.2)	Antagonist	Phentolamine Mesylate	50mM Na/K-phosphate buffer (pH 7.4)	15 min, 22° C	60 min, 22° C	1) 2x 5 min, 4° C 2) distilled water, 1 x 22 ° C

				(10)				
	α_2	[^{3}H]-UK 14,304 (0.64)	Agonist	Phentolamine Mesylate (10)	50 mM Tris-HCl + 100 μM $MnCl_2$ (pH 7.7)	15 min, 22° C	90 min, 22° C	1) 5 min, 4° C 2) distilled water, 1 x 22 ° C
Serotonin	5-HT_{1A}	[^{3}H]-8-OH-DPAT (1)	Agonist	5-Hydroxy-tryptamine, (1)	170 mM Tris-HCl (pH 7.4) [+4 mM $CaCl_2$ + 0.01% ascorbate]*	30 min, 22° C	60 min, 22° C	1) 5 min, 4° C 2) distilled water, 3 x 22 ° C
	5-HT_2	[^{3}H]-Ketanserin (1.14)	Antagonist	Mianserin (10)	170 mM Tris-HCl (pH 7.7)	30 min, 22° C	120 min, 22° C	1) 2x 10 min, 4° C 2) distilled water, 3 x 22 ° C

342 * only included in the main incubation, ** only included in the preincubation

343

densities (i.e., averaged over all cortical layers) of each of the 14 different receptors in 33 of the 35 cytoarchitectonically defined areas were calculated. Due to technical limitations associated with the cutting angle of the coronal sections, it was not possible to measure densities in areas 13a and 14c. The precise sampling for the measurements of each cytoarchitectonically defined area was verified by aligning autoradiographs with defined cytoarchitectonic borders in neighboring silver-staining sections in the corresponding brain processed for the receptor architectonic analysis. For each of the examined areas and their subdivisions, the mean densities of all receptors averaged over all four hemispheres in that area were then visualized simultaneously as “receptor fingerprints”, i.e., as polar coordinate plots which reveal the specific balance of different receptor types within a cytoarchitectonic entity (Zilles et al. 2002).

2.4.1 Statistical analysis of the receptor densities

To determine if there were significant differences in receptor architecture between paired areas (in particular our analysis was focused on directly bordering areas within the prefrontal region), stepwise linear mixed-effect models were performed. A z-score normalization was performed for each receptor separately to ensure an equal weighting of all receptors in subsequent statistical analyses. All statistical analyses were conducted using the R programming language (version 3.6.3.; Team, 2013).

We conducted a statistical testing which included three levels. In the first level, an omnibus test was caried out to determine whether there were differences across all regions when all receptor types are considered simultaneously (Equation 2). The model consists of fixed effects for area and receptor type, and hemisphere was set as a random factor.

$$D_{a,r,h} = \alpha_0 + \alpha_1 A_a + \alpha_2 R_r + \alpha_3 A_a R_r + \beta_1 H_h \qquad (2),$$

where D represents the receptor density, A the prefrontal area, R the receptor type and H the hemisphere.

If the interaction effect between area and receptor type at first level of testing was found to be significant, a second level of simple effect tests was applied for each receptor separately to determine whether there were significant differences across all areas for each receptor type. The *p*-values were corrected for multiple comparison

using the Benjamini-Hochberg correction for false-discovery rate (Benjamini and Hochberg 1995).

Finally, the third level post hoc tests were used to identify the paired areas driving the statistical difference in the second level tests. For each receptor type, 528 post hoc tests were performed. To correct for multiple comparisons in the third step tests, we performed the false-discovery rate correction (Benjamini and Hochberg 1995) separately for each receptor type (i.e., p-values were corrected for 528 comparisons per receptor type).

2.5 Visualization and analysis of functional connectivity

All datasets used here for analysis are openly available sources from the recently established PRIME-DE (http://fcon_1000.projects.nitrc.org/indi/indiPRIME.html) (Milham et al. 2018). Functional data were preprocessed using the Human Connectome Project-style pipeline for Nonhuman Primate as described previously (Autio et al. 2020; Xu et al. 2019). For each macaque, the structural preprocessing includes denoising, skull-stripping, tissue segmentation, surface reconstruction and surface registration to align to Yerkes19 macaque surface template (Donahue et al. 2016). The functional preprocessing includes temporal compressing, motion, correction, global mean scaling, nuisance regression (Friston's 24 motion parameters, white matter, cerebrospinal fluid), band-pass filtering (0.01–0.1 Hz), and linear and quadratic detrending. The preprocessed data then were co-registered to the anatomy T1 and projected to the middle cortical surface. Finally, the data were smoothed (FWHM = 3 mm) on the high-resolution native surface, aligned and down resampled to a 10k surface (10,242 vertices per hemisphere). The preprocessed BOLD activity timecourses for each monkey brain were demeaned and then concatenated in time. This enabled us to estimate the group functional connectivity maps for each seed region in a single analysis.

The connectivity of each identified prefrontal areas was investigated in regard to 76 cortical areas, previously defined by Palomero-Gallagher group, i.e., 16 areas of (pre)motor cortex, 15 areas of cingulate cortex, 6 areas of somatosensory cortex, 23 areas of parietal cortex and 16 areas of occipital cortex (Impieri et al. 2019; Niu et al. 2021; Rapan, Froudist-Walsh, et al. 2021; Rapan, Niu, et al. 2021). A representative

timecourse was calculated for each of the 35 prefrontal areas and the 76 (pre)motor, cingulate, somatosensory, parietal and occipital areas, giving 111 areas in total. For each of the 111 areas, a principal components analysis was performed on activity across all vertices within the area, where the first principal component was taken as the representative activity timecourse for each area.

The representative timecourses of each of the 35 prefrontal areas were used as seeds for functional connectivity analysis. Since they were correlated with the activity timecourses for each vertex on the surface using a Pearson correlation. A Fisher's r-to-z transformation was then applied to each of the correlation coefficients. This was visualized on the Yerkes19 cortical surface. Code used for the implementation and visualization of the functional connectivity analysis has been made publicly available (https://github.com/seanfw/macaque-pfc-func-conn).

2.6 Multivariate analyses of receptor fingerprints

To reveal structure-function relationship between areas of the frontal lobe, we not only used receptor fingerprints of the here identified 33 prefrontal areas (except areas 13a and 14c, see above), but also included those of previously identified 16 motor and premotor areas (Rapan, Froudist-Walsh, et al. 2021). Receptor densities were extracted from the same macaque brains. Hierarchical clustering and principal component analyses were carried out to enable grouping of areas based on receptor architectonic similarities (Palomero-Gallagher et al. 2009). We used a receptor fingerprint of each subdivision as a feature vector characterizing the area of interest. The Euclidean distance, which takes into account difference in the size and shape of fingerprint, was applied as a measure of (dis)similarities between receptor fingerprints.

Before any statistical analysis was conducted, it was necessary to normalize all absolute receptor values due to large differences in absolute densities across receptor types. Receptors with high absolute density values (i.e., GABAergic receptors), would dominate the calculation of the Euclidean distance between areas, as well as of the principal component analysis, cancelling intended multimodal approach in the present analysis. Whereas normalized receptor values enable for each receptor type to contribute with equal significance to the statistical analyses. Here, z-scores calculation was applied, since this approach maintains the relative differences in receptor

densities among areas, i.e., the mean density of a given receptor across all examined areas was subtracted from the mean density of the same receptor in a defined area and obtained value was divided by the standard deviation of that receptor over all areas. The Ward linkage algorithm was chosen as the linkage method because, in combination with the Euclidean distances. It yielded a higher cophenetic correlation coefficient than any other combination of alternative linkage methods and measurements of (dis)similarity. The cophenetic correlation coefficient quantifies how well the dendrogram represents the true, multidimensional distances within the input data. The k-means analysis was applied to identify the highest acceptable number of clusters and confirmed by the k-means permutation test.

3 Results

3.1 Cytoarchitectonic analysis

The systematic identification of 35 prefrontal areas of every 20th coronal histological section of the brain DP1, as well as silver body-stained sections of brains 11530, 11539, 11543, resulted in a map containing the location and extent of all areas, and their relationships with macroanatomical landmarks is clearly depicted in **Figure 2**.

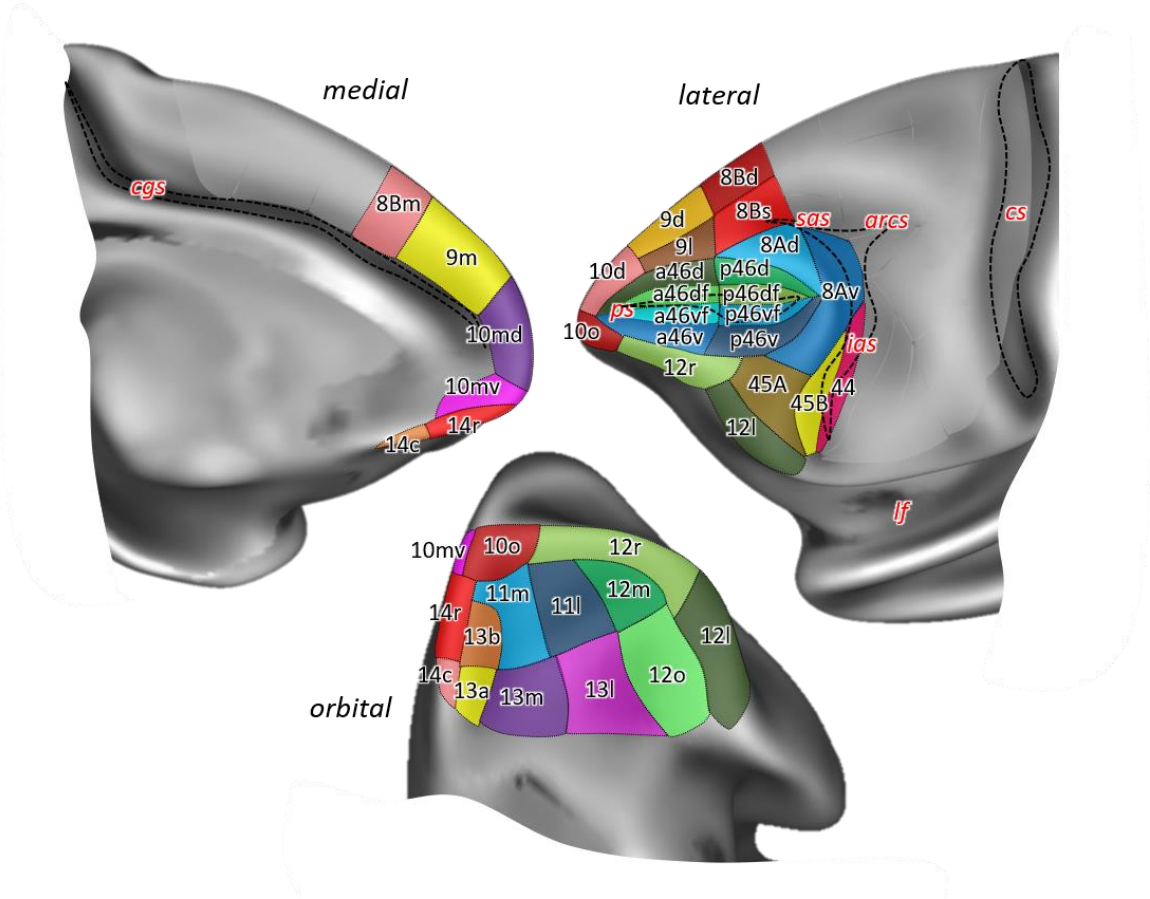

Figure 2 Position and extent of the prefrontal areas on the medial, lateral and orbital views of the Yerkes19 surface. The files with the parcellation scheme are available via EBRAINS platform of the Human Brain Project (https://search.kg.ebrains.eu/instances/Project/e39a0407-a98a-480e-9c63-4a2225ddfbe4) and the BALSA neuroimaging site (https//balsa.wustl.edu/XXXXX). Macroanatomical landmarks are marked in red letters, while black dashed lines mark fundus of sulci; *arcs* – spur of the arcuate sulcus; *cgs* – cingulate sulcus; *cs* – central sulcus; *ias* – inferior arcuate sulcus; *lf* – lateral fissure; *ps* – principal sulcus; *sas* – superior arcuate sulcus.

Additionally, **Supplementary Figures 1 and 2** show the characteristic macroanatomical features (i.e., dimples and sulci) of the macaque frontal lobe, used here to delineate our region of interest. The prefrontal cortex (PFC) is separated from the motor areas by the well-defined arcuate sulcus (*arcs*), which branches dorsally into the superior arcuate sulcus (*sas*) and ventrally into the inferior arcuate sulcus (*ias*), thus forming a letter Y on the lateral surface of the hemisphere. Ventrally, PFC is limited by the lateral fissure (*lf*), which represents the border with temporal areas, whereas on the medial surface, the cingulate sulcus (*cgs*) separates PFC from the limbic cortex. Another prominent feature on the lateral aspect of the PFC in the macaque monkey brain is the well-defined principal sulcus (*ps*), which starts rostrally within the frontopolar region and ends caudally within the arcuate convexity (**Supp. Fig. 2**). These prominent macroanatomical features are recognizable in both macaque species (*Macaca mulatta* – brain ID DP1, and *Macaca fascicularis* – brain IDs rh11530, rh11539 and rh11543) studied here, as well as on the Yerkes19 surface used as a template for our 3D map (**Supp. Fig. 1**).

In contrast, the orbitofrontal surface is characterized by a more variable sulcal pattern, comprised of lateral (*lorb*) and medial orbital sulcus (*morb*). In brain DP1 they are shown as two parallel, sagittally oriented sulci in the left hemisphere, while in the right hemisphere these sulci are partially connected forming a letter H (**Supp. Fig. 2**). Though not as deep as sulci, there are several dimples within the PFC, e.g., the anterior dimple (*aspd*) in its rostral part, and more caudally, the posterior dimple (*pspd*) in the dorsal PFC. Finally, ventral to the *ps* the inferior principal dimple (*ipd*) was recognizable only in the right hemisphere of DP1. The appearance of these dimples in three *M. fascicularis* brains is rather variable. Since the Yerkes19 atlas is based on structural MRI scans of 19 adult macaques, these dimples are missing from its surface (**Supp. Fig. 1**).

As specified in the Material and Methods section, previously published architectonic literature and nomenclature conventions were used as a starting point for the cytoarchitectonic analysis. All borders detected by visual inspection were then tested by image analysis and statistical validation, and the most distinguishing cytoarchitectonic features of the identified subdivisions belonging to the same area are summarized in **Table 2**.

499 **Table 2** Prominent cytoarchitectonic features highlighted for all 35 identified prefrontal areas.

Area	Layer IV	Cytoarchitecture	
10d	granular	small-size pyramids in III/V; dense granular layers II/IV	
10md		wide, pale layer V	
10mv		prominent middle-size pyramids in V	
10o		prominent layer II	
14r	dysgranular	well-developed layer II; columnar pattern in IV-V	
14c	agranular	pale layer III	
11m	granular	sublamination of V (Va/Vb); cell clusters in Va	
11l		sublamination of V (Va/Vb)	
13b	granular	columnar pattern in IV-V	
13a		sublamination of V (Va/Vb)	
13m	dysgranular	sublamination of V (Va/Vb); layer Va wider than Vb	
13l		sublamination of V (Va/Vb); both layers of comparable width	
12r	dysgranular	no sublamination of V	
12m	granular	sublamination of V (Va/Vb)	
12l		sublamination of V (Va/Vb)	
12o	dysgranula	no sublamination of V	
9m	granular	sublamination of V (Va/Vb)	
9d		gradient in cell-size within III; sublamination of V (Va/Vb); pale layer Vb is wider in 9d than 9l	
9l		gradient in cell-size within III; sublamination of V (Va/Vb)	
a46d	granular	scattered middle-sized pyramids in upper layer V	well-developed layer II
a46df			scattered middle-sized pyramids in lower layer III
a46vf			scattered middle-sized pyramids in layer III
a46v			prominent layer II, but not as in a46d
p46d	granular	cells more uniform in size throughout the cortex	well-developed layer II; densely packed cells in layer III
p46df			densely packed cells in layer III; scattered middle-sized pyramids in lower layer III
p46vf			scattered middle-sized pyramids in layer III

p46v		prominent layer II, but not as in p46d
8Bm	dysgranular	layer VI pale compared to dorsal subdivisions
8Bd		dark, prominent layer II
8Bs		small size pyramids in III and V compared to 8Bd
8Ad	granular	upper layer III pale
8Av		lower layer III pale; highly granular cortex
45A	granular	middle-sized pyramids in layer III
45B		layer IV less developed
44	dysgranular	few larger pyramids scattered in layer V

Frontopolar and orbital areas. The most rostral tip of the primate brain is occupied by the so-called frontal polar region (largely occupied by Walker's area 10), where we identified four distinct areas (**Figs. 2 and 3A**): i.e., area 10d (dorsal) located on the dorsolateral surface of the frontal pole, areas 10mv (medio-ventral) and 10md (medio-dorsal) on its medial surface, and 10o (orbital) on its most ventral aspect, occupying the rostral portion of the ventromedial gyrus. With a well-developed layer IV, this entire region represents a highly granular cortex, with slight differences in its appearance between the four defined areas, whereby medial areas 10md and 10mv show a slightly thinner layer IV compared to adjacent areas 10d and 10o, respectively (**Fig. 3B**). Unlike the rest of area 10 subdivisions, area 10d has more densely packed layers II and V, with small-sized pyramids, whereas in the medial (10md/10mv) and orbital (10o) portions characteristic larger pyramids could be recognized in the upper part of layer V. 10mv can be distinguished from the neighbouring areas 10md and 10o by the much thinner appearance of its layer V. Additionally, the border between layers II and III is clearly visible in area 10o, but not in 10mv (**Fig. 3B**). **Figure 3C** shows the result of the statistical validation of these newly defined subdivisions of area 10, as well as of the corresponding borders with adjacent areas.

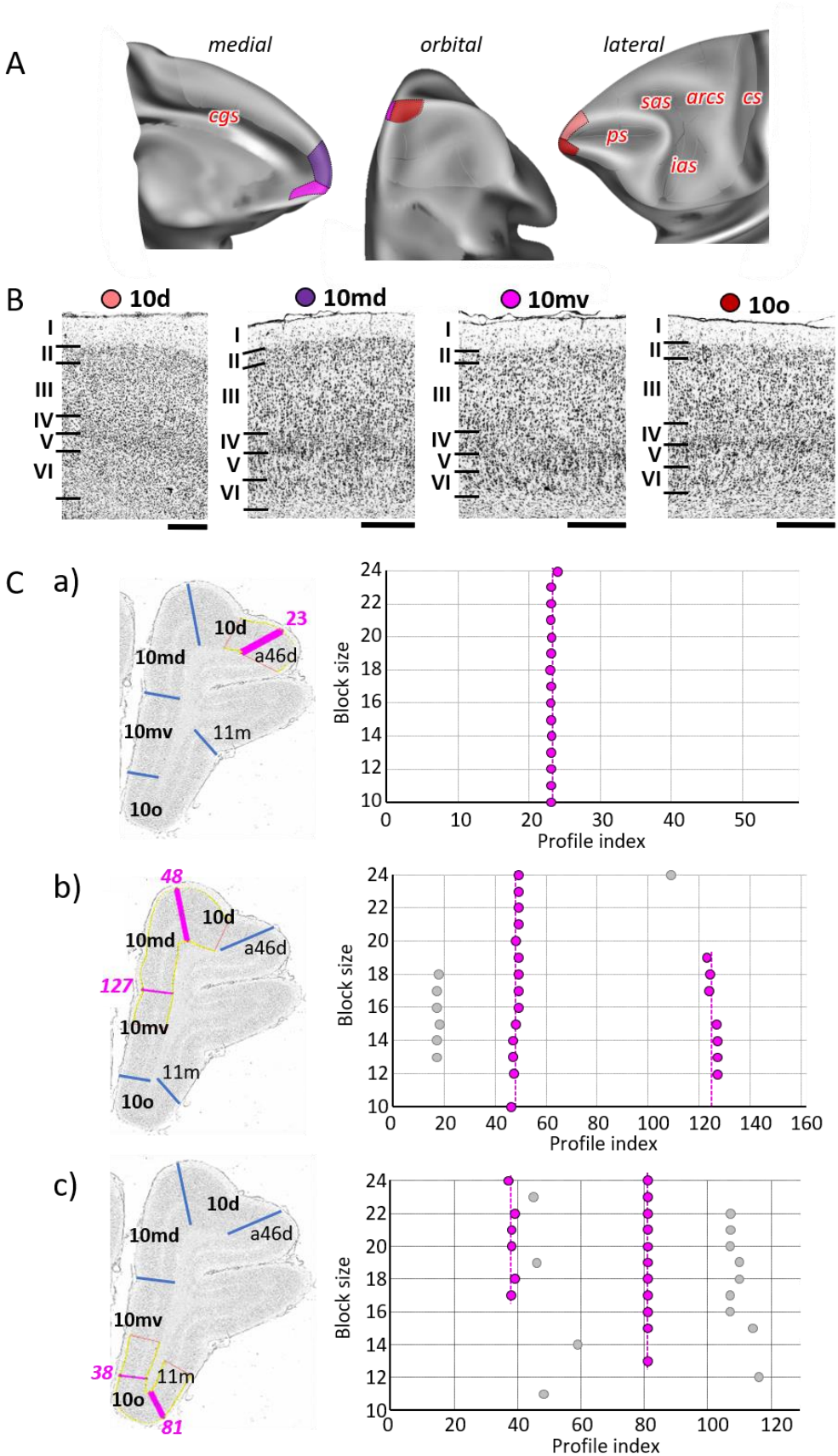

Figure 3 A) Position and extent of subdivisions of Walker's area 10 within the hemisphere are displayed on orbital, lateral and medial views of the Yerkes19. Macroanatomical landmarks are marked in red

letters. B) High-resolution photomicrographs show cytoarchitectonic features of areas 10d, 10md, 10mv and 10o. Each subdivision is labelled by a coloured dot, matching the colour of the depicted area on the 3D model. C) We confirmed cytoarchitectonic borders by a statistically testable method, where the Mahalanobis distance (MD) was used to quantify differences in the shape of profiles extracted from the region of interest. Profiles were extracted between outer and inner contour lines (yellow lines drawn between layers I/II and VI/white matter, respectively) defined on grey level index (GLI) images of the histological sections (left column). Pink lines highlight the position of the border for which statistical significance was tested. The dot plots (right column) reveal that the location of the significant border remains constant over a large block size interval (highlighted by the red dots). a) Depicts analysis of the border between areas 10d and a46d (profile index 23); b) depicts analysis of the border delineating dorsally located subdivisions, 10d and10md (profile index 48), as well as the medial border segregating dorsal and ventral subdivision, 10md and 10mv (profile index 127); and c) depicts analysis of the borders between ventrally positioned subdivisions of the frontal polar region, 10mv and 10o (profile index 38) and 10o and 11m (profile index 81). Scale bar 1mm. Roman numerals indicate cytoarchitectonic layers. *arcs* – spur of the arcuate sulcus; *cgs* – cingulate sulcus; *cs* – central sulcus; *ias* – inferior arcuate sulcus; *ps* – principal sulcus; *sas* – superior arcuate sulcus.

Twelve areas within the orbitofrontal and ventrolateral cortex (**Figs. 2 and 4A; Supp. Figs. 3 and 4**) were identified: two are located within Walker's area 14 (14r and 14c), four are within Walker's area 13 (13b, 13a, 13m and 13l), two are in Walker's area 11 (11m and 11l), and four are within Walker's area 12 (12r, 12m, 12l and 12o). Moving posteriorly along the ventromedial gyrus, granular cortex of area 10o transitions into dysgranular area 14r and further caudally into argranualr area 14c. Similar to areas 14, subdivisions of area 13, which are found on the medial wall of the *morb*, show rostro-caudal differences in the appearance of their layer IV, i.e., rostral area 13b is granular, whereas caudal area 13a is dysgranular (**Fig. 4B**). However, unlike areas 14r and 14c, subdivisions 13b and 13a have bilaminar layer V. Laterally, on the orbitofrontal gyrus, granular areas 11m and 11l occupy its rostral portion, while caudally dysgranular areas 13m and 13l are located, just rostral to the agranular insular region. The main difference among the subdivisions of area 11 is the pattern of cells in sublayer Vb, which is occasionally broken into aggregates of cells in area 11m, but continuous in area 11l. Similar, difference between 13m and 13l is related to the sublaminas V; i.e., in 13m layer Va is wider that Vb, whereas in 13l both layers are of comparable width (**Fig. 4B**). On the ventrolateral surface, the four subdivisions of Walker's area 12 are distinguished by the degree of granularity of layer IV, and the

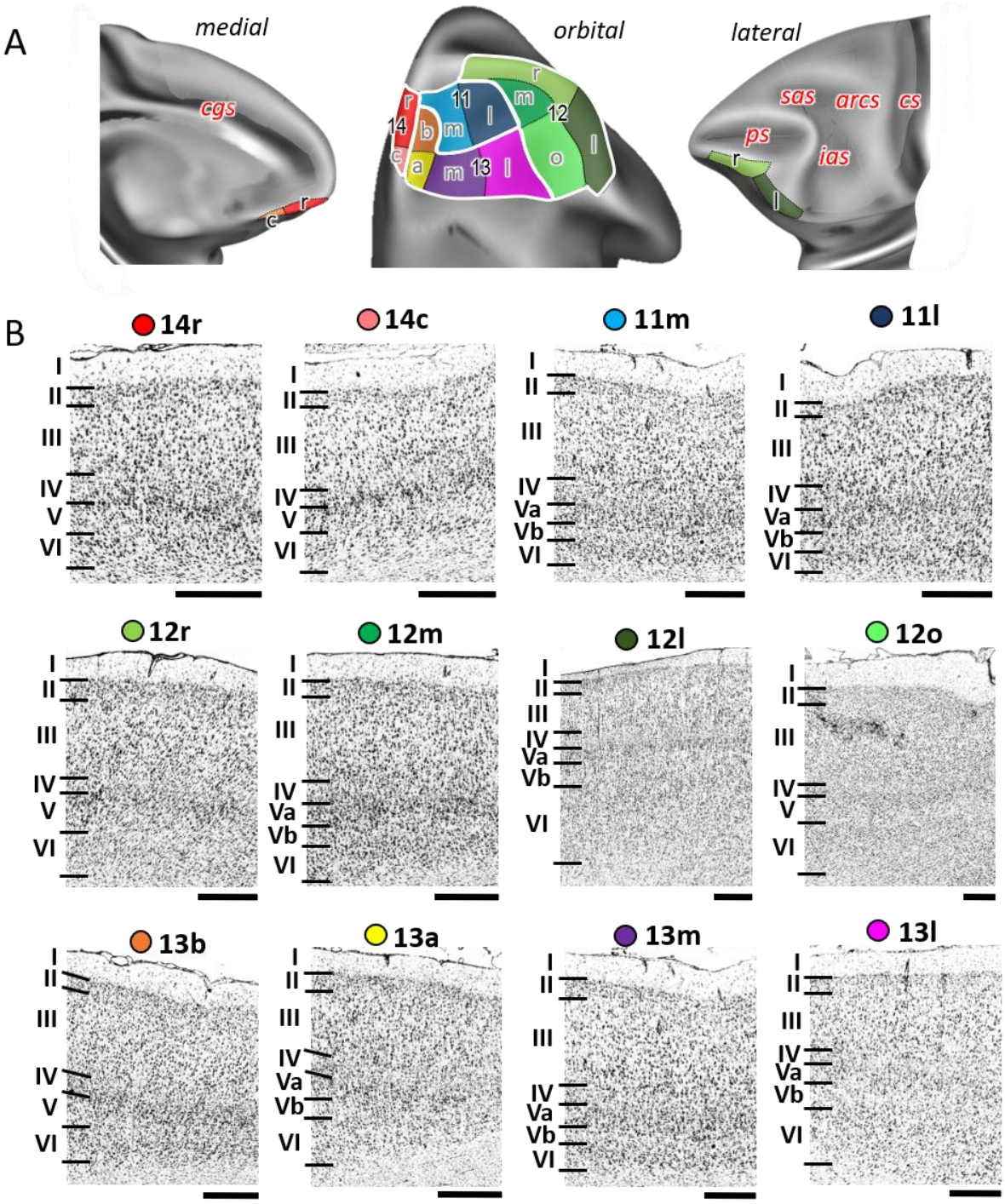

Figure 4 A) Position and extent of the orbitofrontal areas within the hemisphere are displayed on orbital, lateral and medial views of the Yerkes19. Macroanatomical landmarks are marked in red letters. B) High-resolution photomicrographs show cytoarchitectonic features of orbitofrontal 14r, 14c, 11m, 11l, 12r, 12m, 12l, 12o, 13b, 13a, 13m, and 13l. Each subdivision is labelled by a coloured dot, matching the colour of the depict area on the 3D model. A quantitative analysis of their cytoarchitectonic borders is shown in the **Supplementary Figures 3 and 4**. Scale bar 1mm. Roman numerals (and letters) indicate cytoarchitectonic layers. *arcs* – spur of the arcuate sulcus; *cgs* – cingulate sulcus; cs – central sulcus; *ias* – inferior arcuate sulcus; *ps* – principal sulcus; *sas* – superior arcuate sulcus.

size and distribution pattern of the pyramids in layers III and V (**Fig. 4B**). The most rostral area on the medioventral surface of the prefrontal cortex, 12r, is a dysgranular cortex with characteristic columnar aspect in layers III and V. Area 12m, located on the lateral wall of the *lorb*, has a bipartite layer V and a well-developed layer IV which distinguishes it from surrounding areas 12r and 13l. Area 12o, located medial to 12l on the caudal medioventral convexity, has a thin and weakly stained layer IV, and no obvious sublamination in layer V. Area 12l is granular cortex with clear subdivisions in layer V (**Fig. 4B**).

Medial and dorsolateral areas. The dorsal portion of the prefrontal cortex directly abutting area 10 of Walker is occupied by his area 9, within three distinct areas were identified (**Figs. 2 and 5A**): area 9m, located on the medial surface between areas 10md rostrally and 8Bm caudally, is followed dorsally by area 9d, which in turn is delimited laterally by 9l (directly adjacent to area 46). Areas 9d and 9l are limited rostrally by area 10d and caudally by areas 8Bd and 8Bs, respectively. All subdivisions of area 9 are characterized by the low packing density and width of layer III, and the sublamination of layer V with a prominent Va containing relatively large pyramidal cells and a sparsely populated Vb, which distinguishes them from neighbouring areas (**Fig. 5B**). This contrast between layers Va and Vb is particularly conspicuous in area 9l, thus clearly highlighting its border with area 9d (**Fig. 5C**). Area 9d can be distinguished from 9l by its wider, pale layer V. The most recognizable feature of areas 9d and 9l, that is not visible in area 9m, is the gradual increase in the size of layer III pyramids, with largest cells found close to layer IV (**Fig. 5B**).

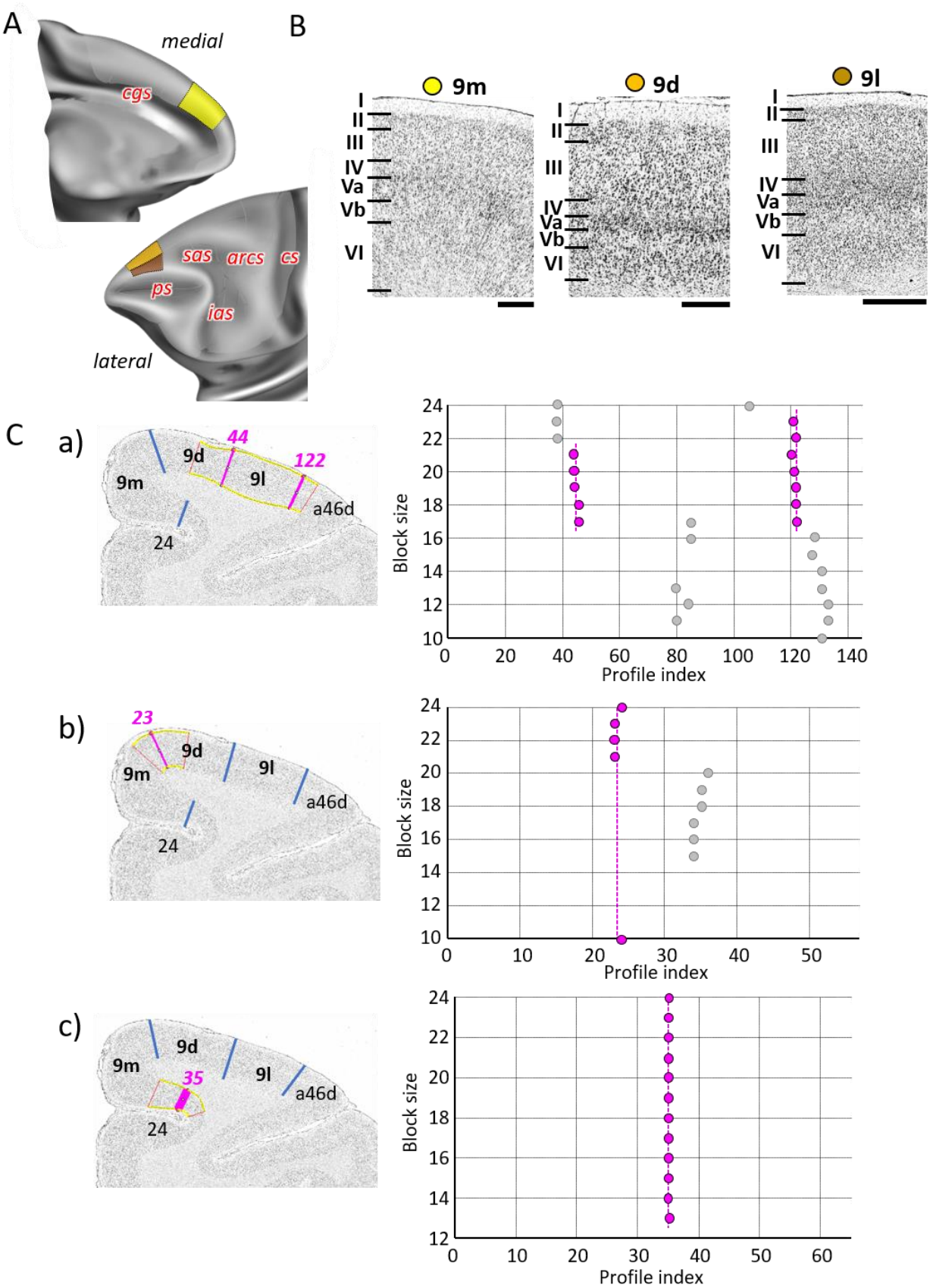

587

588 **Figure 5** A) Position and extent of the rostral medial and dorsolateral prefrontal areas within the
589 hemisphere are displayed on lateral and medial views of the Yerkes19. Macroanatomical landmarks

are marked in red letters. B) High-resolution photomicrographs show cytoarchitectonic features of areas 9m, 9d, and 9l. Each subdivision is labelled by a coloured dot, matching the colour of the depict area on the 3D model. C) We confirmed cytoarchitectonic borders by statistically testable method (for detail see **Fig. 3**). a) Depicts analysis of the borders between area a46d and 9l (profile index 122), as well as 9l and 9d (profile index 44); b) depicts analysis of the border between dorsal and medial subdivision, 9d and 9m (profile index 44); and c) depicts analysis of the border distinguishing medial subdivision 9m from cingulate cortex, area 24 (profile index 35). Scale bar 1mm. Roman numerals (and letters) indicate cytoarchitectonic layers. arcs – spur of the arcuate sulcus; *cgs* – cingulate sulcus; *cs* – central sulcus; *ias* – inferior arcuate sulcus; *ps* – principal sulcus; *sas* – superior arcuate sulcus.

As mentioned above, the dorsal portion of the most posterior part of the PFC is occupied by three subdivisions of Walker's area 8B (**Figs. 2 and 6A**): area 8Bm is located on the medial hemispheric surface, delimited caudally by the premotor cortex and rostrally by area 9m; area 8Bd is located on the dorsal surface along the midline; area 8Bs is a newly identified subdivision found on the cortical surface lateral to 8Bd and reaching the fundus of the *sas*. Walker's area 8A occupies the cortex surrounding the most caudal portion of the *ps*, where it abuts areas p46. Here we identified area 8Ad dorsally, which extends into the ventral wall of the *sas*, reaching its fundus, and area 8Av ventrally, extending into the rostral wall of the *ias*, and also reaching its fundus (**Figs. 2 and 6A**). Subdivisions of area 8B are dysgranular, whereas subdivisions of area 8A present a clearly developed layer IV (**Fig. 6B**). Area 8Bm is more weakly laminated than 8Bd and 8Bs, but presents a columnar organization not visible in the lattermost areas. Area 8Bd is characterized by a more densely packed layer II and by lager pyramids in layers III and V than areas 8Bm or 8Bs. Both subdivisions of area 8A have a clear laminar structure, with a well-developed layer IV, which is especially wide and dense in 8Av (Fig. 6B). All borders were statistically validated by the quantitative cytoarchitectonic analysis (**Fig. 6C; Supp. Figs. 6 and 7**).

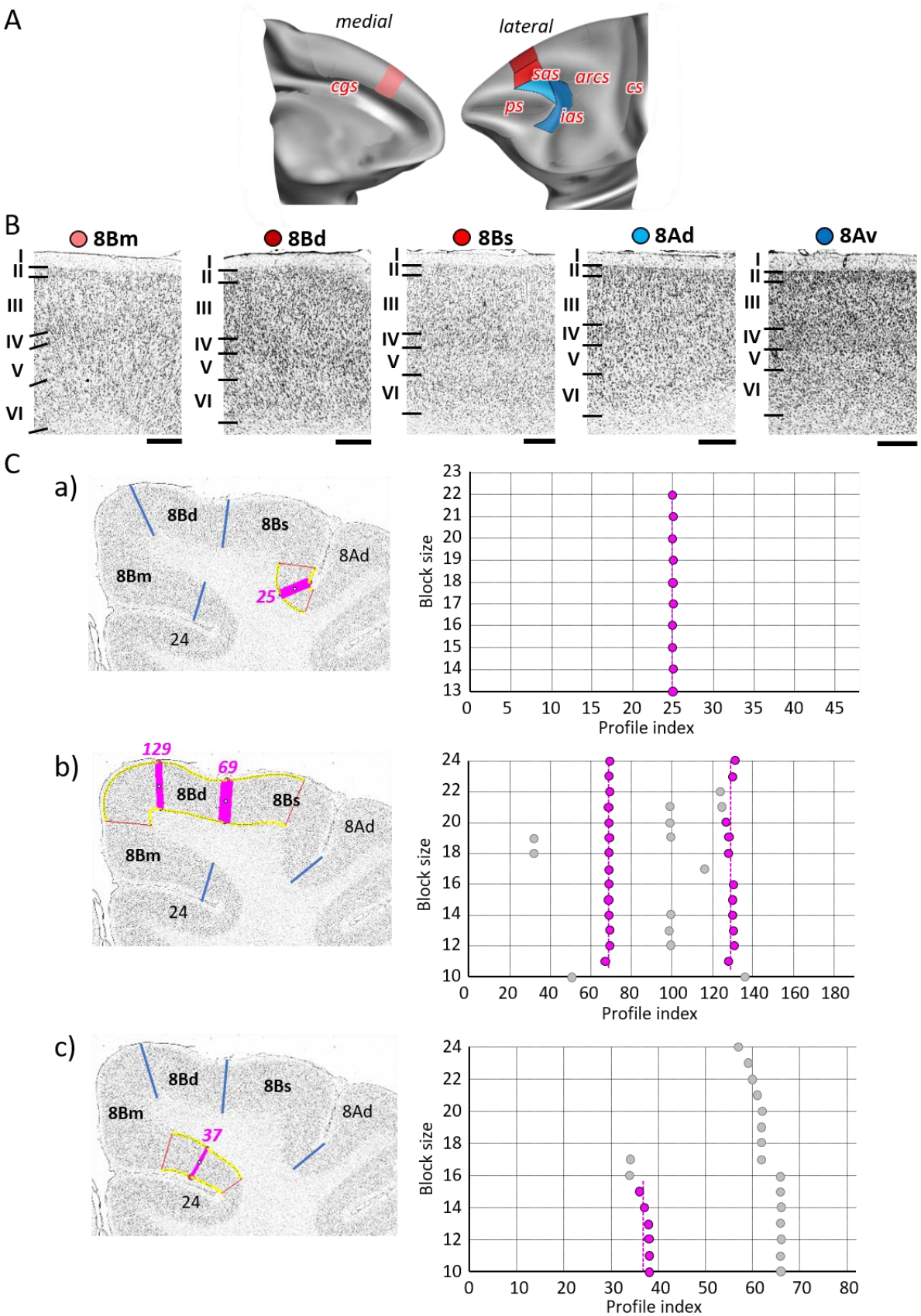

Figure 6 A) Position and the extent of the caudal medial and dorsolateral prefrontal areas within the hemisphere are displayed on lateral and medial views of the Yerkes19. Macroanatomical landmarks

are marked in red. B) High-resolution photomicrographs show cytoarchitectonic features of areas 8B (8Bm, 8Bd, 8Bs) and 8A (8Ad, 8Av). Each subdivision is labelled by a colored dot, matching the color of the depict area on the 3D model. C) We confirmed cytoarchitectonic borders of new 8B subdivisions by statistically testable method (for detail see **Fig. 3**). a) Depicts analysis of the border that separates new subdivisions 8Bs from neighbouring area 8Ad (profile index 25); b) depicts analysis of the borders which delineate area 8Bd from surrounding areas 8Bs and 8Bm (profile index 69), as well as 8Bd and 8Bm (profile index 129); and c) depicts analysis of the border distinguishing medial subdivision 8Bm from cingulate cortex, area 24 (profile index 37). Statistically testable borders for area 8Ad (adjacent to p46d) shown in the **Supp. Fig. 5** and for area 8Av borders can be seen in the **Supp. Fig. 6**. Scale bar 1mm. Roman numerals (and letters) indicate cytoarchitectonic layers. *arcs* – spur of the arcuate sulcus; *cgs* – cingulate sulcus; *cs* – central sulcus; *ias* – inferior arcuate sulcus; *ps* – principal sulcus; *sas* – superior arcuate sulcus.

A mosaic of distinct areas was identified within Walker's area 46 which encompasses our areas a46d, a46df, a46vf, a46v, p46d, p46df, p46vf, and p46v (**Figs. 2 and 7A; Supp. Figs. 5 and 6**). Such segregation results from a principal subdivision of area 46 into areas located within the anterior portion of the *ps* (the "a46-areas") and those found in its posterior portion (the "p46-areas"), as well as differences between areas located on the dorsal (the "46d-areas") and ventral (the "46v-areas") shoulders of the sulcus, or around its fundus (the "46f-areas"), depicted on our schematic drawing of the *ps* (**Fig. 7A**). Cytoarchitectonically, "a46" and "p46" areas can be distinguished by differences in the size of layer III and layer V pyramids, which are smaller in the posterior than in the anterior areas (**Fig. 7B**). Dorsal subdivisions of area 46 have a wider and more densely packed layer II than the ventral areas, which, in turn, have more a more prominent layer IV, and larger cells in layers V and VI. Areas located around the fundus of the ps, i.e., areas a46df/46vf and p46df/46vf, are additionally characterized by a clear border between layer VI and the white matter (**Fig. 7B**).

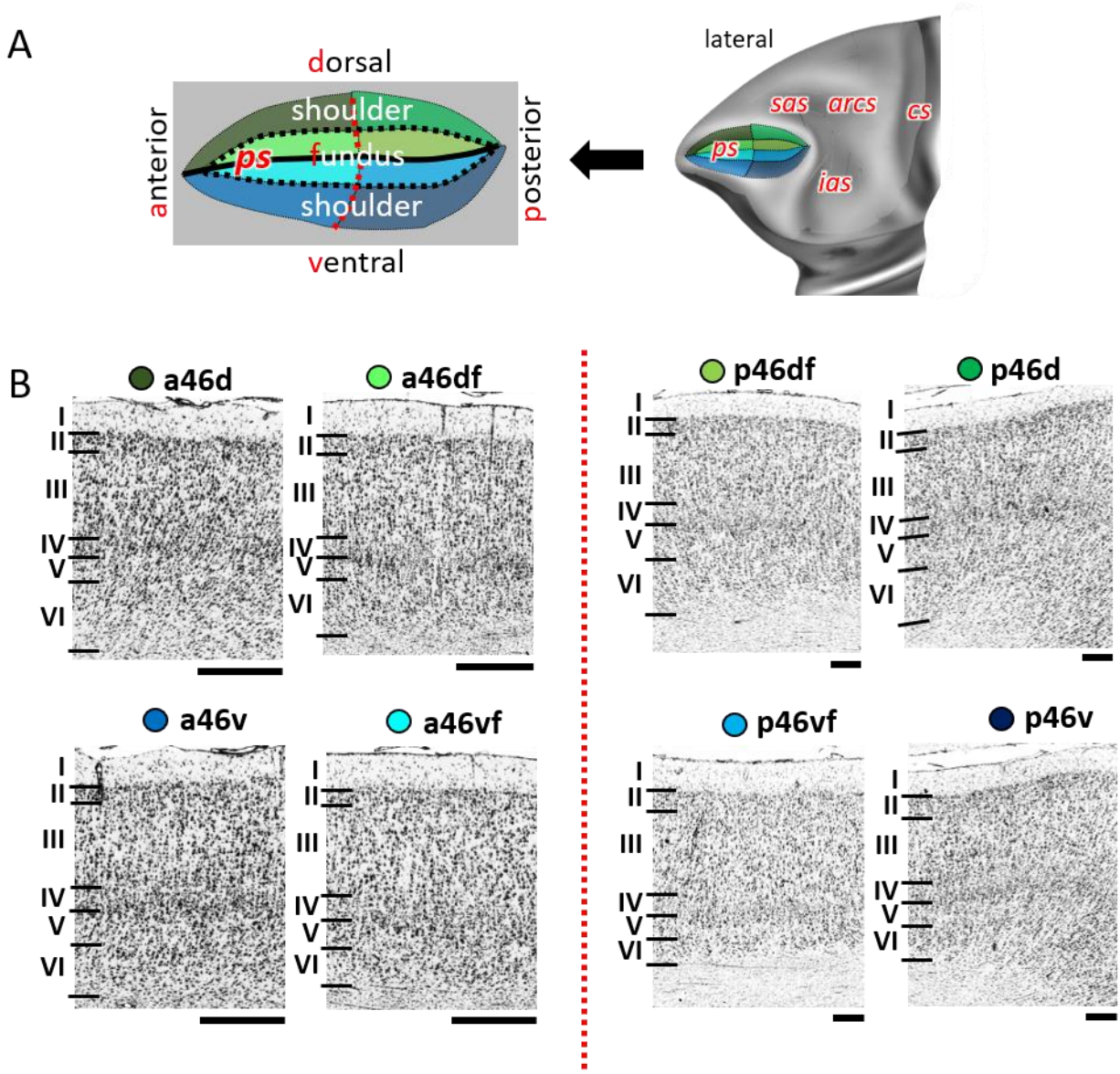

Figure 7 A) Position and the extent of areas located within and around the *ps*, are displayed on lateral view of the Yerkes19. Additionally, schematic drowning demonstrates how identified subdivisions are labelled with letters highlighted in red. Macroanatomical landmarks are marked in red letters. Black line indicates fundus, black dotted line marks border between shoulder and fundus region, and red dotted line separates anterior and posterior portion of sulcus. B) High-resolution photomicrographs show cytoarchitectonic features of anterior areas of 46 (a46d, a46df, a46vf, a46v) and posterior ones (p46d, p46df, p46vf, p46v), separated by red dashed line. Each subdivision is labelled by a colored dot, matching the color of the depict area on the 3D model. Scale bar 1mm. Roman numerals indicate cytoarchitectonic layers. A quantitative analysis of their cytoarchitectonic borders is shown in the **Supp. Figs. 4 and 5**. *arcs* – spur of the arcuate sulcus; *cs* – central sulcus; *ias* – inferior arcuate sulcus; *ps* – principal sulcus; *sas* – superior arcuate sulcus.

Caudal ventral areas. Rostral to the ventral premotor cortex, we identified areas 44, 45A and 45B (**Figs. 2 and 8A; Supp. Figs. 7 and 8**) belonging to the ventral granular PFC. Area 44 can be found along the deeper portion of the ventral wall of the *ias*, and encroaching onto its dorsal wall, where it abuts area 45B. The border between areas 45B and 45A was consistently found at the tip of the *ias*, whereby area 45A occupies the prearcuate convexity. Dysgranular areas 44 and granular area 45B can also be distinguished by differences in layer V which presents larger pyramids in the former than in the latter area (**Fig. 8B**). Layer IV of 45A is wider than that of 45B. Additionally, layer III pyramids tend to build clusters in area 45B, but not in 45A (**Fig. 8B**).

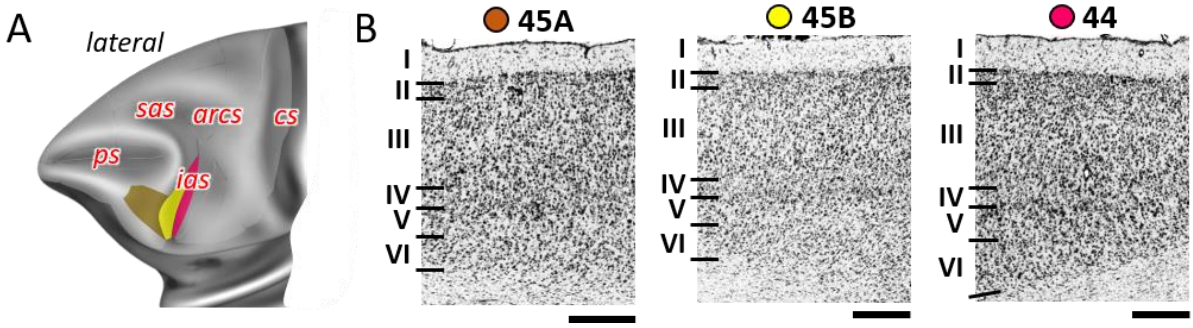

Figure 8 A) Position and the extent of the posterior ventrolateral areas within the hemisphere are displayed on lateral view of the Yerkes19. Macroanatomical landmarks are marked in red letters. B) High-resolution photomicrographs show cytoarchitectonic features of areas 44 and 45 (45A, 45B). Each subdivision is labelled by a colored dot, matching the color of the depict area on the 3D model. A quantitative analysis of their cytoarchitectonic borders is shown in the **Supp. Figs. 6 and 7**. Scale bar 1mm. Roman numerals indicate cytoarchitectonic layers. *arcs* – spur of the arcuate sulcus; *cs* – central sulcus; *ias* – inferior arcuate sulcus; *ps* – principal sulcus; *sas* – superior arcuate sulcus.

3.2 Receptor architectonic analysis

The regional and laminar distribution pattern of 14 distinct receptor types were characterized throughout the macaque prefrontal cortex for each cytoarchitectonically defined area (with the exception for 13a and 14c due to technical limitations) by means of receptor profiles. Silver-stained sections from the corresponding receptor brain were aligned with the receptor autoradiographs at the same macroanatomic level in order

to enable comparison of cytoarchitectonic border positions with receptor distribution patterns. Not all receptors show each areal border, and not all borders are equally clearly defined by all receptor types. Changes in receptor distribution patterns confirmed cytoarchitectonically identified borders, but did not reveal further subdivisions within the PFC.

In detail, neurotransmitter receptors display distinct laminar distribution patterns, which are preserved across all examined areas for most receptor types with the notable exception of the M_2 receptors (**Fig. 9; Supp. Fig. 9**). In some areas M_2 receptors present a single maximum in layer V (10mv, 10o, 14r, 13b, subdivisions of areas 11 and 46). Other areas present a bimodal pattern, with maxima in layers III and V. In some cases, both maxima are of comparable intensity (13m, 13l, subdivisions of area 12), and in other areas the maximum in layer III is clearly higher than that in layer V (10d, 10md, 44, and subdivisions of areas 9, 8B, 8A and 45). Kainate receptors also constitute a notable exception, because they are the only ones consistently presenting higher densities in the deeper than in the superficial cortical layers. The α_1 and 5-HT_{1A} receptors stand out due to their bimodal laminar distribution, with the highest of the two maxima located in the superficial layers. The remaining receptors present a rather unimodal laminar distribution pattern, whereby the width and position of the maximum varies depending on the receptor type. The D_1 receptor reaches its maximum density in subcortical structures, and a relatively homogeneous distribution throughout the neocortex.

Absolute receptor densities (averaged over all cortical layers) varied by several orders of magnitude depending on the receptor type (**Supp. Figs. 10 and 11**). Highest absolute values were found for the $GABA_B$ receptor (2644 fmol/mg in 11l) and lowest densities for the D_1 receptor (67 fmol/mg in 9l). Considerable differences in absolute densities were also found within a single neurotransmitter system. E.g., highest muscarinic cholinergic densities were found for the M_1 receptor (between 1152 fmol/mg in 12m and 708 fmol/mg in 8Av) and lowest for the M_2 receptor (between 223 fmol/mg in 13l and 134 fmol/mg in 14r). In general, lowest receptor densities were measured in subdivisions of areas 8B and 8A, which consequently displayed the smallest fingerprints of all PFC areas. Conversely, highest receptor densities were mainly located in orbitofrontal and frontopolar areas (**Figs. 10 and 11; Supp. Figs. 10 and 11**).

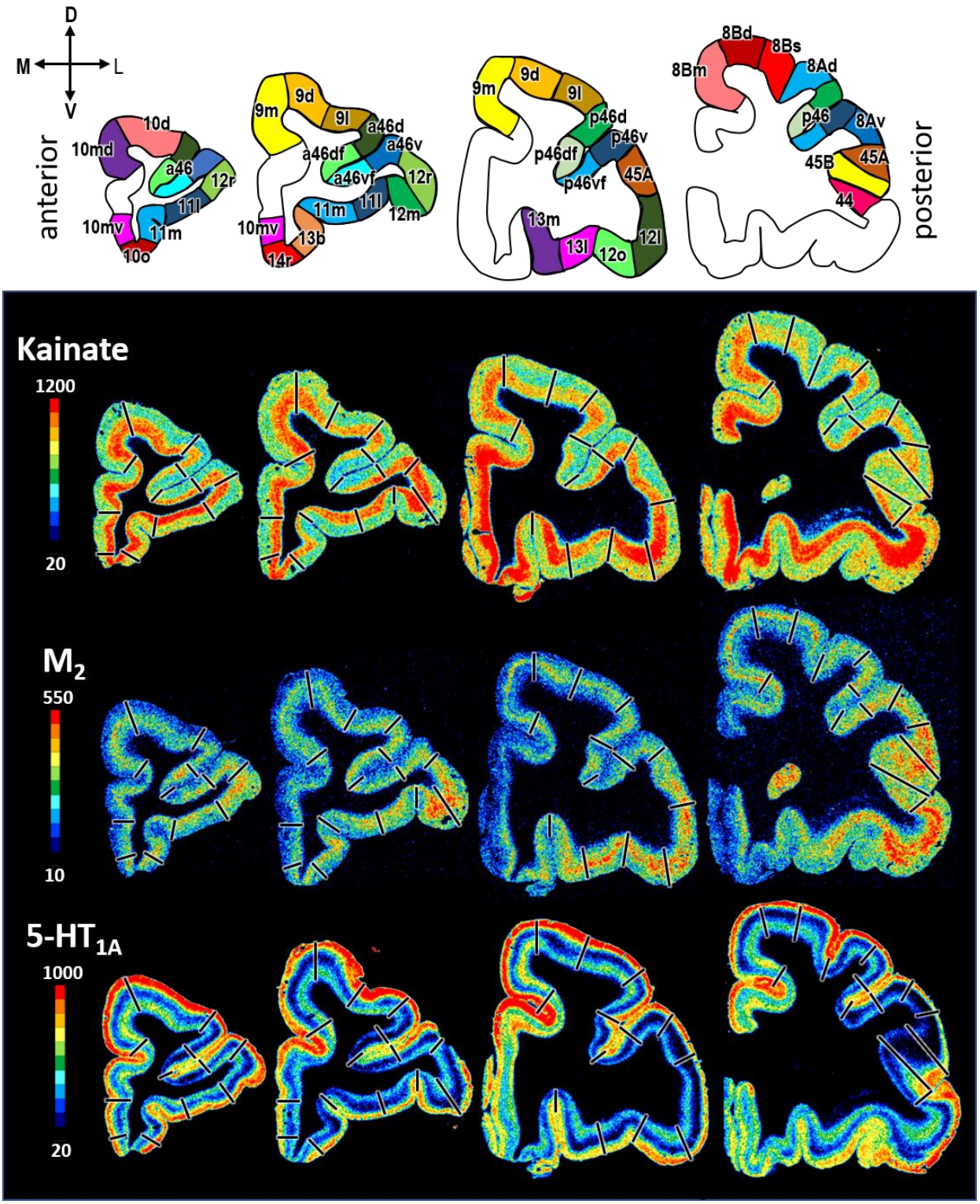

721

722 **Figure 9** Exemplary sections depicting the distribution of kainate, M_2 and 5-HT_{1A} receptors in coronal
723 sections through a macaque hemisphere. The color bar, positioned left to the autoradiographs, codes
724 receptor densities in fmol/mg protein and borders are indicated by black lines. The four schematic
725 drawings at the top represent the distinct rostro-caudal levels and show the position of all prefrontal
726 areas defined. Distribution patterns of the remaining receptors are shown in **Supp. Fig. 8**. C – caudal;
727 D – dorsal; R – rostral; V – ventral.

Out of all prefrontal areas examined here, we found that the frontopolar region (i.e., area 10 subdivisions) is characterized by the highest density of kainate and $GABA_A$/BZ densities. Changes in the laminar pattern of $GABA_A$, M_1, M_2, α_1 and $5HT_{1A}$ receptors most clearly highlight the cytoarchitectonically defined borders within area 10 (**Fig. 9; Supp. Fig. 9**). Differences in the size of fingerprints particularly reflect the dorso-ventral subdivision, with smaller sized fingerprints in areas 10d/10md compared to 10mv/10o (**Fig. 10; Supp. Fig. 10**). Both ventrally positioned subdivisions of area 10 (i.e., areas 10mv and 10o) differed significantly from caudally adjacent area 14r, though not always for the same receptor types (**Tab. 3**). Area 14r presented significantly lower AMPA and $GABA_A$ receptor densities than 10mv and 10o, respectively. Additionally, $GABA_A$/BZ densities in 10mv and 10o were significantly higher than in 14r. Likewise, dorsal subdivisions of area 10 presented a differential pattern of significant receptor densities compared to neighbouring areas. Areas 10d and 10md contain significantly higher kainate and NMDA receptor densities, respectively, than caudally adjacent subdivisions of area 9.

Table 3. FDR-corrected p-values for the post hoc tests (i.e., third level tests; p-values were corrected for 258 comparisons per receptor type). Note, no p-values are provided for the M_1, M_2, 5-HT_2 or D_1 receptors, because they did not reach the level of significance in the second level test. Green background highlights significant pairs of adjacent prefrontal areas in the macaque brain. $*$ $p < 0.05$, $**$ $p < 0.01$, $***$ $p < 0.001$

	AMPA	**kainate**	**NMDA**	**$GABA_A$**	**$GABA_B$**	**BZ**	**M_3**	**α_1**	**α_2**	**5-HT_{1A}**
10d - 10md	0.9393	0.5591	0.8028	0.8776	0.6976	0.7871	0.7553	0.9104	0.866	0.9753
10d - 9d	0.9041	0.1142	0.5721	0.8364	0.1413	0.8728	0.6135	0.9104	0.5692	0.9081
10d - 9l	0.618	**0.0091****	0.4329	0.5871	0.4474	0.7277	0.4173	0.9549	0.4603	0.746
10d - a46dr	0.3472	0.4435	0.194	0.7085	0.9711	0.3149	0.3845	0.5571	0.6929	0.1842
10md - 10mv	0.6304	0.8867	0.3033	0.9407	0.4908	0.8415	0.586	0.7554	0.8435	0.7195
10md - 9m	0.8231	0.1508	**0.0461***	0.1826	0.8701	0.1242	0.1456	0.8313	0.5417	0.9816
10mv - 10o	0.4391	0.9801	0.5458	0.8064	0.7872	0.8587	0.7441	0.9973	0.8276	0.9081
10mv - 14r	**0.0386***	0.149	0.2167	0.1305	0.3529	**0.0291***	0.3522	0.7752	0.2444	0.3143
10o - 11m	0.7018	**0.0056****	0.6676	0.8425	0.5291	0.2996	0.5396	0.9549	0.9936	0.0666
10o - 14r	0.168	0.1227	0.5525	**0.0366***	0.5751	**0.0291***	0.1793	0.7645	0.1471	0.2115
11l - 11m	0.8207	0.5126	0.8931	0.4519	0.4832	0.8721	0.7807	0.9104	0.7881	0.8618

11l - 12m	0.8207	0.9666	0.9271	0.7045	0.058	0.7409	0.7964	0.8085	0.3854	0.8686
11l - 12r	0.5848	0.3727	0.2291	0.8932	0.2739	0.8721	0.7446	0.7645	0.1325	0.917
11l - 13l	0.2408	0.6732	0.9223	0.4866	0.0523	0.9766	0.2814	0.9549	0.1427	0.7352
11l - 13m	0.1005	0.4105	0.9256	0.3035	**0.0104***	0.8678	0.9487	0.7645	0.0781	0.9081
11m - 13b	0.0988	0.3998	0.8028	0.3063	0.4593	0.8728	0.2991	0.9549	0.8403	0.917
11m - 13l	0.1593	0.9801	0.8261	0.8911	0.208	0.8652	0.19	0.9795	0.0925	0.6198
11m - 13m	0.06	0.1684	0.8261	0.698	0.0554	0.9766	0.7943	0.8541	**0.0465***	0.997
11m - 14r	0.0688	0.4928	0.2895	**0.0159***	0.9809	0.489	**0.0347***	0.812	0.149	0.8153
12l - 12o	0.7396	0.7221	0.5477	0.7785	0.7117	0.5449	0.591	0.9338	**0.0323***	0.9837
12l - 12r	0.7423	0.84	0.9808	**0.0261***	0.0824	0.7523	0.0613	0.3864	0.6495	0.9869
12l - 45A	0.2779	0.0773	0.2152	0.8729	0.4924	0.9984	0.5606	0.148	0.9231	0.0933
12m - 12o	0.4391	0.8664	0.9223	0.1851	0.7851	0.7313	0.2335	0.9973	0.6306	0.7877
12m - 12r	0.4191	0.3735	0.3465	0.8326	0.4936	0.8721	0.9602	0.5104	**0.0176***	0.7772
12m - 13l	0.1742	0.7207	0.9867	0.7785	0.7649	0.7496	0.4295	0.929	0.5069	0.8618
12o - 12r	0.9669	0.5144	0.4782	0.0923	0.2583	0.8587	0.2335	0.5575	**0.004****	0.9881
12o - 13l	0.5736	0.6021	0.9649	0.5306	0.9429	0.9901	0.9049	0.929	0.8128	0.6789
12r - a46vr	**0.0151***	0.3743	0.6393	0.0962	0.0824	0.8738	0.3415	0.9973	0.7023	0.6442
12r - p46vr	**0.0427***	0.0659	0.2246	**0.0032****	**0.019***	0.7409	**0.0347***	0.7253	0.6634	0.3438
13b - 14r	0.8536	0.973	0.4654	0.2172	0.4936	0.7277	0.339	0.88	0.1052	0.9081
13l - 13m	0.7624	0.2909	0.9979	0.8563	0.7452	0.8587	0.4298	0.8565	0.8354	0.6937
44A - 45B	0.9416	0.9648	0.9808	0.8425	0.677	0.8415	0.933	0.6727	0.4447	0.089
45A - 45B	0.5714	**0.0122***	0.6278	0.97	0.7593	0.8721	0.7363	0.7902	0.1275	0.2574
45A - 8Av	0.0988	**0.0062****	0.095	0.1219	0.5291	0.9928	**0.0476***	0.0857	**0.0401**	0.0853
45A - p46vr	0.7274	0.6956	0.9363	0.9604	0.6792	0.9901	0.4861	0.9549	0.9686	0.4794
45B - 8Av	**0.0335***	0.9801	**0.0327***	0.0914	0.3129	0.8721	0.1754	**0.0238***	**0.0004*****	**0.0016****
8Ad - 8Av	0.2009	**0.0487***	0.5458	0.9852	0.1933	0.9897	0.2412	**0.0155***	0.6929	**0.0073****
8Ad - 8Bs	0.7142	**0.0183***	0.7149	0.9407	0.8209	0.7836	0.9833	0.9978	0.2807	0.7062
8Ad - p46dr	0.6185	0.0705	0.5546	0.123	0.9152	0.9984	0.2024	0.9795	0.358	0.7062
8Av - p46vr	0.2667	**0.0009*****	0.0726	0.1047	0.2099	0.9915	**0.0036****	0.1038	**0.0344***	**0.0043****
8Bd - 8Bm	0.6165	0.1226	0.7936	0.9194	0.9698	0.7409	0.9038	0.937	0.8403	0.4665
8Bd - 8Bs	0.8684	0.2213	0.6066	0.8663	0.968	0.7386	0.9602	0.7048	0.2297	0.6243
8Bd - 9d	0.1213	**0.0168***	**0.0031****	**0.0011****	**0.0469***	0.9557	**0.0155***	0.3477	**0.0044****	**0.004****
8Bm - 9m	0.2744	0.1202	0.1303	0.115	0.5171	0.9071	0.1863	0.5663	0.2868	0.1364
8Bs - 9l	0.385	**0.0058****	**0.0364***	**0.0083****	0.2099	0.9766	**0.0362***	0.1957	0.084	0.1598
9d - 9l	0.6967	0.3221	0.8516	0.7657	0.5923	0.8587	0.7964	0.8085	0.8602	0.6144
9d - 9m	0.7704	0.3551	0.3881	0.2172	0.2099	0.6636	0.2048	0.9384	0.1121	0.9095
9l - a46dr	0.7246	0.054	0.6553	0.8908	0.4226	0.7544	0.9602	0.5726	0.1595	0.3769
a46d - a46dr	0.6801	**0.004****	0.4699	0.7705	0.7808	0.8728	0.5621	0.833	**0.0257***	0.5572
a46d - a46v	0.3688	0.8465	0.5764	0.5843	0.3129	0.9857	0.6279	0.9549	0.747	0.7573

a46d - p46d	0.6714	0.6574	0.7815	0.9612	0.9519	0.8721	0.528	0.6964	0.9208	0.9138
a46dr - p46dr	0.6434	0.6648	0.6831	0.3038	0.8504	0.9781	0.5283	0.7053	0.5933	0.7062
a46v - a46vr	0.0688	**0.0105***	0.5349	0.3464	0.3066	0.9766	0.5895	0.4481	**0.0101***	0.9936
a46v - p46v	0.9393	0.9003	0.6864	0.9146	0.968	0.489	0.402	0.7902	0.9948	0.7508
a46vr - p46vr	0.8536	0.3958	0.5219	0.2731	0.677	0.8721	0.287	0.7048	0.9504	0.7352
p46d - p46dr	0.7061	0.0724	0.3835	0.1953	0.638	0.7277	0.5781	0.8386	**0.003****	0.9546
p46d - p46v	0.7953	0.7199	0.6601	0.6934	0.226	0.7501	0.7768	0.8638	0.8326	0.6022
p46v - p46vr	0.1742	0.0982	0.3824	0.0563	0.0746	0.3428	0.4663	0.3193	**0.0146***	0.4608

Within the orbitofrontal cortex, laminar distribution patterns of kainate, $GABA_A$, $GABA_B$, M_1, M_2 and M_3 receptors most clearly reflect the cytoarchitectonically identified areas 14r, 13b, 11m and 11l, whereas caudal orbital areas 13m and 13l are highlighted by the laminar distribution of kainate, $GABA_A$, α_1, M_2, M_3 and $5HT_{1A}$ receptors (**Fig. 9; Supp. Fig. 9**). Particularly areas 14r and 12l stand out due to the shape and size of their fingerprints (**Fig. 10; Supp. Fig. 10**). Area 14r is characterized by the lowest $GABA_A$/BZ and M_2 densities within PFC, but is among areas with the highest $GABA_B$ and α_1 levels. In addition to the above described differences with frontopolar areas, 14r contains significantly lower $GABA_A$ and M_3 densities than area11m (**Tab. 3**). Rostral orbital region occupied by the subdivisions 11m and 11l measured highest concentration levels for M_3 among all prefrontal areas, and dysgranular areas 13m and 13l have the highest levels of AMPA, M_2 and α_2 in regard to all other orbital areas. Significant differences between 11l and neighbouring areas were only found for the $GABA_B$ densities in area 13m, whereas 11m differed significantly from areas 14r and 10o in its $GABA_A$ and M_3 and its kainate densities, respectively (**Tab. 3**).

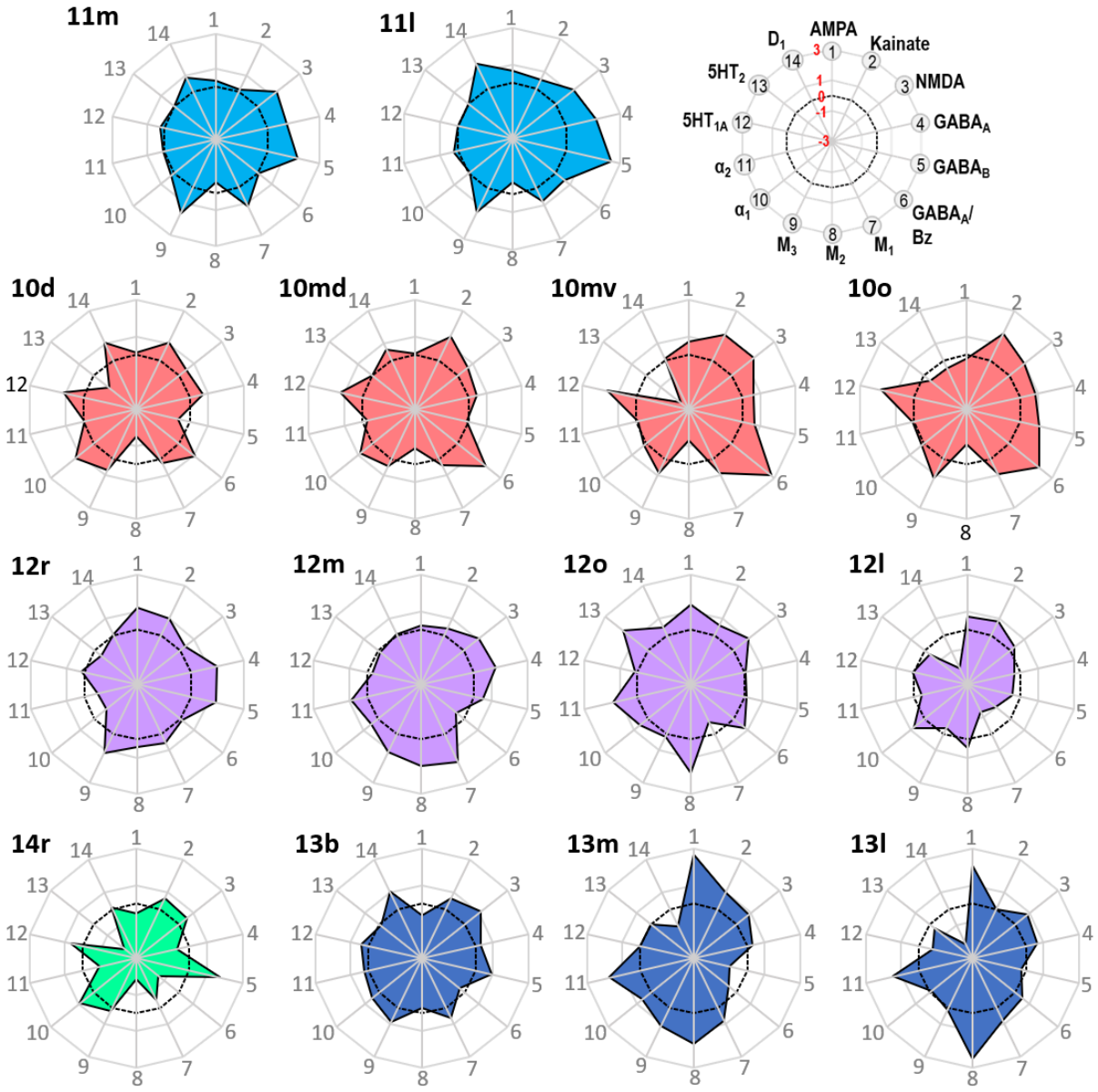

Figure 10 Normalized receptor fingerprints of the frontopolar and orbital areas. Black dotted line on the plot represents the mean value over all areas for each receptor. Receptors displaying a negative z-score are indicative of absolute receptor densities which are lower than the average of that specific receptor over all examined areas. The opposite is true for positive z-scores. Labelling of different receptor types, as well as the axis scaling, are identical for each area plot, which is specified in the polar plot on the top of the figure.

Within Walker's area 12, differences between rostral ventrolateral areas 12m and 12r are best delineated by changes in the laminar distribution patterns of AMPA, $GABA_A$, $5HT_{1A}$, M_1 and M_3 receptors, whereas the border between caudal subareas 12o and 12l is most clearly revealed by the laminar distribution pattern of kainate,

779 $GABA_A$, α_1, M_2, M_3 and $5HT_{1A}$ receptors (**Fig. 9; Supp. Fig. 9**). In general terms, 12r
780 has the highest and 12l the lowest densities measured within Walker's area 12, and in
781 the size of their fingerprints (**Fig. 10; Supp. Fig. 10**). Medially positioned areas (12m
782 and 12o) have significantly higher α_2 receptor densities than laterally positioned areas
783 (12r and 12l). For the lateral areas we also found significant differences in the rostro-
784 caudal direction, whereby 12r has significantly higher $GABA_A$ densities than 12l.
785 Additionally, 12r contains significantly higher AMPA receptor densities than dorsally
786 adjacent areas a46v and p46v. Area 12r also contains significantly higher $GABA_A$,
787 $GABA_B$, and M_3 receptor densities than does p46v (**Tab. 3**).

788 Differences in receptor architecture also revealed a novel cytoarchitectonic
789 subdivisions of Walker's areas 9 and 8B. In particular, the borders between areas 9m,
790 9d and 9l are most clearly reflected in the laminar distribution patterns of kainate,
791 NMDA, $GABA_A$/BZ, M_3, α_2, $5HT_{1A}$ and $5HT_2$ receptors. Subdivision of area 8B into
792 8Bm, 8Bd and 8Bs is clearly revealed by differences in the laminar distribution patterns
793 of AMPA, kainate, M_1, M_3 and 5-HT_{1A} receptors (**Fig. 9; Supp. Fig. 9**). Newly defined
794 area 8Bs contains the lowest kainate density out of all prefrontal areas, whereas area
795 8Bd presents the lowest NMDA and $GABA_A$ receptor densities within the PFC. In
796 general, subdivisions of Walker's area 9 contain higher receptor densities than those
797 of his area 8B, and this is reflected in their slightly larger fingerprints (**Supp. Fig. 11**).
798 There are also pronounced differences in the shape of the fingerprints, and this
799 becomes particularly obvious when observing the normalized fingerprints (**Fig. 11**).
800 Areas 9d and 9l show significantly higher kainate, NMDA, $GABA_A$, and M_3 receptor
801 densities than their caudal counterparts within area 8B (i.e., 8Bd and 8Bs,
802 respectively). Additionally, α_2 and 5-HT_{1A} densities are significantly higher in 9d than
803 in 8Bd (**Tab. 3**). Area 8Bs has significantly lower kainate receptor levels than laterally
804 adjacent area 8Ad. The border between areas 8Bs and 8Ad is also revealed by
805 differences in the laminar distribution pattern of kainate, M_1, α_1, 5-HT_{1A} and 5-HT_2
806 receptors (**Fig. 9; Supp. Figs. 9**).

807 The border between the dorsal and ventral subdivisions of Walker's area 8A (i.e.,
808 8Ad and 8Av) is most clearly indicated by laminar differences in the distribution of
809 kainate, $GABA_A$, $GABA_B$, M_2, and α_1 receptors. Area 8Av was characterized by the
810 lowest density of AMPA, $GABA_B$, M_1, M_3, α_1, α_2 and $5HT_{1A}$ receptors out of all areas
811 analysed here, thus for this area the size of the fingerprint was the smallest

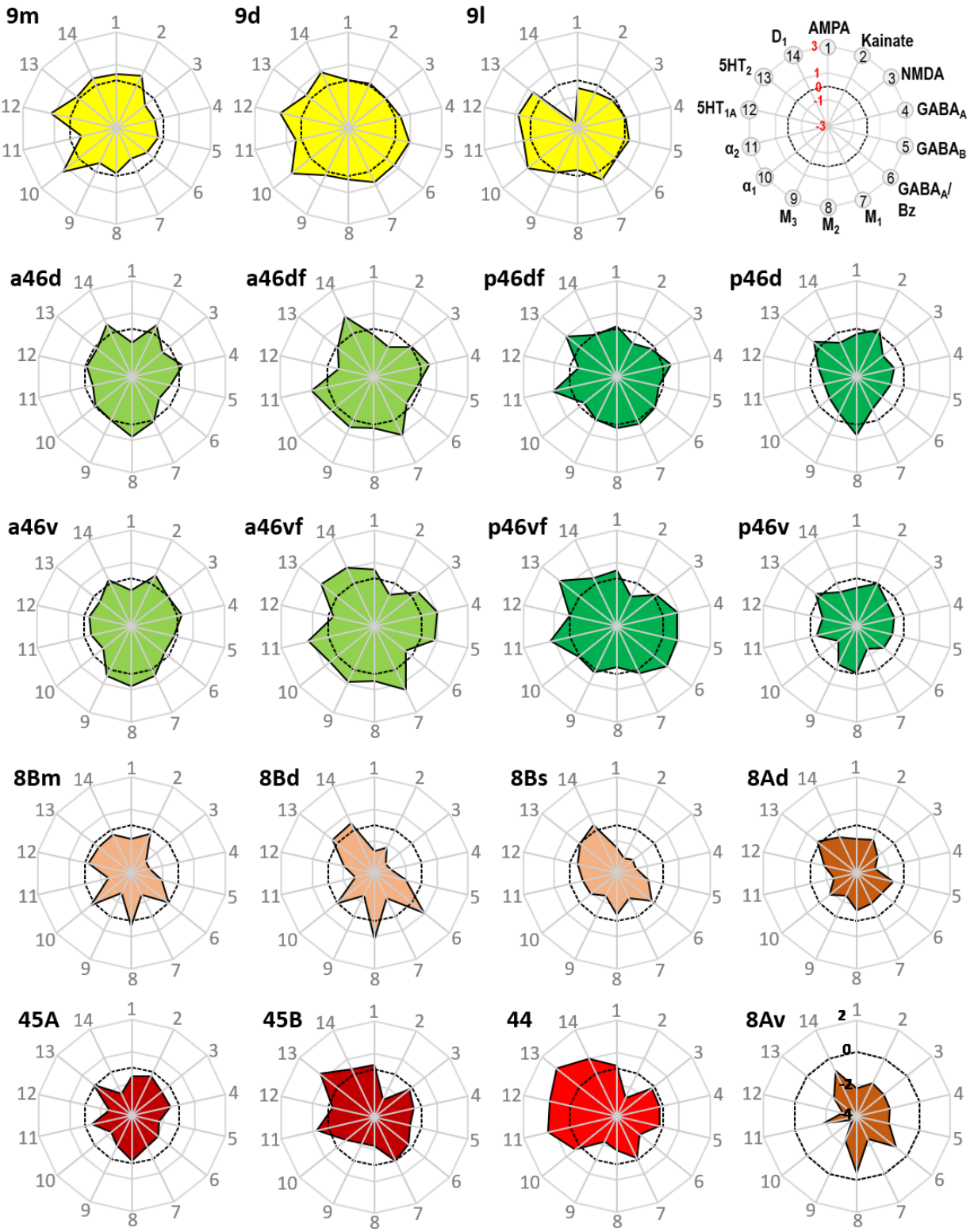

Figure 11 Normalized receptor fingerprints of the medial, dorsolateral, lateral and ventrolateral areas. Black dotted line on the plot represents the mean value over all areas for each receptor. Receptors displaying a negative z-score are indicative of absolute receptor densities which are lower than the average of that specific receptor over all examined areas. The opposite is true for positive z-scores. Labelling of different receptor types, as well as the axis scaling, are identical for each area plot, which

is specified in the polar plot on the top of the figure. Due to the low receptor densities measured in area 8Av, scaling for its fingerprint is adjusted and shown directly on the corresponding polar plot.

in the PFC (**Fig. 11; Supp. Fig. 11**). Area 8Av has significantly lower kainate α_1, and $5HT_{1A}$ receptor densities than 8Ad. It also has significantly lower densities of kainate, M_3, and α_2 than neighbouring area 45A, of AMPA, NMDA, α_1, α_2 and $5HT_{1A}$ receptors than area 45B, as well as of kainate, M_3, α_2 and $5HT_{1A}$ receptors than area p46v (**Tab. 3**).

Subdivisions of Walker's area 46 within and around the *ps* identified by cytoarchitectonic analysis were revealed by the following differences in receptor architecture. Changes in the laminar distribution patterns of AMPA, kainate, $GABA_A$, $GABA_B$, $GABA_A$/BZ and M_3 receptors most clearly reveal delineation of subdivisions within Walker's area 46 for both, anterior and posterior subareas (**Fig. 9; Supp. Fig. 9**). In general, higher densities were found in areas located around the fundus of *ps* than in those located on its dorsal and ventral shoulders, and higher muscarinic cholinergic densities were found in all anterior subdivisions of area 46 than in their caudal counterparts. Furthermore, differences in the fingerprints of anteriorly located subdivisions of area 46 and their corresponding posterior counterparts were greater for areas located on the shoulder (e.g., when comparing a46d and p46d) than for areas located around the fundus (e.g., when comparing a46df and p46df; **Fig. 11; Supp. Fig. 11**). Along the entire length of the *ps* we found significantly higher α_2 receptor densities in areas located around its fundus than the adjacent areas on the shoulder. Interestingly, significant differences in kainate receptors were found only for anterior areas, whereby they were higher in a46d and a46v than in a46df and a46vf, respectively (**Tab. 3**).

Cytoarchitectonic borders between areas 45A, 45B and 44 are clearly reflected by changes in the laminar distribution pattern of kainate, $GABA_B$, $GABA_A$/BZ, M_1, M_2, α_1 and 5-HT_{1A} receptors (**Fig. 9; Supp. Fig. 9**). The size of the normalized receptor fingerprints increases gradually when moving from area 45A through 45B to 44 (**Fig. 11**). Area 45A contains significantly higher kainate levels compared to 45B (**Tab. 3**). Out of all prefrontal areas, area 44 had highest concentration levels recorded for $5HT_2$ receptors. Furthermore, whereas area 44 presents one of the highest 5-HT_{1A} receptor

densities within the PFC, area 45A contains the second lowest PFC density of this receptor type, and 45B only an intermediate to low value, and these differences are reflected in the unique shaped normalized fingerprint of area 44 (**Fig. 11**).

3.3 Hierarchical clustering and principal component analyses

The hierarchical cluster analysis (**Fig. 12A**) revealed differences in size of receptor fingerprints between subdivisions occupying its most rostral portion (found in clusters 1 and 2) from the more caudally positioned prefrontal areas and (pre)motor areas (found in clusters 3, 4 and 5). The five main clusters, which were identified by the k-means analysis, are mostly composed of neighbouring subdivisions, but also group areas that do not share common borders and occupy different regions of the hemisphere.

- **Cluster 1** is the largest cluster, and encompasses the most rostrally located prefrontal areas. It includes all subdivisions of frontal polar cortex (10d, 10md, 10mv, 10o), all subdivisions of area 46 located in the depth of *ps* (a46df, a46vf, p46df, p46vf), anterior subdivisions of 46 located on the shoulders of *ps* (a46d, a46v), rostral orbital areas (11m, 11l, 13b, 14r, 12r, 12m), as well as dorsal and medial areas 9d and 9m. In particular, areas a46df and a46vf are more similar to medial area 12m, than to their posterior counterparts (p46df and p46vf, respectively), while areas a46d and a46v showed a greater similarity with orbital areas 13b and 14r and with medio-dorsal areas 9m and 9d. Additionally, rostral orbital areas 11m and 11l grouped with laterally adjacent area 12r.
- **Cluster 2** is constituted of the posterior orbital areas 13m, 13l, 12o and 12l, as well as dorsal area 9l and premotor area F5v.
- **Cluster 3** encompasses areas positioned most posteriorly in the prefrontal cortex (8Bd, 8Bm, 8Bs, 8Ad, p46d, p46v, 45A, 45B, 44) and premotor areas (F3, F6, F2d, F7d, F5d, F5s). The subdivisions of area 8B grouped closely with area 8Ad, which displayed highest similarity to the medially adjacent area 8Bs, and premotor area F7d, which is the most similar to 8Bd. Medial premotor areas F6 and F3 clustered with caudal premotor area F2d, whereas the posterior subdivisions of area 46 located on the shoulder of the *ps*, areas p46d and p46v,

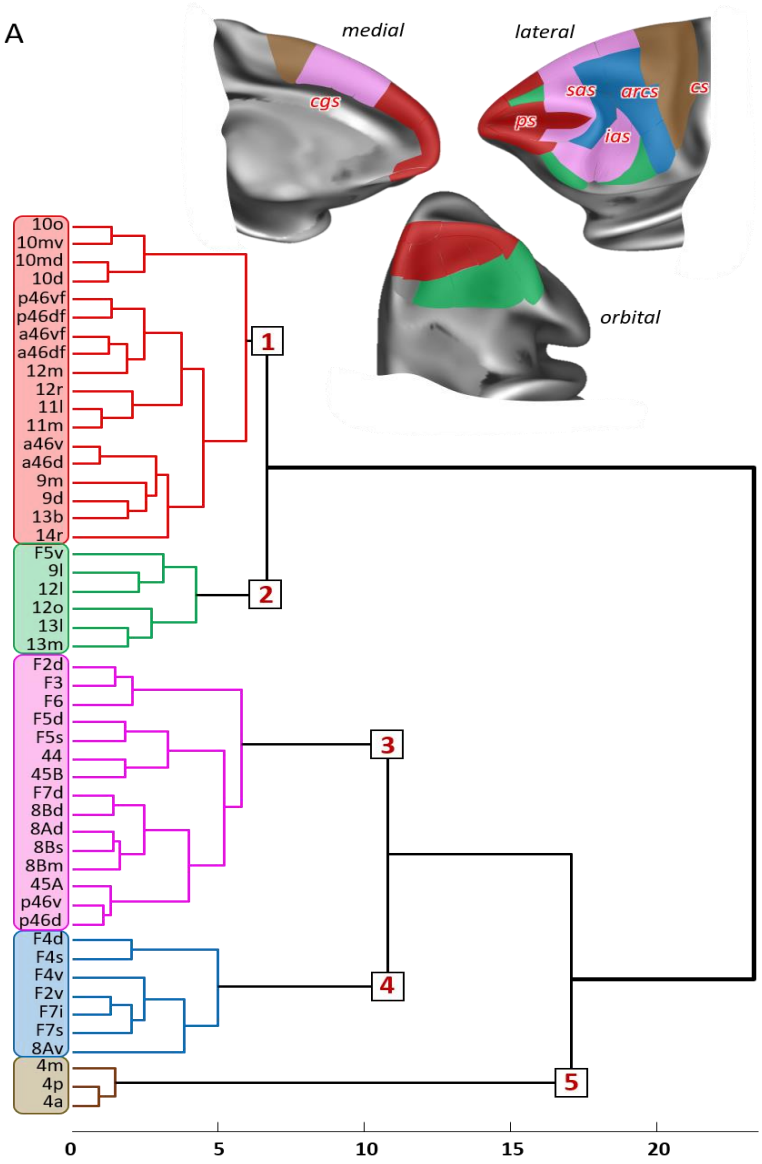

880

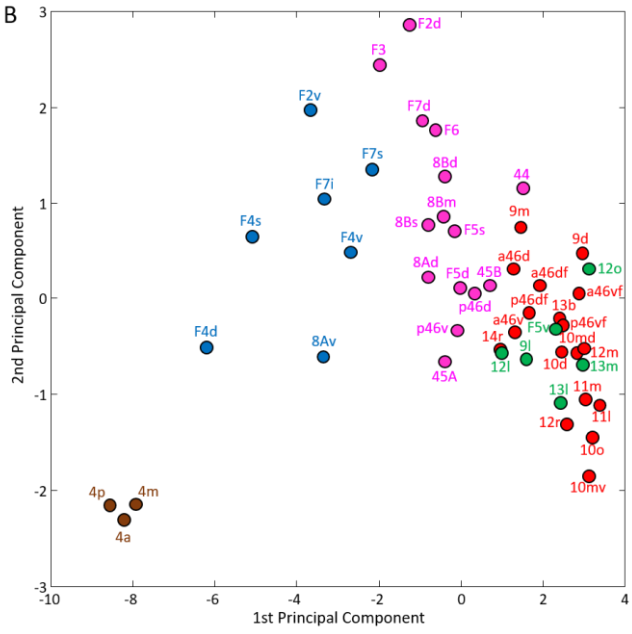

881

Figure 12 Multivariate analyses of the receptor fingerprints in the macaque frontal lobe. The analyses include 33 of the 35 areas identified in the present study (for areas 14c and 13a was not possible to extract receptor densities due to technical limitations), as well as 16 areas of the primary motor and premotor cortex identified in a previous study (Rapan, Froudist-Walsh, et al. 2021) carried out on the same monkey brains. A) Receptor-driven hierarchical clustering and B) principal component analysis (variance 79.8%), where the k-means analysis showed five as the optimal number of clusters. Above the hierarchical dendrogram, the extent and location of the five clusters are depicted on the medial, lateral and orbital surface of the Yerkes19 atlas. Clusters were named according the main functional characteristics of the areas they encompass, and color coded based on the corresponding color on the dendrogram.

did so with area 45A. Areas 45B and 44 share most similarities in receptor densities with the adjacent premotor areas F5s and F5d.

- **Cluster 4** comprises all subdivisions in and the around the spur of the arcuate sulcus, i.e., prefrontal area 8Av and premotor areas F7s, F7i, F2v, F4s, F4d and F4v.
- **Cluster 5** is the most homogeneous cluster of all, since it consists of subdivisions of the primary motor cortex, areas 4p, 4a and 4m.

A principal component analysis was carried out to reduce the 14-dimensional space resulting from the analysis of 14 different receptors area to a 2-dimensional plot (**Fig. 12B**). Differences in the 1st principal component revealed a rostro-caudal trend driven by the gradual decrease in size of the receptor fingerprints. Consequently, subdivisions of area 4 (4m, 4a and 4p) are segregated from the rest of the frontal areas, since their fingerprints are the smallest among all analysed areas (present data, (Rapan, Froudist-Walsh, et al. 2021). In contrast, areas of clusters 1 and 2 present the highest receptor concentration levels. The 2nd principal component further segregated primary motor areas (Cluster 5) from the premotor ones (Cluster 4 and 3), as well as rostral prefrontal areas (Clusters 1 and 2) from the posterior ones (Cluster 3) (**Fig. 12B**). The 1st and 2nd principal components did not segregate areas located in clusters 1 and 2.

3.4 Functional connectivity analysis

In addition to distinct cyto- and receptor architectonic features, areas have also been characterized by their functional connectivity pattern. The results of the analysis

of the functional correlation of each identified prefrontal area with a total of 111 cyto- and receptor architectonically identified areas of the (pre)motor, cingulate, somatosensory, parietal and occipital cortex are depicted in **Figures 13-17**. The array of the functional connectivity pattern for each prefrontal area was displayed on the Yerkes19 surface ($z < 0.25$, **Figs. 13A-17A**), and in the form of circular plots, which depict strongest correlations found ($z > 0.2$, **Figs. 13B-17B**). Additionally, to facilitate the description and interpretation of our results, we created summary figures emphasizing interareal connections (between subdivisions belonging to same area) as well as the most prominent connectivity correlation patterns of each subdivision (**Supp. Figs. 12 and 13**).

Areas 10. Lateral frontopolar areas 10d and 10o present more restricted functional connectivity pattern than medial areas 10md and 10mv (**Fig. 13A**), apart from the weak correlation between 10d and areas a46d and a46v. Contrary, medial areas 10md and 10mv share strong connectivity with cingulate cortex, i.e., dorsally located area 10md with p32, while ventral area 10mv was correlated with s32 and to a lesser extent with p32. Further differences are found, since 10md has stronger connectivity with dorsal and lateral PFC, while 10mv is more strongly correlated to orbital area 14r and ventral prefrontal area 45A (**Fig. 13B; Supp. Fig. 12**). Within the frontal polar region, dorsal areas were more strongly connected with each other than with their ventral counterparts, which also presented a strong correlation between each other (**Supp. Fig. 12**).

Areas 14. Rostral subdivision of area 14 (area 14r) has more prominent functional correlation with medial PFC and anterior cingulate cortex (ACC) than caudally located area 14c, which is strongly correlated with caudal orbital and rostral temporal cortex (**Fig. 13A**). Besides strong connection to 10mv, area 14r is connected to orbital area 13b and cingulate areas 25 and s32. The strongest correlation of area 14c was with areas 25 and 13a, and, to lesser extent, with area 13b (**Fig. 13B; Supp. Fig. 12**). Subdivisions of area 14 show weaker connectivity among each other than to their corresponding adjacent areas (**Supp. Fig. 12**).

Areas 11. Both subdivisions of area 11 displayed similar functional connectivity pattern across the cortex (**Fig. 13A**), however they differed by their regional interconnections (**Fig. 13B; Supp. Fig. 12**). In particular we found strong correlation

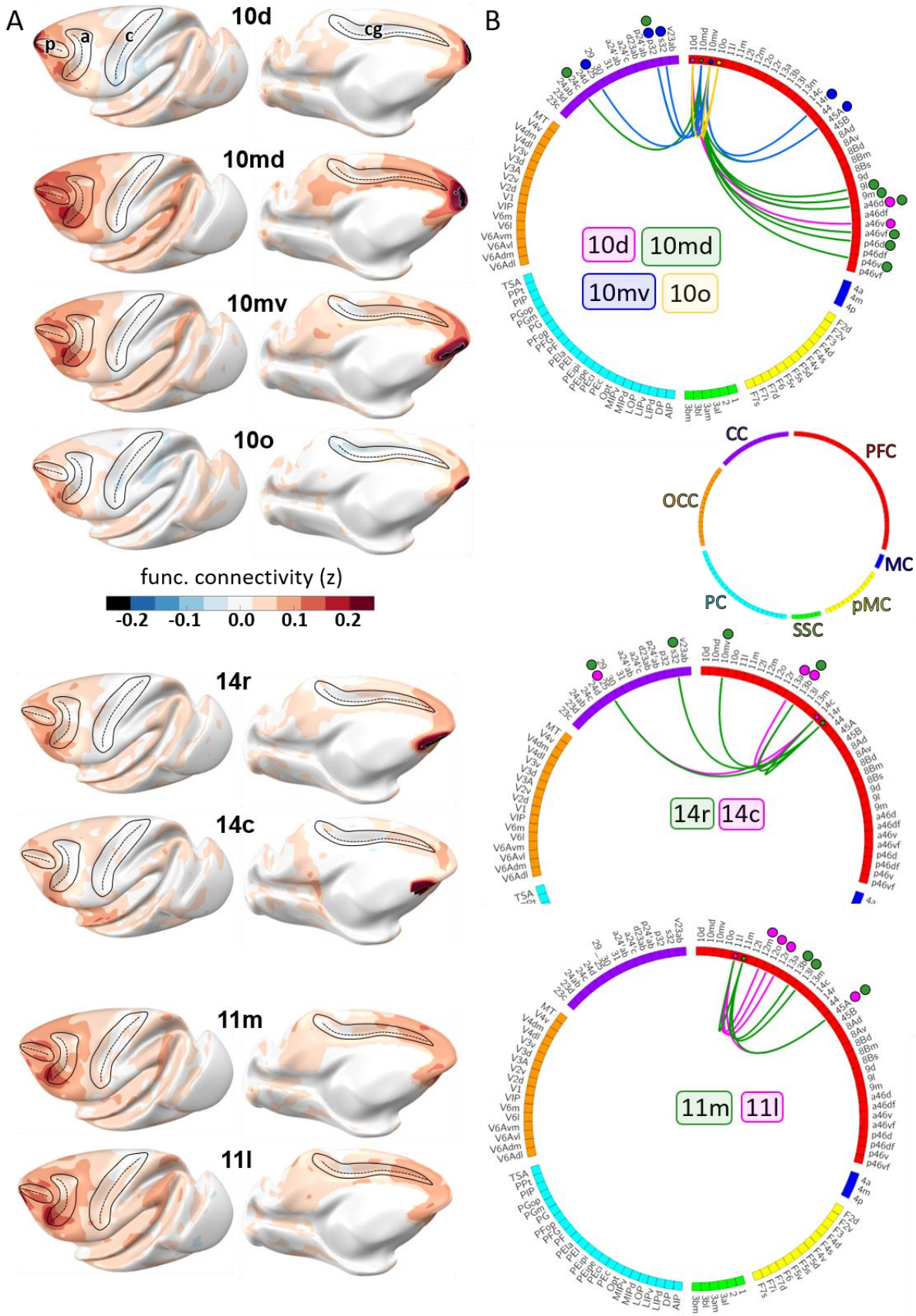

947

948 **Figure 13** A) Results of the functional connectivity analysis depicted on the Yerkes19 surface for areas
949 10, 14 and 11. Scale bar codes for the functional connectivity coefficient (z). B) Strongest functional

connections (z > 0.2) shown on the circular plot for each subdivision. Colored dots correspond to color associate with labelled areas in the plot. Each cortical region shown in distinct color; red for prefrontal cortex (PFC), dark blue for motor cortex (MC), yellow for premotor cortex (pMC), green for somatosensory cortex (SSC), light blue for parietal cortex (PC), orange for occipital cortex (OCC) and purple for cingulate cortex (CC). a – arcuate sulcus; c – central sulcus; cg – cingulate sulcus; p – principal sulcus.

between area 11l and its laterally neighbouring areas 12r, 12m and 12o, whereas area 11m was more strongly correlated with medially adjacent area 13b, and to a lesser extent with area 13l. Finally, both areas 11 are connected to ventrolateral area 45A (**Fig. 13B; Supp. Fig. 12**).

Areas 13. Among subdivisions of area 13, we found that medially located area 13a has most restricted connectivity pattern, whereby most laterally positioned area 13l show opposite trend (**Fig. 14A**). Interestingly, these two areas revealed weakest interconnectivity among each other (**Supp. Fig. 12**). Rather, area 13a show strong connections to adjoining subdivisions 13b and 14c, whereby the strongest connectivity for area 13l is found to be with surrounding areas 13m and 12o (**Fig. 14B; Supp. Fig. 12**). Additionally, area 13l revealed strong connectivity to posterior prefrontal region, in particular to areas 45A, p46d and p46v (**Fig. 14B; Supp. Fig. 12**).

Areas 12. All subdivisions of area 12 presented a widespread functional connectivity pattern (**Fig. 14A**). This was particularly true for area 12r, which showed strong correlation to lateral areas 46, ventral areas 45A and 45B, as well as a correlation, although weaker, with premotor areas F5 (**Fig. 14B; Supp. Fig. 12**). Interareal connectivity pattern showed a weak correlation between area 12l and the rest of the area 12, which share strong functional connectivity among each other (**Supp. Fig. 12**). The strongest connections of 12l are found with areas 45A, 13l and p46v (**Fig. 14B; Supp. Fig. 12**).

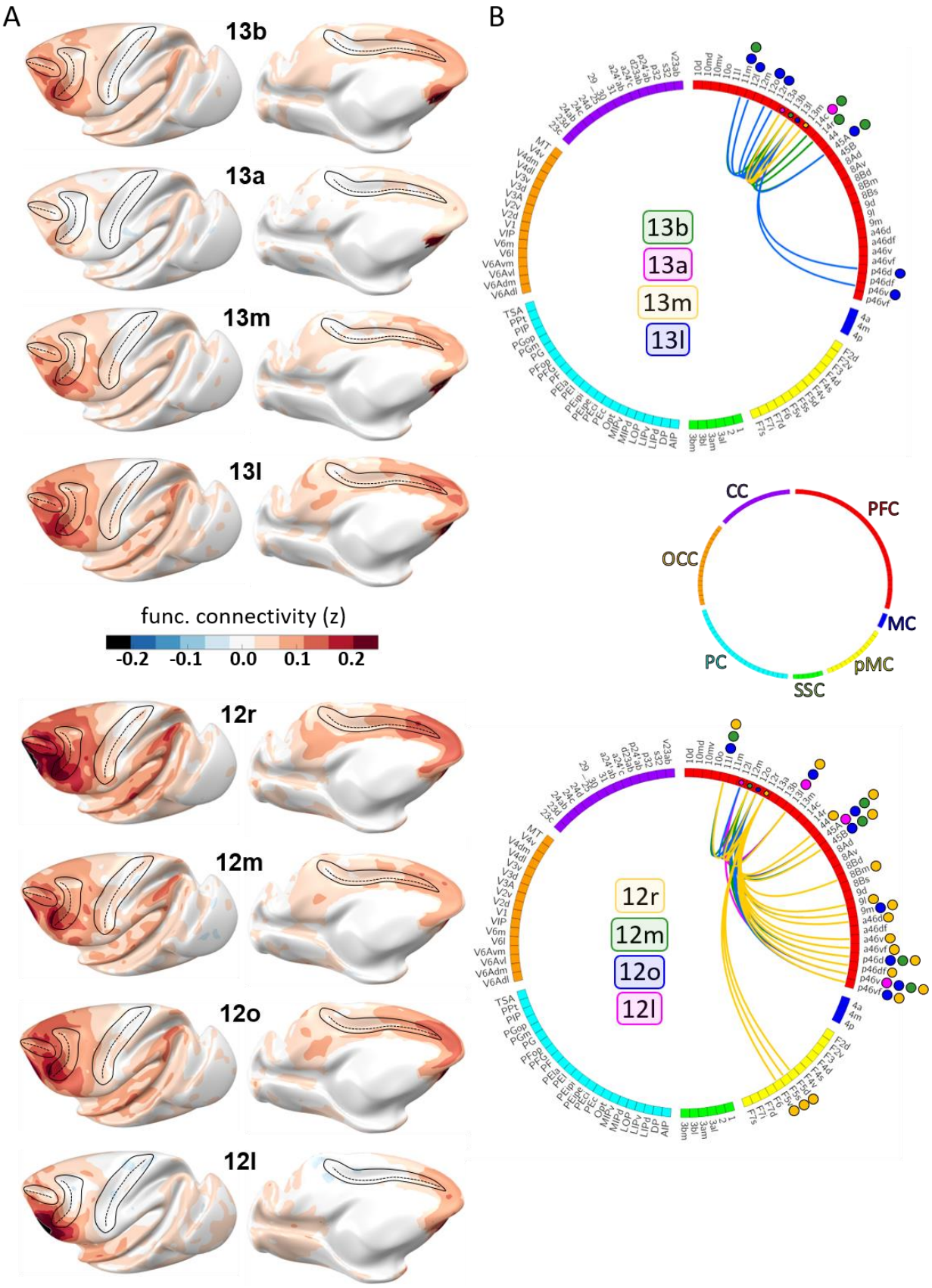

977

978 **Figure 14** A) Results of the functional connectivity analysis depicted on the Yerkes19 surface for areas
979 13 and 12. Scale bar codes for the functional connectivity coefficient. B) Strongest functional

connections (z > 0.2) shown on the circular plot for each subdivision. Colored dots correspond to color associate with labelled areas in the plot. Each cortical region shown in distinct color; red for prefrontal cortex (PFC), dark blue for motor cortex (MC), yellow for premotor cortex (pMC), green for somatosensory cortex (SSC), light blue for parietal cortex (PC), orange for occipital cortex (OCC) and purple for cingulate cortex (CC). a – arcuate sulcus; c – central sulcus; cg – cingulate sulcus; p – principal sulcus.

Areas 9 and 8B. On the dorsolateral prefrontal cortex, rostro-caudal differences can be recognized between functional connectivity pattern of areas 9m, 9d and 9l rostrally, and more caudally located areas 8Bm, 8Bd and 8Bs, which displayed a more widespread connectivity pattern with various distinct areas in the prefrontal, premotor, parietal and medial occipital cortex (**Fig. 15**). While dorso-lateral subdivisions of areas 9 and 8B are strongly intercorrelated, medial areas 9m and 8Bm showed a stronger connection to their medial neighbouring areas, i.e., 9m to its adjacent cingulate area 24c, and 8Bm to surrounding areas a24'c and F6 (**Fig. 15B; Supp. Fig. 13**). Among all subdivisions of area 9, only medial area 9m shows strong functional connectivity with premotor cortex, in particular areas F6, F3, F2v and F5s (**Fig. 15B**). Moreover, area 9l has strong functional connectivity with areas a46d and a46v, medial and dorsal subdivisions 9m and 9d area more strongly correlated with p46d (**Fig. 15B; Supp. Fig. 13**). All subdivisions of area 8B share strong functional connectivity with their surrounding prefrontal areas, parietal area Opt and adjacent premotor areas F6 and F7. But opposite is found in regard to their connectivity with frontopolar, orbital and somatosensory areas (**Fig. 15B**). Additionally, only area 8Bs revealed strong functional connectivity with primary motor cortex, i.e., areas 4a and 4m, as well as with medial occipital region, i.e., areas V6Adm and V6Avm (**Fig. 15B**).

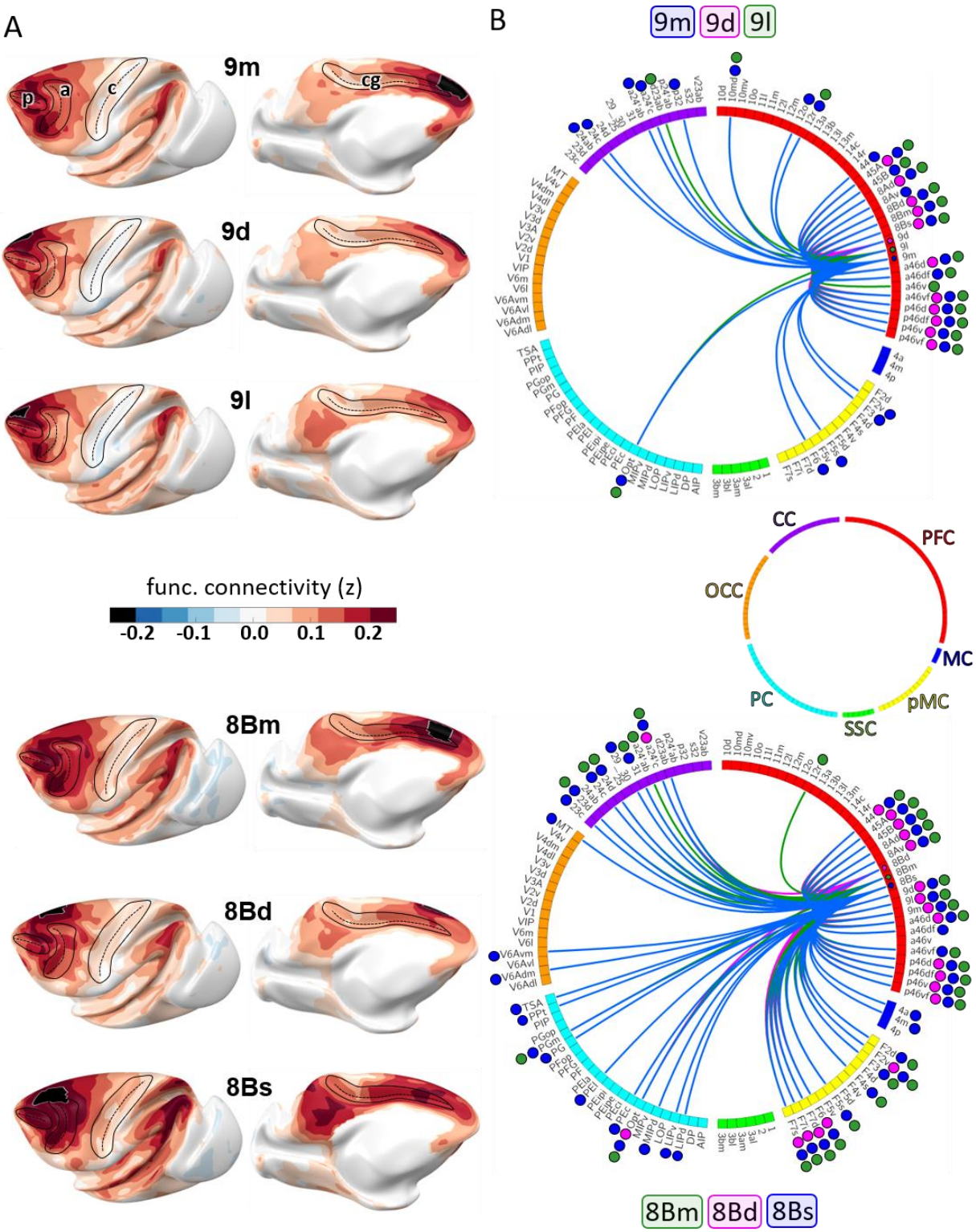

Figure 15 A) Results of the functional connectivity analysis depicted on the Yerkes19 surface for areas 9 and 8B. Scale bar codes for the functional connectivity coefficient. B) Strongest functional connections ($z > 0.2$) shown on the circular plot for each subdivision. Colored dots correspond to color associate with labelled areas in the plot. Each cortical region shown in distinct color; red for prefrontal cortex (PFC), dark blue for motor cortex (MC), yellow for premotor cortex (pMC), green for somatosensory

cortex (SSC), light blue for parietal cortex (PC), orange for occipital cortex (OCC) and purple for cingulate cortex (CC). a – arcuate sulcus; c – central sulcus; cg – cingulate sulcus; p – principal sulcus.

Areas 46. Rostro-caudal differences in functional connectivity patterns were also found for the subdivisions of lateral prefrontal area 46, whereby posterior subdivisions showed a more widespread connectivity pattern with surrounding prefrontal and premotor, as well as with parietal, cingulate and occipital areas, than anterior subdivisions of area 46 (**Fig. 16; Supp. Fig. 13**). Within the *ps*, the anterior and posterior subdivisions of area 46 have a similar intraregional organization, where areas “46d”, “46df” and “46vf” have strong correlations to each other, but for areas “46v”, this is only true with areas “46vf” (**Supp. Fig. 13**). Interestingly, connectivity between areas “46v” and dorsal areas 46 is weaker in the rostral than in the caudal portion of the *ps* (**Supp. Fig. 13**). Furthermore, areas a46v and p46v seem to display opposite correlation trends with the occipital and anterior parietal regions than the remaining subdivisions of area 46. In particular, areas “46v” are positively correlated with multiple areas of the occipital lobe and display a negative correlation in regard to the somatosensory region (**Fig. 16A**).

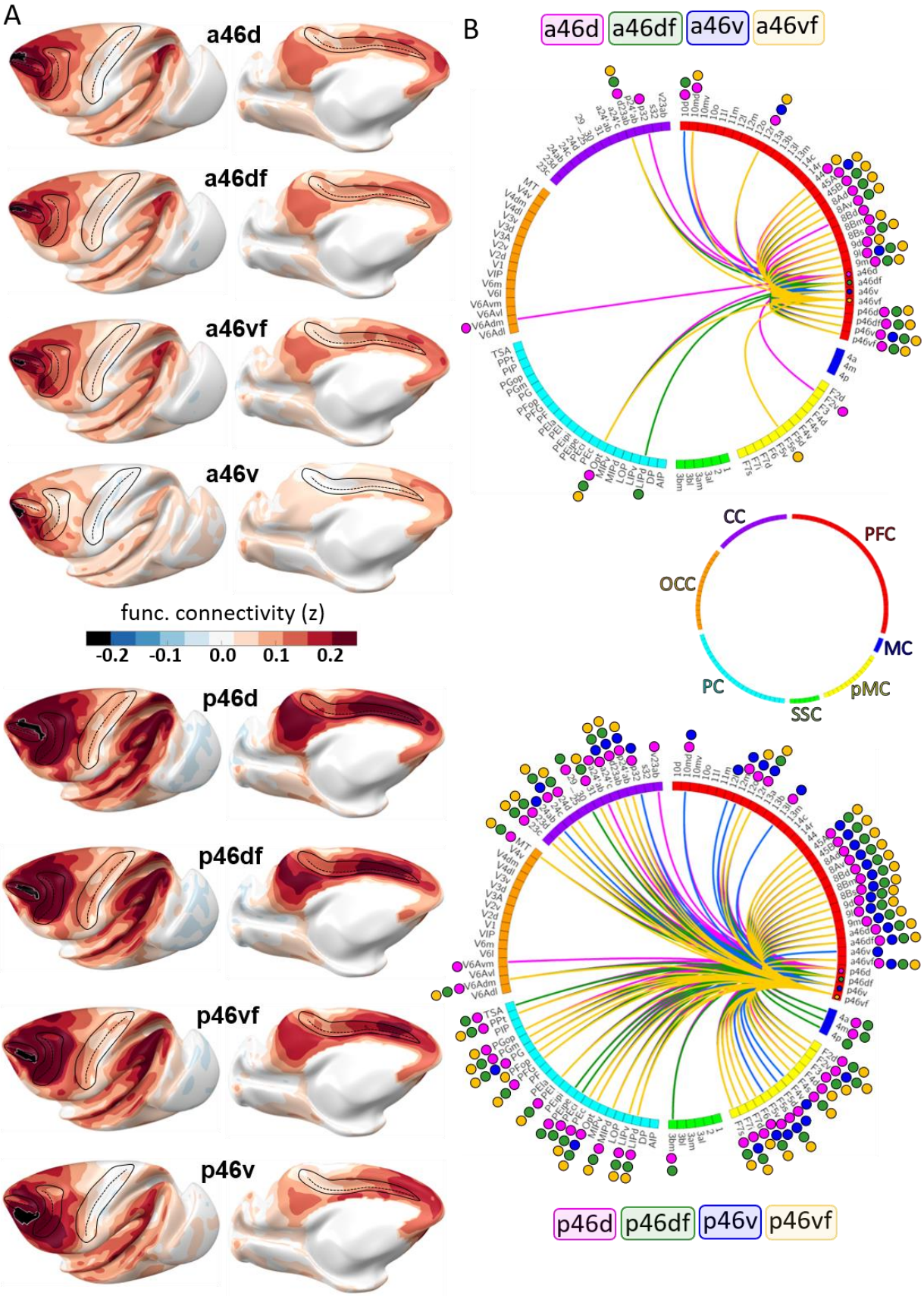

Figure 16 A) Results of the functional connectivity analysis depicted on the Yerkes19 surface for areas "a46" and "p46". Scale bar codes for the functional connectivity coefficient. B) Strongest functional

connections (z > 0.2) shown on the circular plot for each subdivision. Colored dots correspond to color associate with labelled areas in the plot. Each cortical region shown in distinct color; red for prefrontal cortex (PFC), dark blue for motor cortex (MC), yellow for premotor cortex (pMC), green for somatosensory cortex (SSC), light blue for parietal cortex (PC), orange for occipital cortex (OCC) and purple for cingulate cortex (CC). a – arcuate sulcus; c – central sulcus; cg – cingulate sulcus; p – principal sulcus.

Areas 8A, 44 and 45. Within the most posterior portion of the lateral prefrontal cortex, areas 8Ad and 8Av revealed widespread connectivity pattern with region around *ias*, as well as with the cingulate and parietal cortex (**Fig. 17A**). While both subdivisions express similar connectivity pattern across cortex (**Fig. 17B**), we found that area 8Ad was more strongly connected with areas PPt and Pec. In contrast, area 8Av revealed stronger connection with areas PFG and PG (**Supp. Fig. 13**). Ventrolateral areas 45A and 45B have strong interconnection to each other, as well as to surrounding prefrontal and premotor areas (**Fig. 17**). However, while 45B has widespread connectivity throughout the parietal cortex, this was not true for 45A. Instead, we found that area 45A has rather strong correlation with numerous orbital areas (**Fig. 17B; Supp. Fig. 13**). When compared to subdivisions of area 45, the more posteriorly located area 44 exhibits a wider connectivity pattern which includes areas of the prefrontal and premotor as well as areas of parietal and cingulate cortex (**Fig. 17**). Interestingly, area 44 revealed to be connected with primary motor area 4p, located on the anterior wall of the *cs* (**Fig. 17B**).

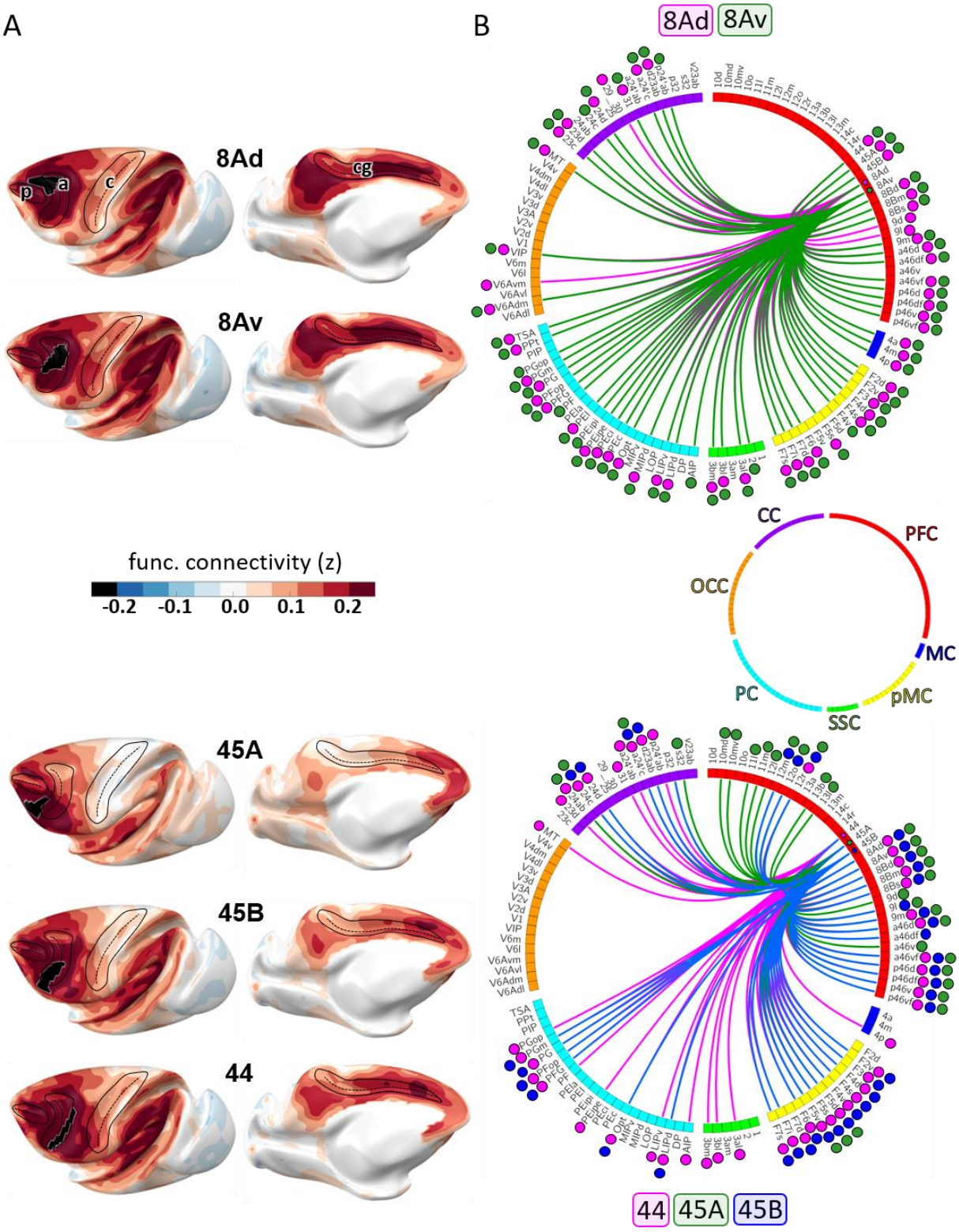

Figure 17 A) Results of the functional connectivity analysis depicted on the Yerkes19 surface for areas 8A, 45 and 44. Scale bar codes for the functional connectivity coefficient. B) Strongest functional connections (z > 0.2) shown on the circular plot for each subdivision. Colored dots correspond to color associate with labelled areas in the plot. Each cortical region shown in distinct color; red for prefrontal cortex (PFC), dark blue for motor cortex (MC), yellow for premotor cortex (pMC), green for

somatosensory cortex (SSC), light blue for parietal cortex (PC), orange for occipital cortex (OCC) and purple for cingulate cortex (CC). a – arcuate sulcus; c – central sulcus; cg – cingulate sulcus; p – principal sulcus.

4 Disscusion

In the present study, we provide a detailed parcellation of the macaque prefrontal cortex (with the exception of the anterior cingulate cortex as a part of the limbic system), and which encompasses 35 cyto- and receptor architectonic areas. The new parcellation scheme integrates and refines former maps of the PFC, particularly concerning area 46 of Walker, and includes novel subdivisions of areas 10 (10mv, 10md, and 10d), 9 (9d and 9l) and 8B (8Bd and 8Bs). It was shown on a 2D flat map to facilitate comparison with previous maps (Barbas and Pandya 1989; Caminiti et al. 2017; Carmichael and Price 1994; Morecraft et al. 2012; Petrides and Pandya 1994, 2002; Preuss and Goldman-Rakic 1991; Walker 1940). Borders were also transferred to the Yerkes19 template (Donahue et al. 2016) to enable an architectonically informed analysis of functional connectivity in the macaque brain.

When analysing changes in receptor densities from area to area, the receptor fingerprints revealed differences across the frontal lobe when moving from rostral to caudal portions. Rostrally located areas contained higher receptor densities, thus bigger receptor fingerprints, than more caudally located areas. These differences in the size of receptor fingerprints seem to be the main force driving clustering of areas as revealed by the multivariate analyses. The analysis of the functional connectivity revealed that subdivisions of area 46, in particular the posterior ones, displayed the most extensive connectivity pattern of the prefrontal region. Areas 45, 44, 8A and 12 also presented a widespread pattern of connectivity with distinct cortical regions across the brain. In contrast, areas 10 and 11 displayed limited functional connectivity with their neighbouring areas, possibly suggesting that these areas are affected by a lower signal-to-noise ratio (Yeo et al. 2011).

4.1 Comparison with previous architectonic maps of macaque prefrontal region

4.1.1 Medial and orbital prefrontal regions (areas 10, 11, 14, 13 and 12)

Walker (Walker 1940) identified five relatively large cytoarchitectonic areas on the medial and orbital prefrontal cortex, i.e., area 10 located on the frontal pole and encroaching onto the orbital surface, area 11 on the rostral orbitolateral surface, caudal areas 13 and 12 on the medial and lateral orbital surface, and area 14 located

on the ventromedial convexity. Preuss and Goldmann-Rakic (Preuss and Goldman-Rakic 1991) identified subdivisions in areas 13 (labelled as 13L and 13M) and 14 (defined as 14A, 14L and 14M), whereas Carmichael and Price (Carmichael and Price 1994) published a more detailed map, which also included cytoarchitectonic subdivisions of areas 10 and 11, and is in accordance with the connectional diversity of this region (Carmichael and Price 1996). We were able to confirm all areas defined by Carmichael and Price (Carmichael and Price 1994), except for those located in the frontal pole region (area 10 of Walker). Their map of the rostral granular area 10 displays areas 10m, located on the medial and dorsal surface of the hemisphere, and 10o, occupying the orbital surface of the medioventral gyrus, and delimited caudally by area 14r (Carmichael and Price 1994). Our cyto- and receptor analyses confirmed the location and extent of area 10o. But it revealed the existence of three subdivisions within 10m, i.e., medio-dorsal area 10md, medio-ventral 10mv, and area 10d on the dorsal surface of the frontal pole. Interestingly, these novel areas differed, not only in their cyto- and receptor architecture, but also in their functional connectivity. Medial areas 10md and 10mv contrasted from their lateral counterparts 10d and 10o by a strong connectivity with the cingulate cortex, i.e., dorsally located area 10md with p32, and ventrally, 10mv with s32 and to a lesser extent with p32. Interestingly, macaque areas p32 and s32 have established homologies within the human brain, where they have been associated with the processing of emotion (Palomero-Gallagher et al. 2013, 2019; Vogt et al. 2013). Conversely, lateral areas displayed a more spatially restricted pattern of functional connectivity.

Within the orbitofrontal cortex, the present analysis confirmed the position and extent of areas 11l, 11m, 13l, 13m, 13b, 13a, 14r and 14c as identified by Carmichael and Price (Carmichael and Price 1994). We also identified four subdivisions of Walker's area 12, but their spatial relationship differs from that described by Carmichael and Price (Carmichael and Price 1994). In both maps areas 12r and 12m occupy the rostral portion of the lateral orbital cortex, while areas 12l and 12o cover its caudal part. Areas 12r and 12l extend onto the ventrolateral convexity below the *ps*. However, unlike in the map of Carmichael and Price (Carmichael and Price 1994), where 12m abuts areas 12r, 12l *and* 12o, in our parcellation area 12m does not have a common border with 12l, since our area 12r extends further posteriorly than that of Carmichael and Price (Carmichael and Price 1994). The orbitofrontal cortex plays an

important role in a reward processing (e.g., association of stimulus), as well as in emotional and motivational aspects of behaviour (Mishkin and Manning 1978; Rolls 2000; Rolls, Yaxley, and Sienkiewicz 1990; Rudebeck and Murray 2011b, 2011a), whereas the ventrolateral region is associated with working memory for non-spatial tasks, as well as object memory retrieval (Wilson, Scalaidhe, and Goldman-Rakic 1993). In particular, the ventrolateral prefrontal cortex contains visual neurons specialized for the identification of object features (Asaad, Rainer, and Miller 1998; Wilson et al. 1993). This brain region also encompasses our areas 12r and 12l, which express significantly lower α_2 receptor densities than their medial counterparts 12m and 12o, respectively. Furthermore, we found areas 12r, 12m and 12o to be strongly connected, while area 12l, which contained the lowest α_2 receptor density of all subdivisions of area 12, was more strongly associated with area 45A than with the other subdivisions of area 12. Thus, the structural and functional organization of this region seems to be closely related to differences in the interareal levels of α_2 receptors. This is an interesting finding since catecholamine neurotransmitters have been associated with cognitive decline in aged non-human primates (Arnsten and Goldman-Rakic 1985), and in particular α_2 receptor agonists have been shown to improve the delayed response performance test results in macaques (Arnsten, Cai, and Goldman-Rakic 1988).

4.1.2 Dorsolateral prefrontal region (areas 9, 46 and 8B)

The analysis also resulted in a novel and more detailed subdivision within this region in regard to areas 9, 8B and 46 than that described in previous maps (Petrides and Pandya 1999; Preuss and Goldman-Rakic 1991; Walker 1940). It confirmed Petrides and Pandya's (Petrides and Pandya 1999) subdivision of area 8A into dorsal and ventral components. Differences in the receptor architectonic organization of dorsolateral prefrontal areas are particularly obvious when looking at the normalized fingerprints, and significant differences were found between rostral and caudal mediodorsal prefrontal areas 9 and 8B, respectively.

Although some authors confirmed Walker's area 9 (1940; e.g.,(Barbas and Pandya 1989; Carmichael and Price 1994; Morecraft et al. 2012; Petrides and Pandya 1994, 2002), others (e.g., (Caminiti et al. 2017; Preuss and Goldman-Rakic 1991) described a dorsal (9d) part, located on the convexity superior to the principal sulcus,

and a medial (9m) subdivision on the medial surface of the hemisphere, dorsal to the cingulate sulcus. We confirmed the existence of 9m, but identified cyto- and receptor architectonic differences within their area 9d. Here only the most dorsal part was labelled as area 9d, whereas more laterally, we identified the distinct area 9l. Whereas area 9l presented a strong functional connectivity with laterally adjacent area a46d, this was not case for our areas 9d and 9m. These areas were more strongly associated with posterior area p46d. Moreover, dorsal subdivisions 9d and 9l are strongly interconnected. Interestingly, medial area 9m, which has been included in the medial prefrontal network (Carmichael and Price 1996), correlated with anterior cingulate area 24c more strongly than with the other subdivisions of area 9.

Further caudal on the mediodorsal prefrontal surface, a transitional region between granular prefrontal and agranular premotor areas was described, namely dysgranular area 8B of Walker (1940) and Petrides and Pandya (1994), which encompasses areas 8Bm and 8Bd of Preuss and Goldman-Rakic (1991) and Morecraft et al. (2012). Similar to the situation described above for area 9, we were able to confirm the existence of area 8Bm, but we subdivided area 8Bd into a dorsal component located caudal to area 9d (our area 8Bd) and a ventral component 8Bs, which abuts area 9l. Previous maps (e.g., Morecraft et al. 2012; Petrides and Pandya 1994, 2002; Preuss and Goldman-Rakic 1991; Walker 1940) depicted area 8B just rostral to the *sas*. However, the extent of our area 8B includes cortex above *sas* as well. Hence, area 8Bd was also identified on the most dorsal portion of the hemisphere rostral to and above the *sas*. Further lateral on the dorsal surface we identified area 8Bs, which extends onto the dorsal wall of the *sas*. Subdivisions of area 8B do not present a transitional region only by their structural features, but also based on their extensive functional connectivity, since our analysis showed a widespread functional connectivity with prefrontal areas, as well as with the medial and dorsal premotor cortex. Dorsal prefrontal cortex, which is occupied by areas 9 and 8B, is involved in orientating processes and joint attention in primate brain (Petrides and Pandya 1999), which is an important behavioural feature when animals need to integrate stimuli from different sensory modalities in order to select an adequate behavioural response. However, unlike area 9, more posteriorly adjacent mediodorsal area 8B is a prominent target region of the prestriate and the medial parietal cortex (Petrides and Pandya 1999). In particular, neurons in area 8B fire during spontaneous ear and eye

movement, as well as during the processing of auditory information (Bon and Lucchetti 1994), indicating a role of this region in the integration of auditory inputs with ear and eye motor output. In monkeys, ear movement improves localization of different sounds in the environment, whereas in humans this ability is rather shifted to eye-head coordination (Bon and Lucchetti 1994). Thus, it has been suggested that area 8B represents a macaque-specific region which is not present in humans, the so-called premotor ear-eye field (PEEF) (Lucchetti, Lanzilotto, and Bon 2008).

Walker (1940) defined area 46 within and around *ps,* and occupying large portion of the lateral prefrontal surface caudal to area 10, while on the most posterior end of principal sulcus, area 46 was replaced by area 8A. This location of area 46 in the macaque monkey has been confirmed in various anatomical studies (Caminiti et al. 2017; Petrides and Pandya 1994, 2002; Preuss and Goldman-Rakic 1991), however it was widely acknowledged that this large region is not homogenous, and distinct subdivisions with many discrepancies among parcellation schemes were made by different authors. Preuss and Goldman-Rakic (1991) identified four subareas along the principal sulcus. Two areas within the sulcus on the dorsal and ventral wall close to the fundus (inner subareas), areas 46d and 46v respectively, and two areas on the dorsal and ventral shoulders of the sulcus and extending onto the free surface of the hemisphere (outer areas) areas 46dr and 46vr, respectively. Other authors identified rostro-caudal differences within Walker's area 46, but only described a dorso-ventral segregation in the caudal portion, thus resulting in a parcellation with a rostral area 46 and caudal areas 9/46d and 9/46v located on the dorsal and ventral banks of the principal sulcus, respectively, and extending onto the free surface of the hemisphere (Borra et al. 2019; Caminiti et al. 2017; Gerbella et al. 2013; Morecraft et al. 2012; Petrides and Pandya 2006).

The existence of dorso-ventral subdivisions along the entire length of the principal sulcus, proposed by Preuss and Goldman-Rakic (1991) could be corroborated by the present quantitative cyto- and receptor architectonic analysis. The present study confirmed the existence of rostro-caudal differences within the region and resulted in a new parcellation scheme for Walker's area 46 including a total of 8 subdivisions - with areas 'a46' located within the anterior portion of *ps* and areas 'p46' occupying its most caudal. Receptor architectonic differences particularly highlighted borders between inner (subdivisions closer to the fundus, areas '46f') and outer

(subdivisions extending onto surface, areas '46d' and '46v') portions of the principal region. We measured significantly higher levels of α_2 receptors in the inner subdivisions compared to their respective outer areas along the rostro-caudal *ps* axis. Area 46 plays an important role in higher-level cognitive processes, such as working memory (Fuster 2008; Goldman-Rakic 1995; Petrides 2000), which has been reported to decline with age (Arnsten and Goldman-Rakic 1985). Similar to subdivisions of area 12, norepinephrine elicits different responses within area 46, depending on which type of receptor is stimulated. In particular, its binding to α_1 and α_2 receptors can have opposite effects on persistent activity during working memory. Stimulation of α_1 receptors increases feedforward calcium-cAMP signalling, whereas stimulation of α_2 receptors inhibits this process (Arnsten et al. 1988; Arnsten, Datta, and Wang 2021; Arnsten and Jentsch 1997; Hara, Rapp, and Morrison 2012). Calcium-cAMP signalling must be kept within a tight range to support persistent activity, with excessive signalling leading to a shut-down of synaptic activity due to opening of potassium channels (Arnsten et al. 2021). The increase in α_2 receptors in inner subdivisions of area 46 could help keep persistent activity in-check in these areas. In contrast, higher levels of kainate are measured in 'shoulder' areas of the *ps* than in the 'fundus' areas, however only between anterior areas this difference has reached a significant level.

Our subdivision of Walker's area 46 into anterior/posterior and fundal/shoulder regions is further supported by the differences in the functional connectivity patterns of the areas we identified, since posterior subdivisions of area 46 displayed a more widespread connectivity pattern than the anterior areas, and also in regard to all other prefrontal areas. Specifically, anterior areas showed the most prominent correlations with areas of the rostral prefrontal region as well as with their caudal 46 counterparts, while posterior areas strongly correlate with surrounding oculomotor areas in the lateral frontal region, as well as with the inferior parietal cortex and mid to posterior cingulate cortex. Our results are in accordance with previous connectivity analyses of area 46 (Borra et al. 2019; Gerbella et al. 2013), and may be indicative of the role of areas "p46" in the visuospatial and visuomotor control of arm/hand reaching and eye movement, whereas areas "a46" are more strongly involved in higher cognitive processes (Borra et al. 2019; Gerbella et al. 2013). Furthermore, whereas the anterior part of *ps* is a major target of projections from the auditory and limbic cortex, the posterior portion receives topographic sensory inputs from auditory, somatosensory,

visual and polysensory cortex (Hackett et al. 1999). Taken together, these findings clearly suggest that the anterior and posterior portions of cortex within the *ps* are involved in different aspects of behaviour, whereby areas "p46" constitute a multimodal integration centre within the lateral PFC. Additionally, significant differences of kanite and α_2 receptors between 'shoulder' and 'fundus' areas suggest an intermediate role of these receptors on working memory, a higher cognitive function associated with this region.

4.1.3 Caudal region (areas 8Ad, 8Av)

Walker's area 8A has been subject of numerous architectonic analyses, resulting in maps that differ in the number and extent of areas depicted. A region defined as the granular part of area 8 (Morecraft et al. 2012; Walker 1940) is known as the frontal eye field (FEF) (Bruce et al. 1985; Stanton et al. 1989), due to an important role in the eye movement and visual attention. It encompasses cortex rostral to premotor representation of the forelimb and mouth by the arcuate sulcus, from the ventral wall of the *sas*, across the portion of the prearcuate convexity located around the posterior portion of *ps* (where it borders posterior parts of area 46) and extending ventrally to the most caudal part of the anterior wall within the *ias* (where it abuts areas 44 and 45B) (Morecraft et al. 2012; Walker 1940). The results of the present quantitative multimodal analysis are in accordance with the map of Petrides and Pandya (1999, 2006), which identifies dorsal and ventral subdivisions within 8A, and not the tripartite subdivision of area 8A proposed by Preuss and Goldman-Rakic (1991), or the rostro-caudal segregation of Gerbella et al. (2007). Furthermore, contrary to the map of Preuss and Goldman-Rakic (1991), where their area 8Ar extends ventrally along the cortical surface adjacent to the *ias*, where it was delimited rostrally by area 12vl, our results are in accordance with the relative dorsoventral extent of area 8A described by Petrides and Pandya (1999, 2006), since area 8Av could be identified only on the cortical surface adjoining the most rostral portion of the *ias*, and is replaced at this position by area 45A, so that it shares no common border with area 12. Within the dorsal portion of the FEF, which is associated with the larger saccades, an auditory activity is also found (Bruce et al. 1985), thus suggesting that auditory stimuli are used to guide visual localization of the sound source within the environment during the visually guided saccades. Moreover, present receptor architectonic analysis also confirmed dorso-ventral differences between subdivisions of area 8A since

significantly higher kainate, α_1 and 5-HT_{1A} receptor densities were measured in 8Ad than in 8Av. Both subdivisions displayed a widespread connectivity pattern, with strongest correlations in the lateral frontal, parietal and mid to posterior cingulate cortex, similar to the situation found for areas “p46”. Interestingly, both areas 8Av and 8Ad display a strong connectivity with areas p46d, p46df, p46vf, but not with area p46v, whose connectivity pattern also differs from that of remaining ‘p46’ areas by its stronger correlation with the ventrolateral frontal region, but its weaker correlation with the inferior parietal and posterior cingulate cortex. Finally, it is noteworthy that areas 8Av and 8Ad (i.e., the cytoarchitectonic correlates of the functionally defined FEF) were negatively correlated with areas of the occipital lobe, whereas p46v presented a positive correlation with this brain region, indicating that subdivisions of area 8A operate at a higher visual processing level than area p46v.

4.1.4 Ventrolateral region (areas 45A, 45B and 44)

Finally, the ventrolateral region also encompasses areas 44 and 45, which are thought to be the homologs of Broca’s region in humans (Petrides and Pandya 2002). In contrast with the parcellations proposed by Walker (1940) and Preuss and Goldman-Rakic, (1991), Petrides and Pandya (2002), found area 45 to extend rostrally onto the adjacent lateral surface of the hemisphere for a considerable distance, reaching as far as the *ipd*. Previous maps depicted area 45 mainly within the *ias*, and only encroaching onto the free surface, where it was replaced dorsally by area 46 and ventrally by area 12 (in the map of Walker (1940), or rostrally by area 8Ar (in the map of Preuss and Goldman-Rakic 1991). Furthermore, Petrides and Pandya (1994, 1999, 2002) subdivided monkey area 45 into areas 45A and 45B. Area 45A occupies the ventral portion of the prearcuate convexity ventral to area 8Av, and extends rostrally into the *ipd,* where is substituted by 12r dorsally, and ventrally by 12l. Caudally 45A is delimited by 45B, which occupies the rostro-dorsal wall of the *ias*. The subdivision of area 45 was based primarily on differences in the appearance of layer IV (Petrides and Pandya 1994, 1999, 2002). The results of the present quantitative multimodal approach not only support the presence of an area 45, and not of area 12, on the prearcuate convexity, but also confirm the existence of areas 45A and 45B, with higher kainate densities in the former than the latter area.

Our definition of areas 45A and 45B, as well as their functional connectivity patterns are in accordance with a detailed tracer study by Gerbella et al., (2010). Area 45A seems to be associated with vocalization and communication behaviour, whereas area 45B rather plays a role in oculomotor frontal system (Gerbella et al. 2010). Interestingly, we found area 45A, but not 45B to have a strong correlation with premotor areas F5s and F5v, which are supposed to be involved in hand and mouth movements (Fogassi et al. 2001; Maranesi et al. 2012), respectively. Furthermore, by far the strongest correlation between prefrontal areas was found between areas 45B and 44, which also presented the smallest Euclidean distance in the hierarchical clustering analysis. This finding further supports the hypothesis, that similarities in the size and shape of fingerprints constitute the molecular underpinning for brain functions (Zilles et al. 2015; Zilles and Nicola Palomero-Gallagher 2017).

In the past the existence of area 44 has been subject of controversy. Walker (1940) and Preuss and Goldman-Rakic, (1991) did not identify an area 44 in their maps, because they considered that area 45 not only occupied the rostral, but also the caudal wall of the *ias*. Similarly, Matelli *et al.* (1985) did not identify area 44 either, since they thought that their area F5 continues rostrally into the *ias*, where it was followed by area 45. Petrides and Pandya (Petrides et al. 2012; Petrides and Pandya 1994) identified a distinct dysgranular area between the caudally adjacent agranular premotor cortex and granular area 45, and this is supported by our structural (cyto- and receptor architecture) and functional connectivity analyses. Furthermore, tracer studies (Cavada and Goldman-Rakic 1989; Matelli et al. 1986; Petrides and Pandya 1984), which are in accordance with our functional connectivity results, showed that area 44 differs from the posteriorly adjacent ventral premotor cortex by its cortico-cortical projections to the parietal region. Whilst the ventral premotor region shares strong reciprocal connections with the most anterior areas of the inferior parietal lobule (IPL), in particular with area PE (Cavada and Goldman-Rakic 1989; Matelli et al. 1986; Petrides and Pandya 1984), area 44 of the monkey brain is linked with the most posterior areas PFG and PG of the inferior parietal lobe (Petrides and Pandya 2009). Thus, macaque area 44 serves as an important region for the integration of different inputs, thus in order to supports the role of area 45B in oculomotor control (Gerbella et al. 2010), since its functional connectivity pattern displayed a widespread correlation with premotor, parietal and cingulate areas.

4.2 Receptor-driven structural organization of the macaque PFC reveals distinct functional domains within the region

The present multivariate analysis of the receptor fingerprints of prefrontal and (pre)motor areas revealed antero-posterior differences between frontal areas, in particular regarding the size of the receptor fingerprints. Thus, areas grouped within clusters 1 and 2 (i.e., areas of rostral PFC) have larger fingerprints, i.e., show higher concentration of receptors, than areas in clusters 3, 4 and 5 (i.e., areas of the caudal PFC, the premotor cortex, and the primary motor cortex). In addition to this global anterior-posterior segregation, prefrontal areas seem to form clusters around areas 46, 8A, 45 and 12, which displayed widespread connectivity patterns within the prefrontal region. These findings are in correspondence with the proposal that these four areas constitute highly influential regions within the lateral and orbital PFC regions, and play an essential role in mediating between distinct neuronal networks, thus modulating the corresponding functional domains within that region (Goulas, Uylings, and Stiers 2014; Ispolatov and Maslov 2008). Therefore, the extensive network of cortico-cortical connections within areas of the PFC as well as of these areas with multiple other brain regions seems to enable the integration of information within and between functional networks (Yeterian et al. 2012).

4.2.1 Areas of Cluster 1

Cluster 1 encompasses most of the rostrally positioned prefrontal areas, which share dense reciprocal connections with the limbic and auditory cortex (Hackett et al. 1999; Romanski 2007), and also includes areas p46df and p46vf, which are located more posteriorly within the *ps*. The medial orbitofrontal cortex (OFC) is associated with value comparison, since it shares reciprocal connections with brain regions involved in similar aspects of reward-guided behaviour (Price 2007), and is a primary source of visceromotor inputs via reciprocal projections to the hypothalamus and brain stem (Carmichael and Price 1994). Lesion studies of the medial OFC in the macaque brain, in particular to area 14, showed animals to be enticed into making incorrect choices, indicating that the decision-making process within the medial OFC is rather associated with motivation, than with action-like behaviour (Noonan et al. 2010; Rudebeck and

Murray 2011b). Since we found strong functional correlation between areas 10mv and 14r, it is interesting that most of the adjacent areas, such as 10o, 10mv and 11m, showed significantly higher levels of inhibitory receptors (i.e., $GABA_A$ and $GABA_A$/BZ), but, only area 10mv contained significantly higher levels of AMPA in regard to 14r. Additionally, similar to the medial frontopolar cortex, we found area 14r to have a strong functional connectivity with the anterior cingulate cortex, in particular to area 25. In contrast, connections of the lateral OFC to high order sensory areas, such as the anterior temporal and perirhinal cortex (Carmichael and Price 1994; Price 2007), indicate that this region plays an important role in the reward-associated behaviour by assigning a value to stimuli. Animals with lesions in the rostrolateral OFC were unable to learn when to ascribe a different value when a new object is introduced, thus highlighting the importance of this region in value learning (Noonan et al. 2010). Although the medial and lateral orbitofrontal regions display distinct connectional patterns with distant cortical and subcortical structures, they also share numerous reciprocal connections which are thought to support the exchange and integration of information (Carmichael and Price 1994). Specifically, areas 14r, 14c, 13a, 11m and 12o serve as “intermediary” areas connecting the lateral and medial OFC networks (Carmichael and Price 1994; Price 2007).

Microstimulation recordings revealed presence of the auditory-responsive neurons within the caudal *ps* (Hackett et al. 1999; Ito 1981; Watanabe 1992), although most input from the auditory cortex targets the rostral portion of *ps* (Barbas and Mesulam 1985) and, in particular, the frontopolar region (Medalla and Barbas 2014). In the present study we only analysed functional connectivity patterns of cyto- and receptor architectonically identified areas with areas, and these currently do not include the temporal lobe. Therefore, we were not able to confirm this integration of auditory information in frontolateral areas. However, out multivariate analyses grouped together subdivisions of area 10, anterior parts of area 46, as well as caudal fundal portions of area 46, which are known to be targeted by the auditory cortex (Barbas and Mesulam 1985; Hackett et al. 1999; Medalla and Barbas 2014).

Thus, the orbitofrontal cortex provides an information on the object-value and motivation (Carmichael and Price 1994; Noonan et al. 2010; Price 2007; Romanski 2007; Rudebeck and Murray 2011a) which is then further processed by distinct regions in the medial and lateral PFC (Goulas et al. 2014). In addition, the dorsal prefrontal

cortex, which is occupied by subdivisions of area 9 (also found in Cluster 1) is involved in orientating processes and joint attention in the primate brain, which is an important feature when the animal processes and integrates stimuli from different sensory modalities in order to select the adequate behavioural response (Petrides and Pandya 1999). Thus, PFC areas which we found to be grouped within cluster 1 based on similarities in their receptor fingerprints are involved in distinct aspects of reward-guided behaviour.

4.2.2 Areas of Cluster 2

Cluster 2 is composed of closely grouped areas located in the posterior orbital PFC, i.e., areas 13m, 13l, 12o, 12l. It also contains dorsolateral prefrontal area 9l and premotor area F5v, located on the ventral portion of the postarcuate convexity, with which orbital areas do not share common borders. This is interesting, since area F5v is mostly associated with mouth movements (Maranesi et al. 2012), and shares strong cortico-cortical connections with ventrally adjacent area ProM, as well as with the gustatory, orbitofrontal, insular and somatosensory cortex (Maranesi et al. 2012), indicating an important role of this area in a feeding-related behaviour (Cipolloni and Pandya 1999). While areas of the posterior orbital PFC, and in particular subdivisions of area 13, represent a multimodal region, which is targeted by the gustatory visual, auditory, somatosensory and olfactory cortex, as well as by the amygdala, which assigns an emotional value to the integrated stimuli (Barbas 2007).

Our functional connectivity analysis showed that newly identified area 9l has a strong correlation with multimodal area 46, in particular with area a46d, and to a lesser extent with area p46v. Thus, area 9l may serve as bridge between two multimodal regions of the orbital and lateral PFC. Furthermore, electrophysiological recordings from of a brain region which topologically corresponds to our areas 9l and 9d revealed that it contains neurons which are activated solely during voluntary head rotation, and neurons which are also activated when the head rotation is observed in another individual (mirror-like neurons), indicating that area 9 mediates head movements associated with social settings (Lanzilotto et al. 2017).

4.2.3 Areas of Cluster 3

Cluster 3 encompasses all subdivisions of area 8B, area 8Ad, ventrolateral areas 45A, 45B and 44, areas occupying the posterior shoulder of *ps* (i.e., p46d, p46v),

ventral premotor F5s and F5d, as well as medial and dorsal premotor areas F6, F3, F7d and F2d. Medial area F6 plays an important role in controlling when and how to execute complex motor plan (Matelli, Luppino, and Rizzolatti 1991), but it lacks direct connections to the primary motor areas, as well as the spinal cord (Dum and Strick 2002; Luppino et al. 1993), thus its contribution to movement is mediated via its dense connections with other premotor areas (e.g., F3, F2d). Present functional analysis also revealed strong correlation between areas F6 and its rostrally adjacent area 8Bm. In general, area 8B is a prominent target region of the prestriate and the medial parietal cortex (Petrides and Pandya 1999), and constitutes the cytoarchitectonic correlate of the functionally identified premotor ear-eye field (PEEF) (Lucchetti et al. 2008), which is involved in auditory stimuli recognition and orientation processes (Bon and Lucchetti 1994; Lanzilotto et al. 2013). Since neurons in area 8B fire during spontaneous ear and eye movement, as well as during auditory information processing, indicating a role of this region in the integration of auditory inputs with ear and eye motor output, this area is thought to be monkey specific, and have no homolog in the human brain (Bon and Lucchetti 1994; Lanzilotto et al. 2013). In monkeys, ear movement improves localization of different sounds in the environment, whereas in humans this ability is rather shifted to eye-head coordination (Bon and Lucchetti 1994).

Our novel architectonic subdivisions of area 8B presented different functional connectivity profiles. The functional connectivity profile of 8Bd is limited to adjacent areas on the dorsal portion of the PFC (e.g., areas 9d and F7d), whereas area 8Bs has a more widespread connectivity pattern which includes more ventrally located 8Ad and F7s. Furthermore, our cyto- and receptor architectonic results support the classification of area 8B as a transitional region between the prefrontal and the premotor cortex, since the subdivisions of area 8B (which are dysgranular) showed a closer receptor architectonic relationship with premotor (agranular) than with the remaining prefrontal (granular) areas. This is particularly true for 8Bd and area F7d, a premotor area associated with the supplementary eye field (SEF) (Schlag and Schlag-Rey 1987) as well as for 8Bs with area 8Ad, which is part of the frontal eye field (FEF), another region specialized for visual attention (Amiez and Petrides 2009), but also contributes, together with 8Bs, to auditory responses (Bruce and Goldberg 1985). The most prominent difference found between SEF and FEF is that saccades evoked from the latter region are of fixed vectors, whereas microstimulation recordings revealed

evidence for the representation of eye position in SEF (Mitz and Godschalk 1989; Schlag and Schlag-Rey 1987).

The present functional connectivity analysis revealed a strong correlation between areas 8Ad and p46d, which is in agreement with previous tracer studies (Barbas and Mesulam 1981, 1985; Barbas and Pandya 1989). In general, input from the principalis region to the FEF may mediate regulatory control over gaze (Schall 1997). Areas located in cluster 3 also receive projections from the auditory cortex (Gerbella et al. 2010; Romanski et al. 1999; Romanski and Averbeck 2009). However, whereas areas of cluster 1 are targeted by the rostral parabelt region, input to areas in cluster 3 originates in the caudal parable region. The posterior ventral cortex, which encompasses areas 45A (part of cluster 3) and 12l, shows evidence of overlapping auditory and visual responsive regions (Romanski and Goldman-Rakic 2002; Wilson et al. 1993), indicating that convergent input enables responses to both stimuli, especially when processing of information related to face and vocalization communication is associated with the recognition of familiar and unfamiliar faces (Romanski 2007). Finally, areas 45B and 44, located within the *ias*, are associated with the oculomotor control (Gerbella et al. 2010). In addition, present functional analysis showed that posterior area 44 has strong connection to neighbouring premotor area F5s, which, actually, presents the highest correlation found between two areas in our study. Therewith, ventral premotor areas F5s and F5d represent hand movements and are involved in object grasping (Fogassi et al. 2001). In particular, area F5s (defined as area F5a by Belmalih et al. 2009) is associated with stereoscopic analysis of the 3D object (Fogassi et al. 2001).

Thus, within cluster 3, we find caudal prefrontal areas associated with the attention and orientation based on the distinct visual and auditory inputs, whereas premotor areas grouped here are involved in arm reaching and orientation, with a main focus on a hand grasping (Gerbella, Rozzi, and Rizzolatti 2017).

4.2.4 Areas of Cluster 4

Cluster 4 contains area 8Av and premotor areas F7i, F7s, F2v, F4s, F4d an F4v. As mentioned above, area 8Av is part of FEF, which is largely associated with saccades (Bruce et al. 1985). Due to the unique receptor architectonic features of the ventral portion of area 8A, indicated by the smallest receptor fingerprint of all prefrontal

areas, we found a clear differentiation between 8Av and almost all surrounding prefrontal areas, where all significant receptor types were lower in 8Av. Thus, area 8Av was found to be more comparable to posteriorly adjacent premotor areas located within and around *arcs*, which are also characterized by relatively small fingerprints. This is interesting, since fMRI studies of macaque behaviour involving voluntary saccadic eye movement reported a bilateral activation of both the rostral and caudal banks of *arcs*, as well as of cortex within the spur of this sulcus (Baker et al. 2006; Koyama et al. 2004) That is, activations were found in a region which is thought to be part of an extended oculomotor region (Amiez and Petrides 2009) associated with visual pursuit (Fukushima et al. 2002), and which is largely occupied by the areas composing our cluster 4. In particular, premotor areas of the extended oculomotor region are thought to play a role in blinking movement (Bruce et al. 1985) and in coordinating eye-arm movements within the peripersonal space (Fujii, Mushiake, and Tanji 1998).

4.2.5 Areas of Cluster 5

Finally, primary motor areas 4m, 4a and 4p demonstrated greater dissimilarity of their receptor fingerprints in regard to rest of the frontal areas and formed segregated cluster. Indeed, these areas are characterized by the one of the smallest receptor fingerprints among all areas identified in the present study. Previous analysis of subdivisions of area 4 of our own group (Rapan, Froudist-Walsh, et al. 2021), revealed differences in cyto- and receptor architecture as well as functional connectivity between area 4p, located mainly on the anterior bank of the central sulcus, and two other motor subdivisions, occupying the precentral convexity and medial surface of the hemisphere. In particular, area 4p showed strong functional corelation to the somatosensory area 7b (Andersen, Asanuma, et al. 1990), whereas areas 4m and 4a showed higher correlations with areas area 7a and 7m, which are involved in visuomotor coordination (Andersen, Asanuma, et al. 1990; Andersen, Bracewell, et al. 1990). Unlike medial and dorsolateral subdivisions, cortex occupied by area 4p has a higher packing density of the cortico-motor neurons (Rathelot and Strick 2009), associated with the fine movements, such as the independent finger movement (Porter and Lemon 1995). Theses neuros is also play a role in a mapping of a new motor outline, which would enable performance of an additional skill (Rathelot and Strick 2009). Since prefrontal area 44 revealed to be strongly connected with areas in

premotor cortex associated with a hand movement, it is interesting that it also has strong functional connectivity with motor area 4p.

5 Conclusion

The benefit of the present comprehensive study of the primate frontal cortex comes from its multimodal and quantitative architectonic approach, in combination with a functional connectivity analysis. Thus, we anticipate that resulting parcellation and 3D map will be useful tool for neuroscientific community, since it is incorporated with information about principles of structural and functional organization in the macaque frontal lobe. Providing a strong anatomical and neurochemical foundation for the analysis and interpretation of primate fMRI data. In addition, all data obtained here are publicly available for broad scientific community via the EBRAINS platform of the Human Brain Project and the BALSA repository.

Acknowledgements

This project has received funding from the European Union's Horizon 2020 Research and Innovation Programme under the Specific Grant Agreements 785907 (Human Brain Project SGA2) and 945539 (Human Brain Project SGA3), from the Federal Ministry of Education and Research (BMBF) under project number 01GQ1902, from the National Institute of Health (NIH) under grant number R01MH122024-02, and from the Helmholtz Association's Initiative and Networking Fund through the Helmholtz International BigBrain Analytics and Learning Laboratory (HIBALL) under the Helmholtz International Lab grant agreement InterLabs-0015.

Author contributions

Lucija Rapan: Investigation, Validation, Visualization, Writing – Original Draft; **Sean Froudist-Walsh**: Conceptualization, Software, Writing – Review and Editing; **Meiqi Niu**: Formal Analysis, Data Curation, Visualization, Writing – Review and Editing; **Ting Xu**: Resources, Data Curation, Writing – Review and Editing; **Ling Zhao**: Formal Analysis, Data Curation, Visualization, Writing – Review and Editing; **Thomas Funck**: Formal Analysis; **Xiao-Jing Wang**: Writing – Review and Editing; **Nicola Palomero-Gallagher**: Conceptualization, Resources, Data Curation, Supervision, Writing – Review and Editing, Project Administration

Conflict of Interest Statement

The authors declare that the research was conducted in the absence of any commercial or financial relationships that could be acknowledged as a potential conflict of interest.

6 References

Amiez, Céline, and Michael Petrides. 2009. "Anatomical Organization of the Eye Fields in the Human and Non-Human Primate Frontal Cortex." *Progress in Neurobiology* 89(2):220–30. doi: 10.1016/j.pneurobio.2009.07.010.

Andersen, R. A., C. Asanuma, G. Essick, and R. M. Siegel. 1990. "Corticocortical Connections of Anatomically and Physiologically Defined Subdivisions within the Inferior Parietal Lobule." *Journal of Comparative Neurology* 296(1):65–113. doi: 10.1002/cne.902960106.

Andersen, R. A., R. M. Bracewell, S. Barash, J. W. Gnadt, and L. Fogassi. 1990. "Eye Position Effects on Visual, Memory, and Saccade-Related Activity in Areas LIP and 7a of Macaque." *Journal of Neuroscience* 10(4):1176–96. doi: 10.1523/JNEUROSCI.10-04-01176.1990.

Arnsten, A. F., J. X. Cai, and P. S. Goldman-Rakic. 1988. "The Alpha-2 Adrenergic Agonist Guanfacine Improves Memory in Aged Monkeys without Sedative or Hypotensive Side Effects: Evidence for Alpha-2 Receptor Subtypes." *Journal of Neuroscience* 8(11):4287–98. doi: 10.1523/JNEUROSCI.08-11-04287.1988.

Arnsten, A. F., and J. D. Jentsch. 1997. "The Alpha-1 Adrenergic Agonist, Cirazoline, Impairs Spatial Working Memory Performance in Aged Monkeys." *Pharmacology, Biochemistry, and Behavior* 58(1):55–59. doi: 10.1016/s0091-3057(96)00477-7.

Arnsten, Amy F. T., Dibyadeep Datta, and Min Wang. 2021. "The Genie in the Bottle-Magnified Calcium Signaling in Dorsolateral Prefrontal Cortex." *Molecular Psychiatry* 26(8):3684–3700. doi: 10.1038/s41380-020-00973-3.

Arnsten, Amy F. T., and Patricia S. Goldman-Rakic. 1985. "A2-Adrenergic Mechanisms in Prefrontal Cortex Associated with Cognitive Decline in Aged Nonhuman Primates." *Science* 230(4731):1273–76. doi: 10.1126/science.2999977.

Asaad, Wael F., Gregor Rainer, and Earl K. Miller. 1998. "Neural Activity in the Primate Prefrontal Cortex during Associative Learning." *Neuron* 21(6):1399–1407. doi: 10.1016/S0896-6273(00)80658-3.

Autio, Joonas A., Matthew F. Glasser, Takayuki Ose, Chad J. Donahue, Matteo Bastiani, Masahiro Ohno, Yoshihiko Kawabata, Yuta Urushibata, Katsutoshi Murata, Kantaro Nishigori, Masataka Yamaguchi, Yuki Hori, Atsushi Yoshida, Yasuhiro Go, Timothy S. Coalson, Saad Jbabdi, Stamatios N. Sotiropoulos, Henry Kennedy, Stephen Smith, David C. Van Essen, and Takuya Hayashi. 2020. "Towards HCP-Style Macaque Connectomes: 24-Channel 3T Multi-Array Coil, MRI Sequences and Preprocessing." *NeuroImage* 215:116800. doi: 10.1016/j.neuroimage.2020.116800.

Baker, Justin T., Gaurav H. Patel, Maurizio Corbetta, and Lawrence H. Snyder. 2006. "Distribution of Activity Across the Monkey Cerebral Cortical Surface, Thalamus and Midbrain during Rapid, Visually Guided Saccades." *Cerebral Cortex* 16(4):447–59. doi: 10.1093/cercor/bhi124.

Barbas, H., and M. M. Mesulam. 1981. "Organization of Afferent Input to Subdivisions of Area 8 in the Rhesus Monkey." *The Journal of Comparative Neurology* 200(3):407–31. doi: 10.1002/cne.902000309.

Barbas, H., and M. M. Mesulam. 1985. "Cortical Afferent Input to the Principals Region of the Rhesus Monkey." *Neuroscience* 15(3):619–37. doi: 10.1016/0306-4522(85)90064-8.

Barbas, H., and D. N. Pandya. 1989. "Architecture and Intrinsic Connections of the Prefrontal Cortex in the Rhesus Monkey." *The Journal of Comparative Neurology* 286(3):353–75. doi: 10.1002/cne.902860306.

Barbas, Helen. 2007. "Specialized Elements of Orbitofrontal Cortex in Primates." *Annals of the New York Academy of Sciences* 1121:10–32. doi: 10.1196/annals.1401.015.

Belmalih, Abdelouahed, Elena Borra, Massimo Contini, Marzio Gerbella, Stefano Rozzi, and Giuseppe Luppino. 2009. "Multimodal Architectonic Subdivision of the Rostral Part (Area F5) of the Macaque Ventral Premotor Cortex." *The Journal of Comparative Neurology* 512(2):183–217. doi: 10.1002/cne.21892.

Benjamini, Yoav, and Yosef Hochberg. 1995. "Controlling the False Discovery Rate: A Practical and Powerful Approach to Multiple Testing." *Journal of the Royal Statistical Society: Series B (Methodological)* 57(1):289–300. doi: 10.1111/j.2517-6161.1995.tb02031.x.

Bon, L., and C. Lucchetti. 1994. "Ear and Eye Representation in the Frontal Cortex, Area 8b, of the Macaque Monkey: An Electrophysiological Study." *Experimental Brain Research* 102(2):259–71. doi: 10.1007/BF00227513.

Borra, Elena, Carolina Giulia Ferroni, Marzio Gerbella, Valentina Giorgetti, Chiara Mangiaracina, Stefano Rozzi, and Giuseppe Luppino. 2019. "Rostro-Caudal Connectional Heterogeneity of the Dorsal Part of the Macaque Prefrontal Area 46." *Cerebral Cortex (New York, N.Y.: 1991)* 29(2):485–504. doi: 10.1093/cercor/bhx332.

Brodmann, K. 1905. "Lokalization Der Grosshirnrinde. III. Mitteilung: Die Rindenfelder Der Niederen Affen." 4:177–226.

Brodmann, K. 1909. "Vergleichende Lokalisationslehre Der Grosshirnrinde in Ihren Prinzipien Dargestellt Auf Grund Des Zellenbaues."

Bruce, C. J., and M. E. Goldberg. 1985. "Primate Frontal Eye Fields. I. Single Neurons Discharging before Saccades." *Journal of Neurophysiology* 53(3):603–35. doi: 10.1152/jn.1985.53.3.603.

Bruce, C. J., M. E. Goldberg, M. C. Bushnell, and G. B. Stanton. 1985. "Primate Frontal Eye Fields. II. Physiological and Anatomical Correlates of Electrically Evoked Eye Movements." *Journal of Neurophysiology* 54(3):714–34. doi: 10.1152/jn.1985.54.3.714.

Caminiti, Roberto, Elena Borra, Federica Visco-Comandini, Alexandra Battaglia-Mayer, Bruno B. Averbeck, and Giuseppe Luppino. 2017. "Computational Architecture of the Parieto-Frontal Network Underlying Cognitive-Motor Control in Monkeys." *ENeuro* 4(1):ENEURO.0306-16.2017. doi: 10.1523/ENEURO.0306-16.2017.

Carmichael, S. T., and J. L. Price. 1994. "Architectonic Subdivision of the Orbital and Medial Prefrontal Cortex in the Macaque Monkey." *The Journal of Comparative Neurology* 346(3):366–402. doi: 10.1002/cne.903460305.

Carmichael, S. T., and J. L. Price. 1996. "Connectional Networks within the Orbital and Medial Prefrontal Cortex of Macaque Monkeys." *The Journal of Comparative Neurology* 371(2):179–207. doi: 10.1002/(SICI)1096-9861(19960722)371:2<179::AID-CNE1>3.0.CO;2-#.

Cavada, C., and P. S. Goldman-Rakic. 1989. "Posterior Parietal Cortex in Rhesus Monkey: II. Evidence for Segregated Corticocortical Networks Linking Sensory and Limbic Areas with the Frontal Lobe." *The Journal of Comparative Neurology* 287(4):422–45. doi: 10.1002/cne.902870403.

Cipolloni, P. B., and D. N. Pandya. 1999. "Cortical Connections of the Frontoparietal Opercular Areas in the Rhesus Monkey." *The Journal of Comparative Neurology* 403(4):431–58.

DeFelipe, Javier. 2015. "The Anatomical Problem Posed by Brain Complexity and Size: A Potential Solution." *Frontiers in Neuroanatomy* 9.

Donahue, Chad J., Stamatios N. Sotiropoulos, Saad Jbabdi, Moises Hernandez-Fernandez, Timothy E. Behrens, Tim B. Dyrby, Timothy Coalson, Henry Kennedy, Kenneth Knoblauch, David C. Van Essen, and Matthew F. Glasser. 2016. "Using Diffusion Tractography to Predict Cortical Connection Strength and Distance: A Quantitative Comparison with Tracers in the Monkey." *Journal of Neuroscience* 36(25):6758–70. doi: 10.1523/JNEUROSCI.0493-16.2016.

Dum, Richard P., and Peter L. Strick. 2002. "Motor Areas in the Frontal Lobe of the Primate." *Physiology & Behavior* 77(4–5):677–82. doi: 10.1016/s0031-9384(02)00929-0.

Fogassi, L., V. Gallese, G. Buccino, L. Craighero, L. Fadiga, and G. Rizzolatti. 2001. "Cortical Mechanism for the Visual Guidance of Hand Grasping Movements in the Monkey: A Reversible Inactivation Study." *Brain: A Journal of Neurology* 124(Pt 3):571–86. doi: 10.1093/brain/124.3.571.

Fujii, Naotaka, Hajime Mushiake, and Jun Tanji. 1998. "An Oculomotor Representation Area within the Ventral Premotor Cortex." *Proceedings of the National Academy of Sciences* 95(20):12034–37. doi: 10.1073/pnas.95.20.12034.

Fukushima, Kikuro, Takanobu Yamanobe, Yasuhiro Shinmei, and Junko Fukushima. 2002. "Predictive Responses of Periarcuate Pursuit Neurons to Visual Target Motion." *Experimental Brain Research* 145(1):104–20. doi: 10.1007/s00221-002-1088-7.

Fuster, Joaquin M. 2008. *The Prefrontal Cortex*. 4th ed. Amsterdam Boston: Academic Press/Elsevier.

Gerbella, Marzio, Abdelouahed Belmalih, Elena Borra, Stefano Rozzi, and Giuseppe Luppino. 2007. "Multimodal Architectonic Subdivision of the Caudal Ventrolateral Prefrontal Cortex of the Macaque Monkey." *Brain Structure & Function* 212(3–4):269–301. doi: 10.1007/s00429-007-0158-9.

Gerbella, Marzio, Abdelouahed Belmalih, Elena Borra, Stefano Rozzi, and Giuseppe Luppino. 2010. "Cortical Connections of the Macaque Caudal Ventrolateral Prefrontal Areas 45A and 45B." *Cerebral Cortex (New York, N.Y.: 1991)* 20(1):141–68. doi: 10.1093/cercor/bhp087.

Gerbella, Marzio, Elena Borra, Simone Tonelli, Stefano Rozzi, and Giuseppe Luppino. 2013. "Connectional Heterogeneity of the Ventral Part of the Macaque Area 46." *Cerebral Cortex (New York, N.Y.: 1991)* 23(4):967–87. doi: 10.1093/cercor/bhs096.

Gerbella, Marzio, Stefano Rozzi, and Giacomo Rizzolatti. 2017. "The Extended Object-Grasping Network." *Experimental Brain Research* 235(10):2903–16. doi: 10.1007/s00221-017-5007-3.

Goldman-Rakic, P. S. 1995. "Cellular Basis of Working Memory." *Neuron* 14(3):477–85. doi: 10.1016/0896-6273(95)90304-6.

Goulas, Alexandros, Harry B. M. Uylings, and Peter Stiers. 2014. "Mapping the Hierarchical Layout of the Structural Network of the Macaque Prefrontal Cortex." *Cerebral Cortex* 24(5):1178–94. doi: 10.1093/cercor/bhs399.

Hackett, T. A., I. Stepniewska, and J. H. Kaas. 1999. "Prefrontal Connections of the Parabelt Auditory Cortex in Macaque Monkeys." *Brain Research* 817(1–2):45–58. doi: 10.1016/s0006-8993(98)01182-2.

Hara, Yuko, Peter R. Rapp, and John H. Morrison. 2012. "Neuronal and Morphological Bases of Cognitive Decline in Aged Rhesus Monkeys." *Age (Dordrecht, Netherlands)* 34(5):1051–73. doi: 10.1007/s11357-011-9278-5.

Herkenham, M., A. B. Lynn, M. D. Little, M. R. Johnson, L. S. Melvin, B. R. de Costa, and K. C. Rice. 1990. "Cannabinoid Receptor Localization in Brain." *Proceedings of the National Academy of Sciences of the United States of America* 87(5):1932–36.

Impieri, Daniele, Karl Zilles, Meiqi Niu, Lucija Rapan, Nicole Schubert, Claudio Galletti, and Nicola Palomero-Gallagher. 2019. "Receptor Density Pattern Confirms and Enhances the Anatomic-Functional Features of the Macaque Superior Parietal Lobule Areas." *Brain Structure & Function* 224(8):2733–56. doi: 10.1007/s00429-019-01930-9.

Ispolatov, Iaroslav, and Sergei Maslov. 2008. "Detection of the Dominant Direction of Information Flow and Feedback Links in Densely Interconnected Regulatory Networks." *BMC Bioinformatics* 9:424. doi: 10.1186/1471-2105-9-424.

Ito, Shin-ichi. 1981. "Prefrontal Unit Activity of Macaque Monkeys during Auditory and Visual Reaction Time Tasks."

Koyama, Minoru, Isao Hasegawa, Takahiro Osada, Yusuke Adachi, Kiyoshi Nakahara, and Yasushi Miyashita. 2004. "Functional Magnetic Resonance Imaging of Macaque Monkeys Performing Visually Guided Saccade Tasks: Comparison of Cortical Eye Fields with Humans." *Neuron* 41(5):795–807. doi: 10.1016/s0896-6273(04)00047-9.

Lanzilotto, M., M. Gerbella, V. Perciavalle, and C. Lucchetti. 2017. "Neuronal Encoding of Self and Others' Head Rotation in the Macaque Dorsal Prefrontal Cortex." *Scientific Reports* 7(1):8571. doi: 10.1038/s41598-017-08936-5.

Lanzilotto, M., V. Perciavalle, and C. Lucchetti. 2013. "A New Field in Monkey's Frontal Cortex: Premotor Ear-Eye Field (PEEF)." *Neuroscience and Biobehavioral Reviews* 37(8):1434–44. doi: 10.1016/j.neubiorev.2013.05.010.

Lucchetti, C., M. Lanzilotto, and L. Bon. 2008. "Auditory-Motor and Cognitive Aspects in Area 8B of Macaque Monkey's Frontal Cortex: A Premotor Ear-Eye Field (PEEF)." *Experimental Brain Research* 186(1):131–41. doi: 10.1007/s00221-007-1216-5.

Luppino, G., M. Matelli, R. Camarda, and G. Rizzolatti. 1993. "Corticocortical Connections of Area F3 (SMA-Proper) and Area F6 (Pre-SMA) in the Macaque Monkey." *The Journal of Comparative Neurology* 338(1):114–40. doi: 10.1002/cne.903380109.

Mahalanobis, P. C., D. N. Majumdar, M. W. M. Yeatts, and C. Radhakrishna Rao. 1949. "Anthropometric Survey of the United Provinces, 1941: A Statistical Study." *Sankhyā: The Indian Journal of Statistics (1933-1960)* 9(2/3):89–324.

Maranesi, Monica, Francesca Rodà, Luca Bonini, Stefano Rozzi, Pier Francesco Ferrari, Leonardo Fogassi, and Gino Coudé. 2012. "Anatomo-Functional Organization of the Ventral Primary Motor and Premotor Cortex in the Macaque Monkey." *The European Journal of Neuroscience* 36(10):3376–87. doi: 10.1111/j.1460-9568.2012.08252.x.

Matelli, M., R. Camarda, M. Glickstein, and G. Rizzolatti. 1986. "Afferent and Efferent Projections of the Inferior Area 6 in the Macaque Monkey." *The Journal of Comparative Neurology* 251(3):281–98. doi: 10.1002/cne.902510302.

Matelli, M., G. Luppino, and G. Rizzolatti. 1991. "Architecture of superior and mesial area 6 and the adjacent cingulate cortex in the macaque monkey." *Journal of Comparative Neurology* 311(4):445–62. doi: 10.1002/cne.903110402.

Medalla, Maria, and Helen Barbas. 2014. "Specialized Prefrontal 'Auditory Fields': Organization of Primate Prefrontal-Temporal Pathways." *Frontiers in Neuroscience* 8:77. doi: 10.3389/fnins.2014.00077.

Merker, B. 1983. "Silver Staining of Cell Bodies by Means of Physical Development." *Journal of Neuroscience Methods* 9(3):235–41.

Milham, Michael P., R. Cameron Craddock, Jake J. Son, Michael Fleischmann, Jon Clucas, Helen Xu, Bonhwang Koo, Anirudh Krishnakumar, Bharat B. Biswal, F. Xavier Castellanos, Stan Colcombe, Adriana Di Martino, Xi-Nian Zuo, and Arno Klein. 2018. "Assessment of the Impact of Shared Brain Imaging Data on the Scientific Literature." *Nature Communications* 9(1):2818. doi: 10.1038/s41467-018-04976-1.

Milham, Michael, Christopher I. Petkov, Daniel S. Margulies, Charles E. Schroeder, Michele A. Basso, Pascal Belin, Damien A. Fair, Andrew Fox, Sabine Kastner, Rogier B. Mars, Adam Messinger, Colline Poirier, Wim Vanduffel, David C. Van Essen, Ashkan Alvand, Yannick Becker, Suliann Ben Hamed, Austin Benn, Clementine Bodin, Susann Boretius, Bastien Cagna, Olivier Coulon, Sherif Hamdy El-Gohary, Henry Evrard, Stephanie J. Forkel, Patrick Friedrich, Sean Froudist-Walsh, Eduardo A. Garza-Villarreal, Yang Gao, Alessandro Gozzi, Antoine Grigis, Renee Hartig, Takuya Hayashi, Katja Heuer, Henrietta Howells, Dirk Jan Ardesch, Béchir Jarraya, Wendy Jarrett, Hank P. Jedema, Igor Kagan, Clare Kelly, Henry Kennedy, P. Christiaan Klink, Sze Chai Kwok, Robert Leech, Xiaojin Liu, Christopher Madan, Wasana Madushanka, Piotr Majka, Ann-Marie Mallon, Kevin Marche, Adrien Meguerditchian, Ravi S. Menon, Hugo Merchant, Anna Mitchell, Karl-Heinz Nenning, Aki Nikolaidis, Michael Ortiz-Rios, Marco Pagani, Vikas Pareek, Mark Prescott, Emmanuel Procyk, Reza Rajimehr, Ioana-Sabina Rautu, Amir Raz, Anna Wang Roe, Román Rossi-Pool, Lea Roumazeilles, Tomoko Sakai, Jerome Sallet, Pamela García-Saldivar, Chika Sato, Stephen Sawiak, Marike Schiffer, Caspar M. Schwiedrzik, Jakob Seidlitz, Julien Sein, Zhi-ming Shen, Amir Shmuel, Afonso C. Silva, Luciano Simone, Nikoloz Sirmpilatze, Julia Sliwa, Jonathan Smallwood, Jordy Tasserie, Michel Thiebaut de Schotten, Roberto Toro, Regis Trapeau, Lynn Uhrig, Julien Vezoli, Zheng Wang, Sara Wells, Bella Williams, Ting Xu, Augix Guohua Xu, Essa Yacoub, Ming Zhan, Lei Ai, Céline Amiez, Fabien Balezeau, Mark G. Baxter, Erwin L. A. Blezer, Thomas Brochier, Aihua Chen, Paula L. Croxson, Christienne G. Damatac, Stanislas Dehaene, Stefan Everling, Lazar Fleysher, Winrich Freiwald, Timothy D. Griffiths, Carole Guedj, Fadila Hadj-Bouziane, Noam Harel, Bassem Hiba, Benjamin Jung, Bonhwang Koo, Kevin N. Laland, David A. Leopold, Patrik Lindenfors, Martine Meunier, Kelvin

Mok, John H. Morrison, Jennifer Nacef, Jamie Nagy, Mark Pinsk, Simon M. Reader, Pieter R. Roelfsema, David A. Rudko, Matthew F. S. Rushworth, Brian E. Russ, Michael Christoph Schmid, Elinor L. Sullivan, Alexander Thiele, Orlin S. Todorov, Doris Tsao, Leslie Ungerleider, Charles R. E. Wilson, Frank Q. Ye, Wilbert Zarco, and Yong-di Zhou. 2020. "Accelerating the Evolution of Nonhuman Primate Neuroimaging." *Neuron* 105(4):600–603. doi: 10.1016/j.neuron.2019.12.023.

Mishkin, M., and F. J. Manning. 1978. "Non-Spatial Memory after Selective Prefrontal Lesions in Monkeys." *Brain Research* 143(2):313–23. doi: 10.1016/0006-8993(78)90571-1.

Mitz, A. R., and M. Godschalk. 1989. "Eye-Movement Representation in the Frontal Lobe of Rhesus Monkeys." *Neuroscience Letters* 106(1–2):157–62. doi: 10.1016/0304-3940(89)90219-x.

Morecraft, R. J., K. S. Stilwell-Morecraft, P. B. Cipolloni, J. Ge, D. W. McNeal, and D. N. Pandya. 2012. "Cytoarchitecture and Cortical Connections of the Anterior Cingulate and Adjacent Somatomotor Fields in the Rhesus Monkey." *Brain Research Bulletin* 87(4–5):457–97. doi: 10.1016/j.brainresbull.2011.12.005.

Niu, Meiqi, Lucija Rapan, Thomas Funck, Seán Froudist-Walsh, Ling Zhao, Karl Zilles, and Nicola Palomero-Gallagher. 2021. "Organization of the Macaque Monkey Inferior Parietal Lobule Based on Multimodal Receptor Architectonics." *NeuroImage* 231:117843. doi: 10.1016/j.neuroimage.2021.117843.

Noonan, M. P., M. E. Walton, T. E. J. Behrens, J. Sallet, M. J. Buckley, and M. F. S. Rushworth. 2010. "Separate Value Comparison and Learning Mechanisms in Macaque Medial and Lateral Orbitofrontal Cortex." *Proceedings of the National Academy of Sciences* 107(47):20547–52. doi: 10.1073/pnas.1012246107.

Palomero-Gallagher, Nicola, Felix Hoffstaedter, Hartmut Mohlberg, Simon B. Eickhoff, Katrin Amunts, and Karl Zilles. 2019. "Human Pregenual Anterior Cingulate Cortex: Structural, Functional, and Connectional Heterogeneity." *Cerebral Cortex (New York, N.Y.: 1991)* 29(6):2552–74. doi: 10.1093/cercor/bhy124.

Palomero-Gallagher, Nicola, Brent A. Vogt, Axel Schleicher, Helen S. Mayberg, and Karl Zilles. 2009. "Receptor Architecture of Human Cingulate Cortex: Evaluation of the Four-Region Neurobiological Model." *Human Brain Mapping* 30(8):2336–55. doi: 10.1002/hbm.20667.

Palomero-Gallagher, Nicola, and Karl Zilles. 2018. "Cyto- and Receptor Architectonic Mapping of the Human Brain." *Handbook of Clinical Neurology* 150:355–87. doi: 10.1016/B978-0-444-63639-3.00024-4.

Palomero-Gallagher, Nicola, and Karl Zilles. 2019. "Cortical Layers: Cyto-, Myelo-, Receptor- and Synaptic Architecture in Human Cortical Areas." *NeuroImage* 197:716–41. doi: 10.1016/j.neuroimage.2017.08.035.

Palomero-Gallagher, Nicola, Karl Zilles, Axel Schleicher, and Brent A. Vogt. 2013. "Cyto- and Receptor Architecture of Area 32 in Human and Macaque Brains." *The Journal of Comparative Neurology* 521(14):3272–86. doi: 10.1002/cne.23346.

Passingham, Richard. 2009. "How Good Is the Macaque Monkey Model of the Human Brain?" *Current Opinion in Neurobiology* 19(1):6–11. doi: 10.1016/j.conb.2009.01.002.

Petrides, M., and D. N. Pandya. 1984. "Projections to the Frontal Cortex from the Posterior Parietal Region in the Rhesus Monkey." *The Journal of Comparative Neurology* 228(1):105–16. doi: 10.1002/cne.902280110.

Petrides, M., and D. N. Pandya. 1999. "Dorsolateral Prefrontal Cortex: Comparative Cytoarchitectonic Analysis in the Human and the Macaque Brain and Corticocortical Connection Patterns." *The European Journal of Neuroscience* 11(3):1011–36. doi: 10.1046/j.1460-9568.1999.00518.x.

Petrides, M., and D. N. Pandya. 2002. "Comparative Cytoarchitectonic Analysis of the Human and the Macaque Ventrolateral Prefrontal Cortex and Corticocortical Connection Patterns in the Monkey." *The European Journal of Neuroscience* 16(2):291–310. doi: 10.1046/j.1460-9568.2001.02090.x.

Petrides, M., and D. N. Pandya. 2006. "Efferent Association Pathways Originating in the Caudal Prefrontal Cortex in the Macaque Monkey." *The Journal of Comparative Neurology* 498(2):227–51. doi: 10.1002/cne.21048.

Petrides, Michael. 2000. "Dissociable Roles of Mid-Dorsolateral Prefrontal and Anterior Inferotemporal Cortex in Visual Working Memory." *Journal of Neuroscience* 20(19):7496–7503. doi: 10.1523/JNEUROSCI.20-19-07496.2000.

Petrides, Michael. 2005. "Lateral Prefrontal Cortex: Architectonic and Functional Organization." *Philosophical Transactions of the Royal Society of London. Series B, Biological Sciences* 360(1456):781–95. doi: 10.1098/rstb.2005.1631.

Petrides, Michael, and Deepak N. Pandya. 1994. "Comparative Architectonic Analysis of the Human and the Macaque Frontal Cortex." Pp. 17–58 in *Handbook of Neuropsychology*. Amsterdam: Elsevier.

Petrides, Michael, and Deepak N. Pandya. 2009. "Distinct Parietal and Temporal Pathways to the Homologues of Broca's Area in the Monkey." *PLOS Biology* 7(8):e1000170. doi: 10.1371/journal.pbio.1000170.

Petrides, Michael, Francesco Tomaiuolo, Edward H. Yeterian, and Deepak N. Pandya. 2012. "The Prefrontal Cortex: Comparative Architectonic Organization in the Human and the Macaque Monkey Brains." *Cortex* 48(1):46–57. doi: 10.1016/j.cortex.2011.07.002.

Porter, Robert, and Roger Lemon. 1995. *Corticospinal Function and Voluntary Movement*. Oxford: Oxford University Press.

Preuss, T. M., and P. S. Goldman-Rakic. 1991. "Myelo- and Cytoarchitecture of the Granular Frontal Cortex and Surrounding Regions in the Strepsirhine Primate Galago and the Anthropoid Primate Macaca." *The Journal of Comparative Neurology* 310(4):429–74. doi: 10.1002/cne.903100402.

Price, Joseph L. 2007. "Definition of the Orbital Cortex in Relation to Specific Connections with Limbic and Visceral Structures and Other Cortical Regions." *Annals of the New York Academy of Sciences* 1121(1):54–71. doi: 10.1196/annals.1401.008.

Rapan, Lucija, Sean Froudist-Walsh, Meiqi Niu, Ting Xu, Thomas Funck, Karl Zilles, and Nicola Palomero-Gallagher. 2021. "Multimodal 3D Atlas of the Macaque Monkey Motor and Premotor Cortex." *NeuroImage* 226:117574. doi: 10.1016/j.neuroimage.2020.117574.

Rapan, Lucija, Meiqi Niu, Ling Zhao, Thomas Funck, Katrin Amunts, Karl Zilles, and Nicola Palomero-Gallagher. 2021. "Receptor Architecture of Macaque and Human Early Visual Areas: Not Equal, but Comparable." *Brain Structure & Function*. doi: 10.1007/s00429-021-02437-y.

Rathelot, Jean-Alban, and Peter L. Strick. 2009. "Subdivisions of Primary Motor Cortex Based on Cortico-Motoneuronal Cells." *Proceedings of the National Academy of Sciences of the United States of America* 106(3):918–23. doi: 10.1073/pnas.0808362106.

Rolls, E. T. 2000. "The Orbitofrontal Cortex and Reward." *Cerebral Cortex (New York, N.Y.: 1991)* 10(3):284–94. doi: 10.1093/cercor/10.3.284.

Rolls, E. T., S. Yaxley, and Z. J. Sienkiewicz. 1990. "Gustatory Responses of Single Neurons in the Caudolateral Orbitofrontal Cortex of the Macaque Monkey." *Journal of Neurophysiology* 64(4):1055–66. doi: 10.1152/jn.1990.64.4.1055.

Romanski, L. M., B. Tian, J. Fritz, M. Mishkin, P. S. Goldman-Rakic, and J. P. Rauschecker. 1999. "Dual Streams of Auditory Afferents Target Multiple Domains in the Primate Prefrontal Cortex." *Nature Neuroscience* 2(12):1131–36. doi: 10.1038/16056.

Romanski, Lizabeth M. 2007. "Representation and Integration of Auditory and Visual Stimuli in the Primate Ventral Lateral Prefrontal Cortex." *Cerebral Cortex (New York, N.Y.: 1991)* 17 Suppl 1:i61-69. doi: 10.1093/cercor/bhm099.

Romanski, Lizabeth M., and Bruno B. Averbeck. 2009. "The Primate Cortical Auditory System and Neural Representation of Conspecific Vocalizations." *Annual Review of Neuroscience* 32:315–46. doi: 10.1146/annurev.neuro.051508.135431.

Romanski, Lizabeth M., and Patricia S. Goldman-Rakic. 2002. "An Auditory Domain in Primate Prefrontal Cortex." *Nature Neuroscience* 5(1):15–16. doi: 10.1038/nn781.

Rudebeck, Peter H., and Elisabeth A. Murray. 2011a. "Balkanizing the Primate Orbitofrontal Cortex: Distinct Subregions for Comparing and Contrasting Values." *Annals of the New York Academy of Sciences* 1239:1–13. doi: 10.1111/j.1749-6632.2011.06267.x.

Rudebeck, Peter H., and Elisabeth A. Murray. 2011b. "Dissociable Effects of Subtotal Lesions within the Macaque Orbital Prefrontal Cortex on Reward-Guided Behavior." *Journal of Neuroscience* 31(29):10569–78. doi: 10.1523/JNEUROSCI.0091-11.2011.

Schall, Jeffrey D. 1997. "Visuomotor Areas of the Frontal Lobe." Pp. 527–638 in *Extrastriate Cortex in Primates*. Vol. 12, *Cerebral Cortex*, edited by K. S. Rockland, J. H. Kaas, and A. Peters. Boston, MA: Springer US.

Schlag, J., and M. Schlag-Rey. 1987. "Evidence for a Supplementary Eye Field." *Journal of Neurophysiology* 57(1):179–200. doi: 10.1152/jn.1987.57.1.179.

Schleicher, A., K. Amunts, S. Geyer, T. Kowalski, T. Schormann, N. Palomero-Gallagher, and K. Zilles. 2000. "A Stereological Approach to Human Cortical Architecture: Identification and Delineation of Cortical Areas." *Journal of Chemical Neuroanatomy* 20(1):31–47. doi: 10.1016/s0891-0618(00)00076-4.

Schleicher, A., N. Palomero-Gallagher, P. Morosan, S. B. Eickhoff, T. Kowalski, K. de Vos, K. Amunts, and K. Zilles. 2005. "Quantitative Architectural Analysis: A New Approach to Cortical Mapping." *Anatomy and Embryology* 210(5–6):373–86. doi: 10.1007/s00429-005-0028-2.

Schleicher, A., and K. Zilles. 1990. "A Quantitative Approach to Cytoarchitectonics: Analysis of Structural Inhomogeneities in Nervous Tissue Using an Image Analyser." *Journal of Microscopy* 157(Pt 3):367–81. doi: 10.1111/j.1365-2818.1990.tb02971.x.

Schleicher, Axel, Patricia Morosan, Katrin Amunts, and Karl Zilles. 2009. "Quantitative Architectural Analysis: A New Approach to Cortical Mapping." *Journal of Autism and Developmental Disorders* 39(11):1568–81. doi: 10.1007/s10803-009-0790-8.

Stanton, G. B., S. Y. Deng, M. E. Goldberg, and N. T. McMullen. 1989. "Cytoarchitectural Characteristic of the Frontal Eye Fields in Macaque Monkeys." *The Journal of Comparative Neurology* 282(3):415–27. doi: 10.1002/cne.902820308.

Uylings, H. B., K. Zilles, and G. Rajkowska. 1999. "Optimal Staining Methods for Delineation of Cortical Areas and Neuron Counts in Human Brains." *NeuroImage* 9(4):439–45. doi: 10.1006/nimg.1999.0417.

Vogt, Brent A., Patrick R. Hof, Karl Zilles, Leslie J. Vogt, Christina Herold, and Nicola Palomero-Gallagher. 2013. "Cingulate Area 32 Homologies in Mouse, Rat, Macaque and Human: Cytoarchitecture and Receptor Architecture." *The Journal of Comparative Neurology* 521(18):4189–4204. doi: 10.1002/cne.23409.

Walker, A. Earl. 1940. "A Cytoarchitectural Study of the Prefrontal Area of the Macaque Monkey." *Journal of Comparative Neurology* 73(1):59–86. doi: 10.1002/cne.900730106.

Watanabe, M. 1992. "Frontal Units of the Monkey Coding the Associative Significance of Visual and Auditory Stimuli." *Experimental Brain Research* 89(2):233–47. doi: 10.1007/BF00228241.

Wilson, Fraser A. W., Séamas P. Ó. Scalaidhe, and Patricia S. Goldman-Rakic. 1993. "Dissociation of Object and Spatial Processing Domains in Primate Prefrontal Cortex." *Science* 260(5116):1955–58. doi: 10.1126/science.8316836.

Xu, Ting, Darrick Sturgeon, Julian S. B. Ramirez, Seán Froudist-Walsh, Daniel S. Margulies, Charles E. Schroeder, Damien A. Fair, and Michael P. Milham. 2019. "Interindividual Variability of Functional Connectivity in Awake and Anesthetized Rhesus Macaque Monkeys." *Biological Psychiatry: Cognitive Neuroscience and Neuroimaging* 4(6):543–53. doi: 10.1016/j.bpsc.2019.02.005.

Yeo, B. T. Thomas, Fenna M. Krienen, Jorge Sepulcre, Mert R. Sabuncu, Danial Lashkari, Marisa Hollinshead, Joshua L. Roffman, Jordan W. Smoller, Lilla Zöllei, Jonathan R. Polimeni, Bruce Fischl, Hesheng Liu, and Randy L. Buckner. 2011. "The Organization of the Human Cerebral Cortex Estimated by Intrinsic Functional Connectivity." *Journal of Neurophysiology* 106(3):1125–65. doi: 10.1152/jn.00338.2011.

Yeterian, Edward H., Deepak N. Pandya, Francesco Tomaiuolo, and Michael Petrides. 2012. "The Cortical Connectivity of the Prefrontal Cortex in the Monkey Brain." *Cortex; a Journal Devoted to the Study of the Nervous System and Behavior* 48(1):58–81. doi: 10.1016/j.cortex.2011.03.004.

Zilles, K., N. Palomero-Gallagher, C. Grefkes, F. Scheperjans, C. Boy, K. Amunts, and A. Schleicher. 2002. "Architectonics of the Human Cerebral Cortex and Transmitter Receptor Fingerprints: Reconciling Functional Neuroanatomy and Neurochemistry." *European Neuropsychopharmacology: The Journal of the European College of Neuropsychopharmacology* 12(6):587–99.

Zilles, Karl, and Katrin Amunts. 2009. "Receptor Mapping: Architecture of the Human Cerebral Cortex." *Current Opinion in Neurology* 22(4):331–39. doi: 10.1097/WCO.0b013e32832d95db.

Zilles, Karl, Maraike Bacha-Trams, Nicola Palomero-Gallagher, Katrin Amunts, and Angela D. Friederici. 2015. "Common Molecular Basis of the Sentence Comprehension Network Revealed by Neurotransmitter Receptor Fingerprints." *Cortex; a Journal Devoted to the Study of the Nervous System and Behavior* 63:79–89. doi: 10.1016/j.cortex.2014.07.007.

Zilles, Karl, and N. Palomero-Gallagher. 2017. "Comparative Analysis of Receptor Types That Identify Primary Cortical Sensory Areas." Pp. 225–45 in.

Zilles, Karl, and Nicola Palomero-Gallagher. 2017. "Multiple Transmitter Receptors in Regions and Layers of the Human Cerebral Cortex." *Frontiers in Neuroanatomy* 11:78. doi: 10.3389/fnana.2017.00078.

Supplementary Figures

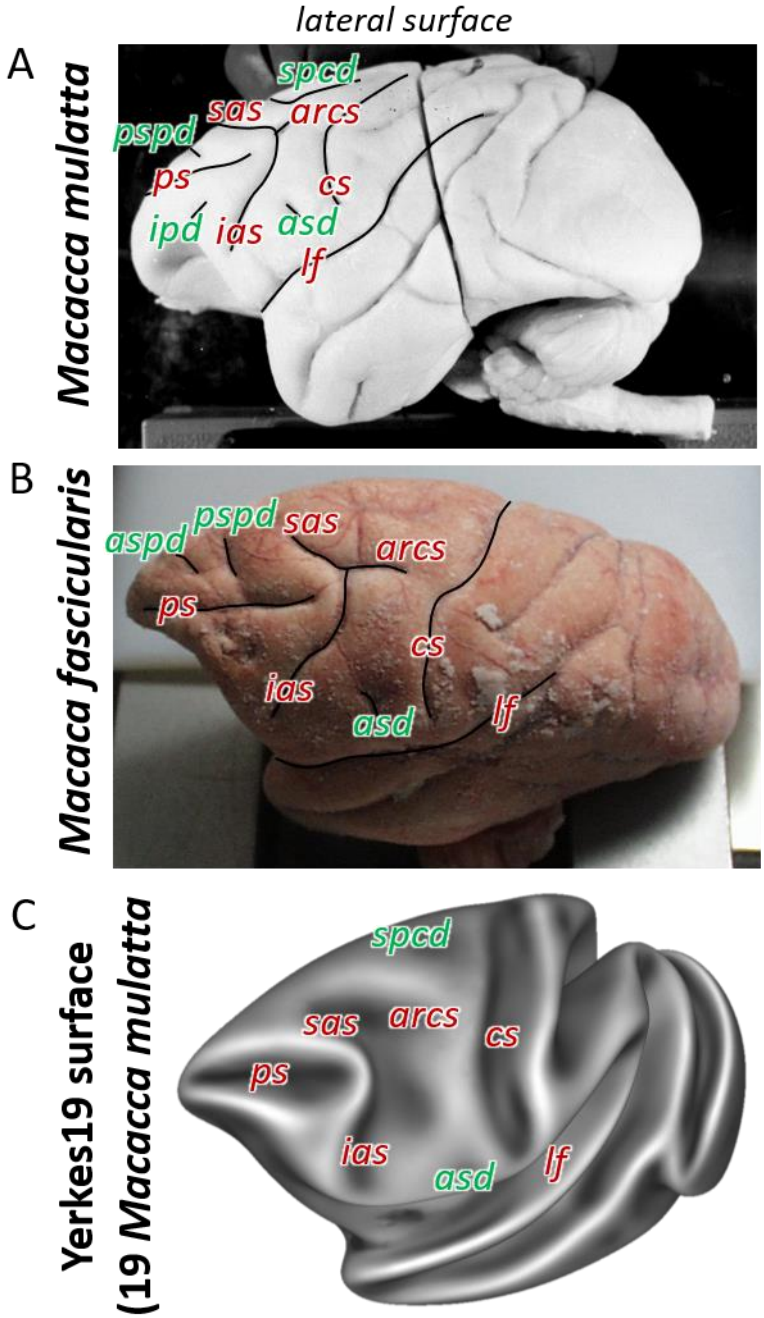

Supplementary Figure 1. Macroanatomical landmarks (sulci labelled in red letters and dimples in green) shown on the lateral surface of the two related species of macaque monkey used in the present architectonic analyses. Photographs of two of the post mortem brains used in the present study. Brain ID DP1 (A; *Macaca mulatta*), and brain ID 11530 (B; *Macaca fascicularis*). Average surface representations of the Yerkes 19 (C) *Macaca mulatta* template brains. arcs – spur of the arcuate sulcus; asd – anterior supracentral dimple; aspd – anterior superior principal dimple; cs – central sulcus; ias – inferior arcuate sulcus; ps – principal sulcus; pspd – posterior superior principal dimple; sas – superior arcuate sulcus; spcd – superior precentral dimple.

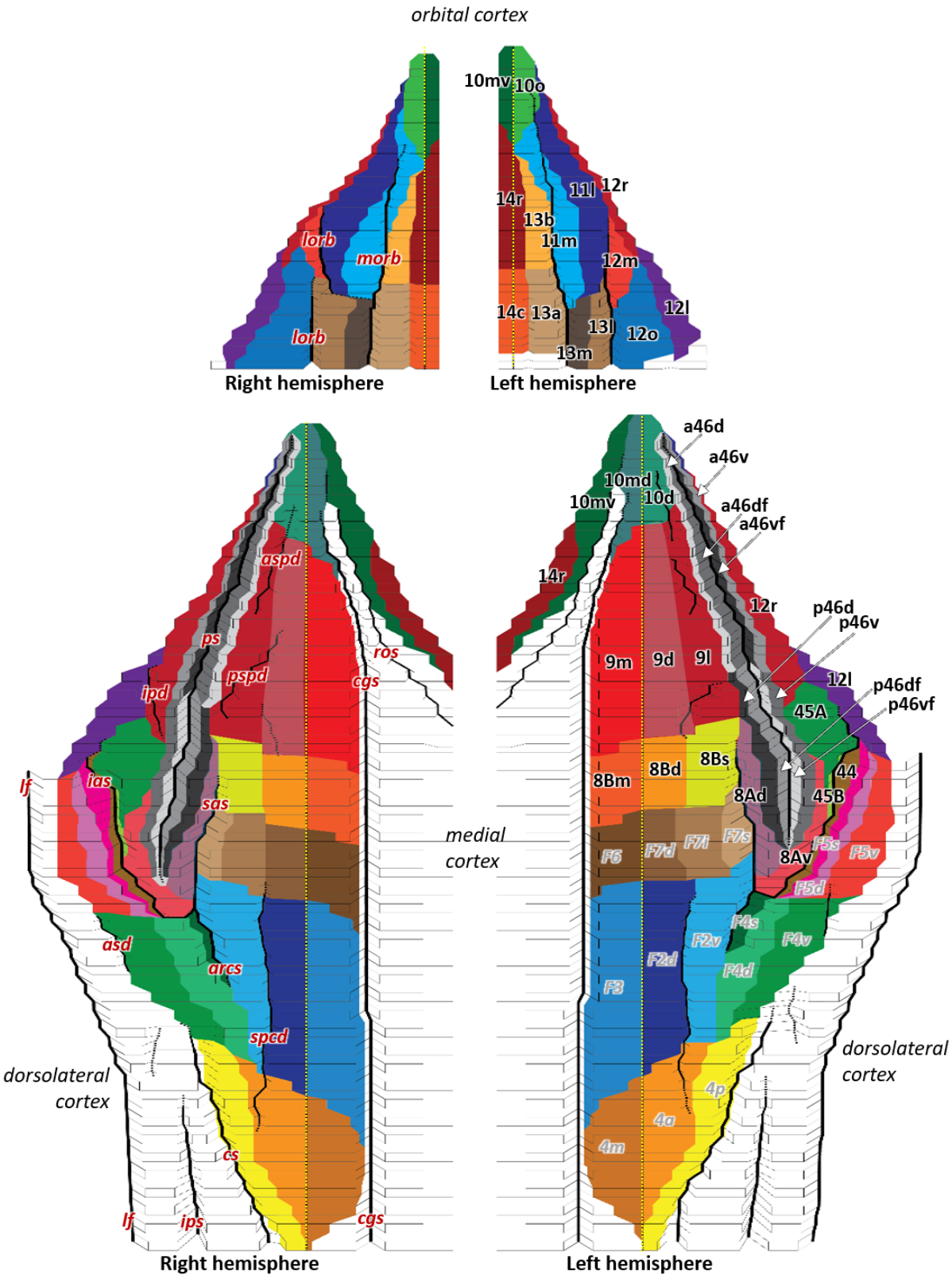

Supplementary Figure 2. 2D flat map, based on the macroanatomical landmarks of every 40th section, displays orbital, medial and dorsolateral hemispheric views with all defined areas within the macaque frontal lobe. Areas are labelled on the left hemisphere i.e., prefrontal areas in black and, previously mapped (pre)motor areas (Rapan et al. 2021a) in gray. Due to limited space on the map, we used white

arrows to mark anterior and posterior subdivisions of 46. Dashed yellow line on the hemispheres represents the midline, which separates medial and dorsolateral cortex. Black full lines mark the fundus of sulci. Macroanatomical landmarks are marked on the right hemisphere; arcs – spur of the arcuate sulcus; asd – anterior supracentral dimple; aspd – anterior superior principal dimple; cgs – cingulate sulcus; cs – central sulcus; ias – inferior arcuate sulcus; lf – lateral fissure; lorb – lateraral orbital sulcus; morb – medial orbital sulcus; ps – principal sulcus; pspd – posterior superior principal dimple; sas – superior arcuate sulcus; spcd – superior precentral dimple.

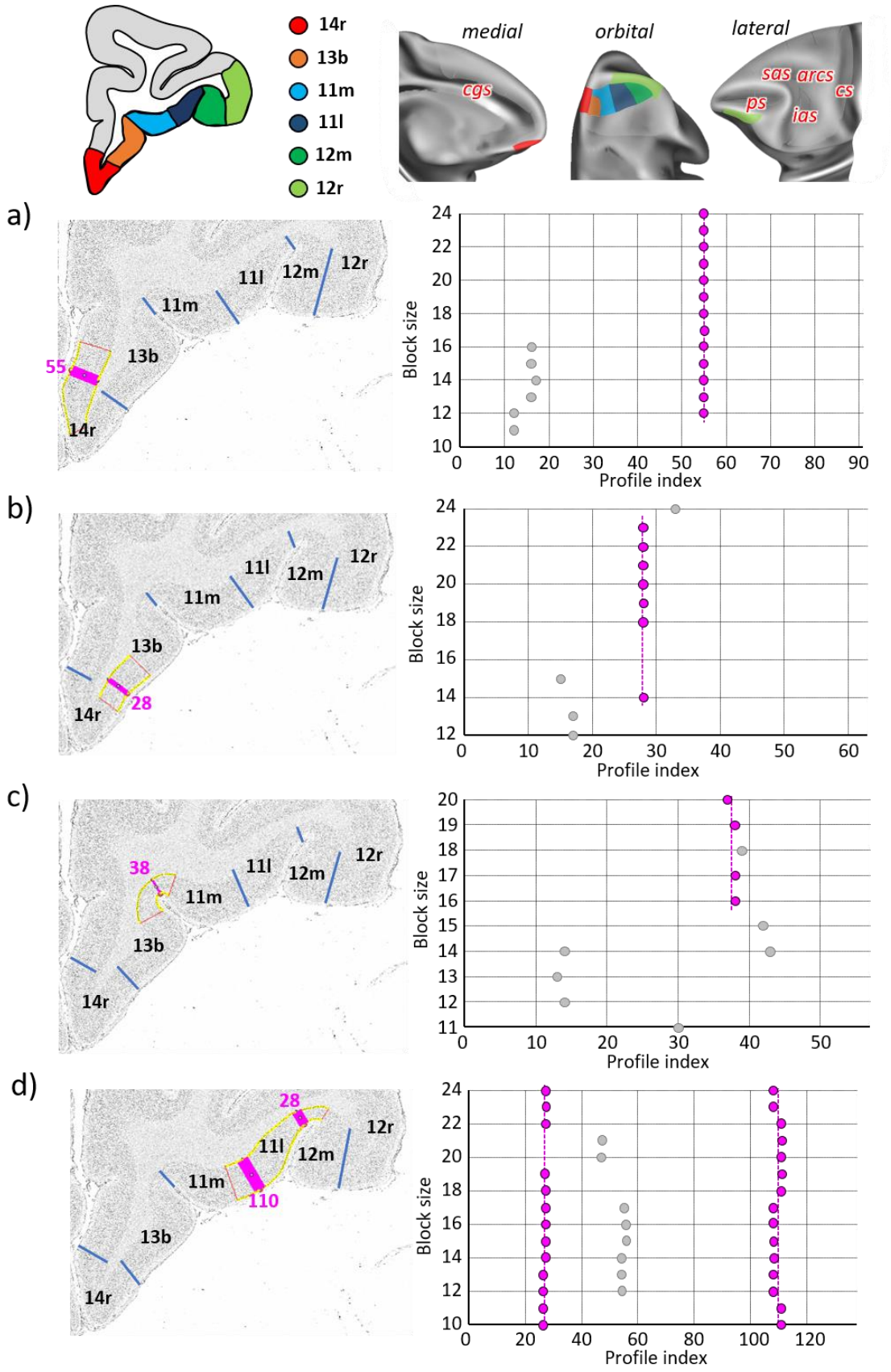

Supplementary Figure 3. Statistically testable borders confirmed by the quantitative analysis for the rostral orbital and ventrolateral areas 14r, 13b, 11m, 11l, 12m and 12r. For details see Fig. 3

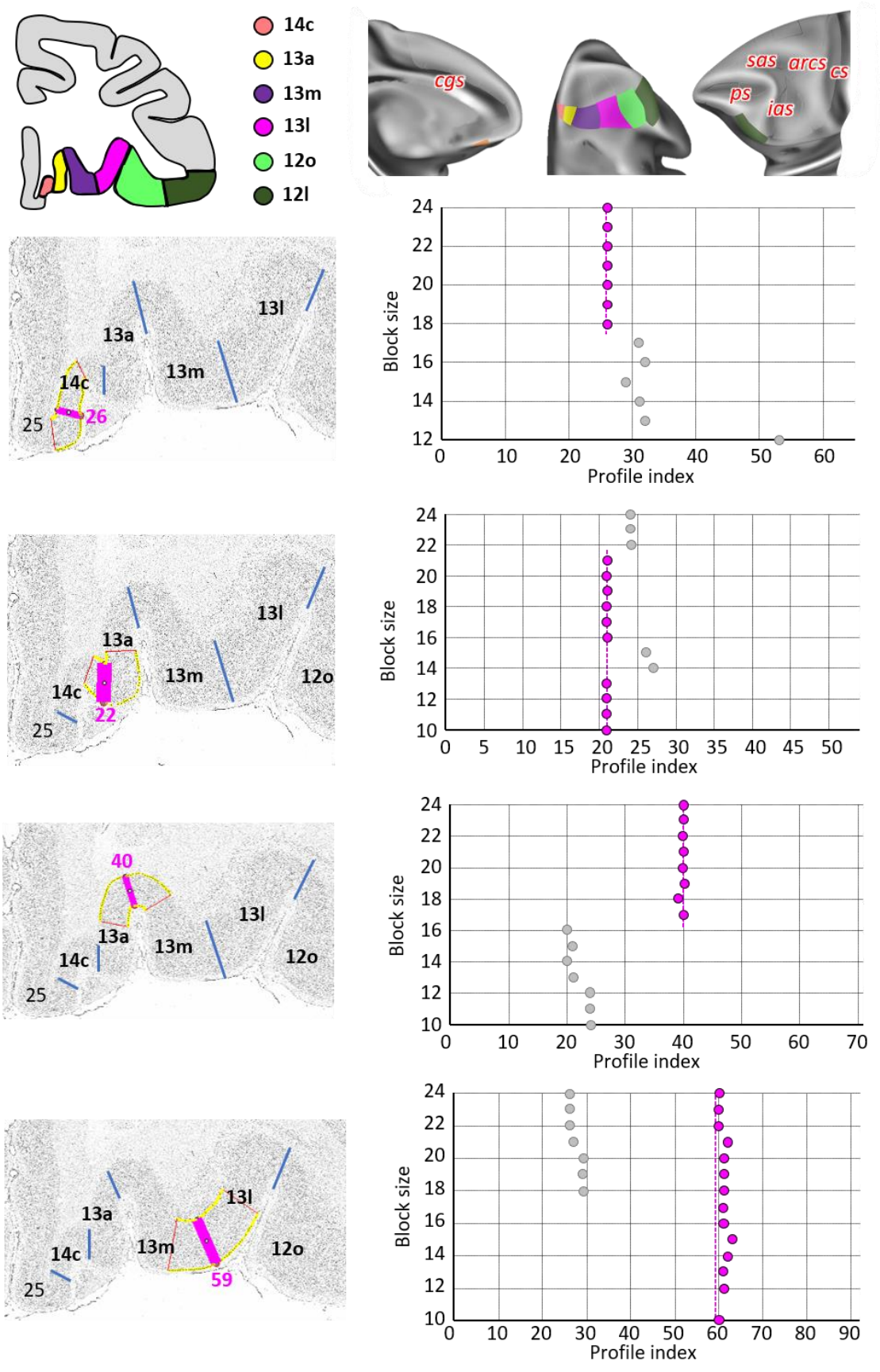

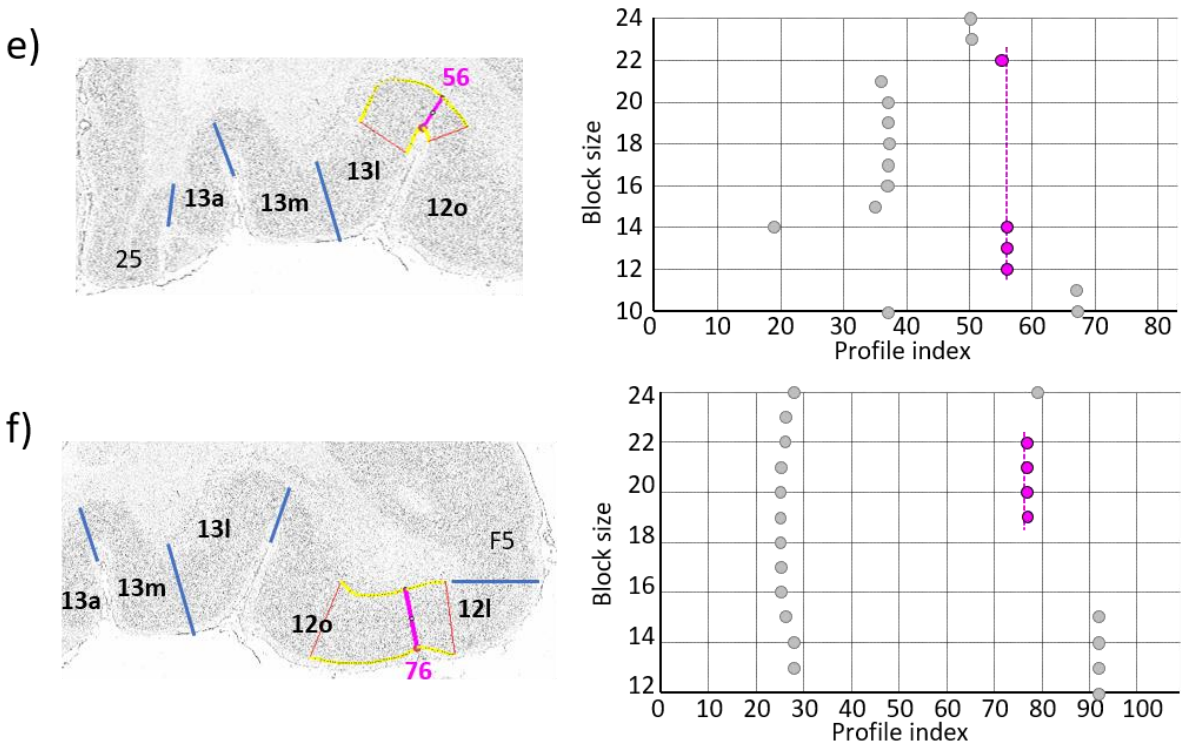

Supplementary Figure 4. Statistically testable borders confirmed by the quantitative analysis for the caudal orbital and ventrolateral areas 14c, 13a, 13m, 13l and 12o. For details see Fig. 3

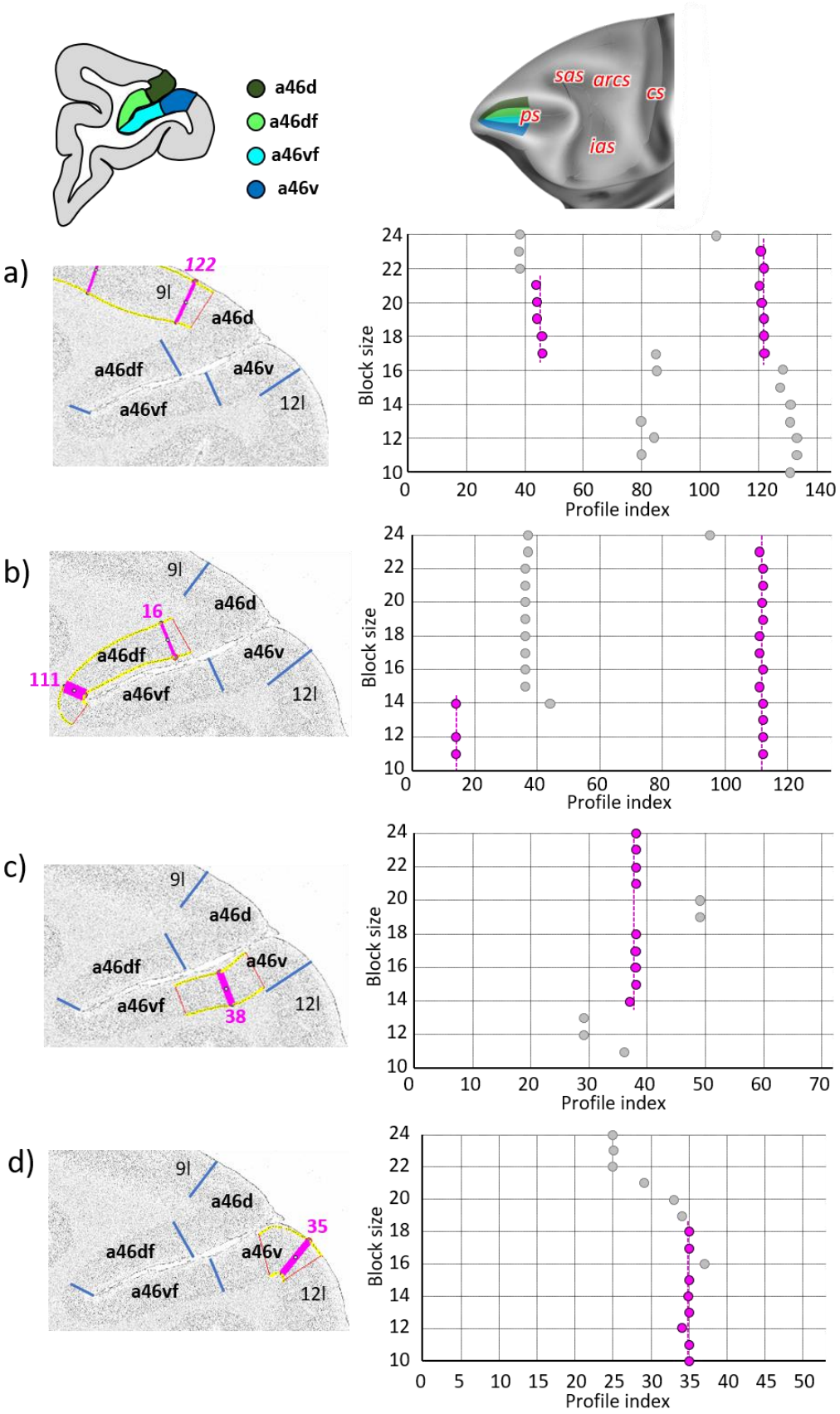

Supplementary Figure 5. Statistically testable borders confirmed by the quantitative analysis for the rostral region of the ps, occupied by the anterior subdivisions of area 46; a46d, a46df, a46vf and a46v. For details see Fig. 3

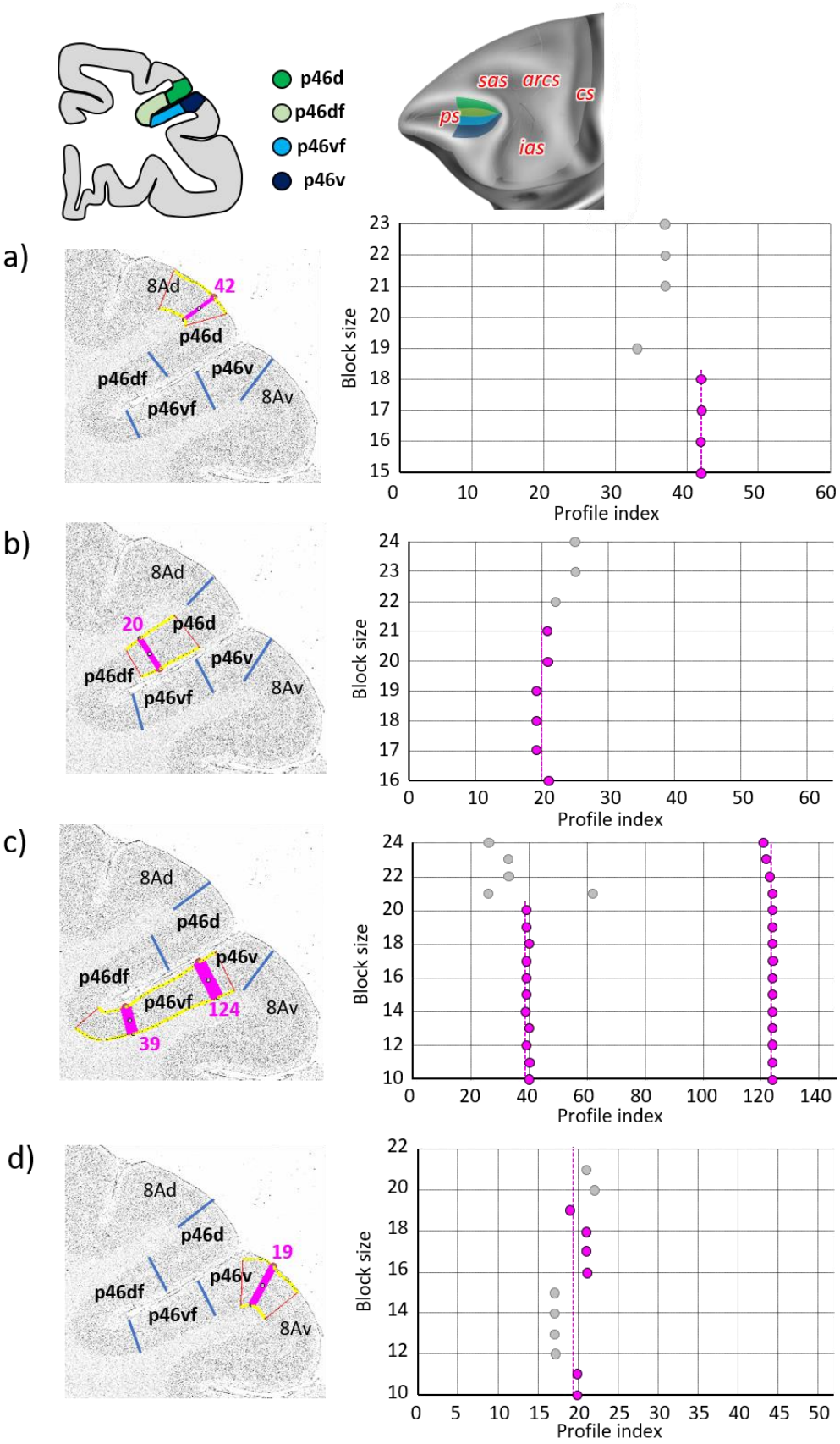

Supplementary Figure 6. Statistically testable borders confirmed by the quantitative analysis for the caudal region of the ps, occupied by the posterior subdivisions of area 46; p46d, p46df, p46vf and p46v. For details see Fig. 3

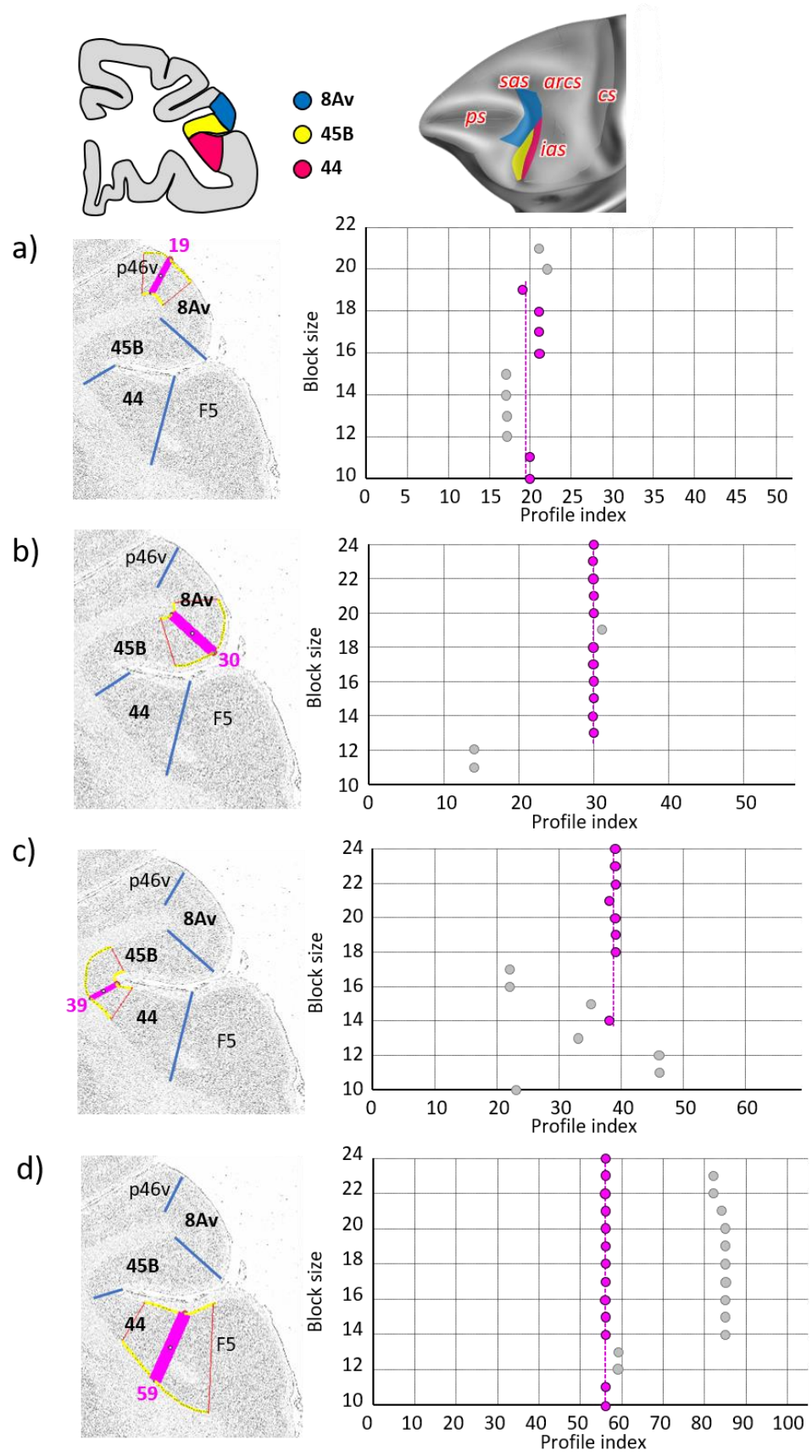

Supplementary Figure 7. Statistically testable borders confirmed by the quantitative analysis for the caudal ventrolateral cortex; areas 8Av, 45B and 44. For details see Fig. 3

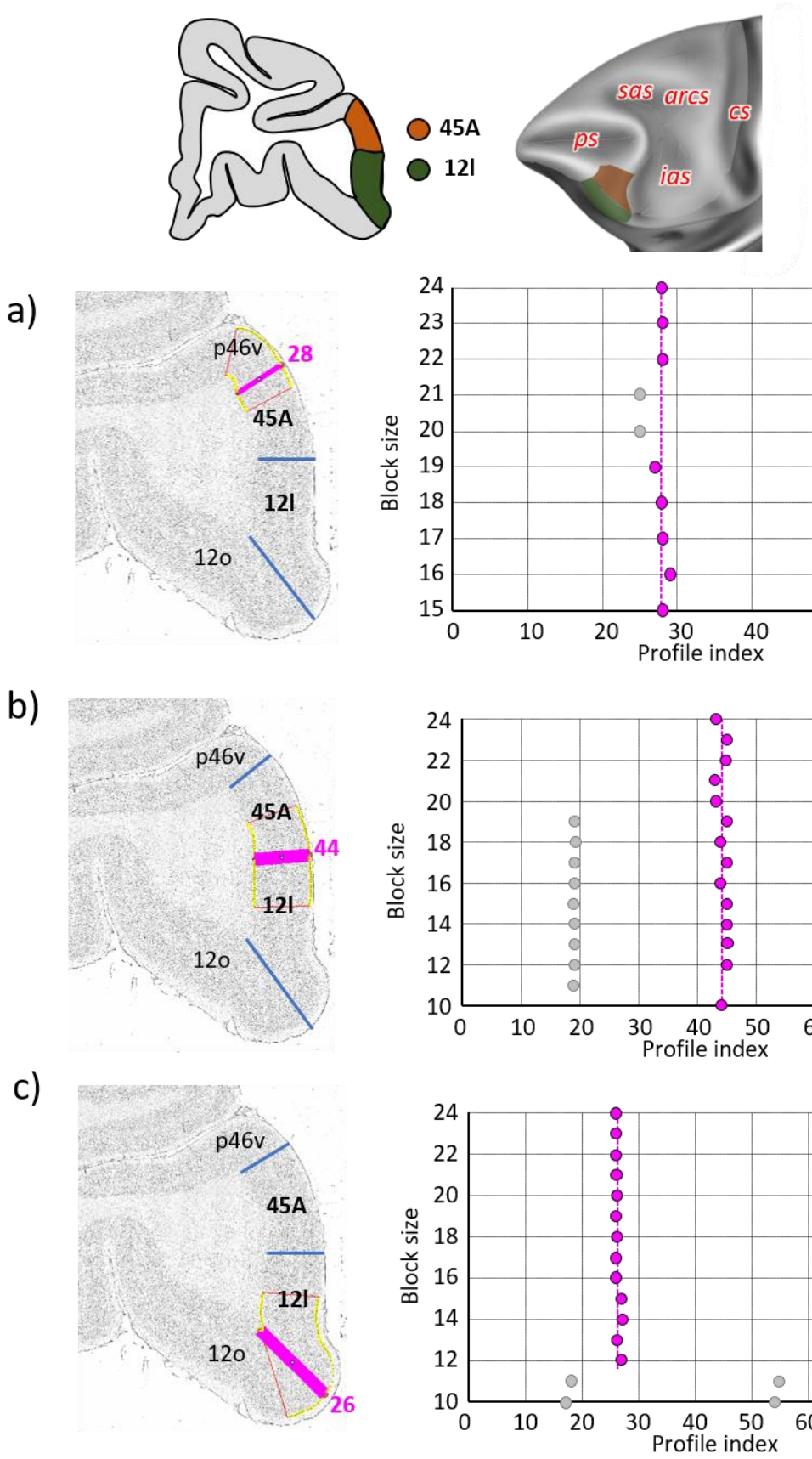

Supplementary Figure 8. Statistically testable borders confirmed by the quantitative analysis for the caudal ventrolateral area 12l and dorsally adjacent area 45A. For details see Fig. 3

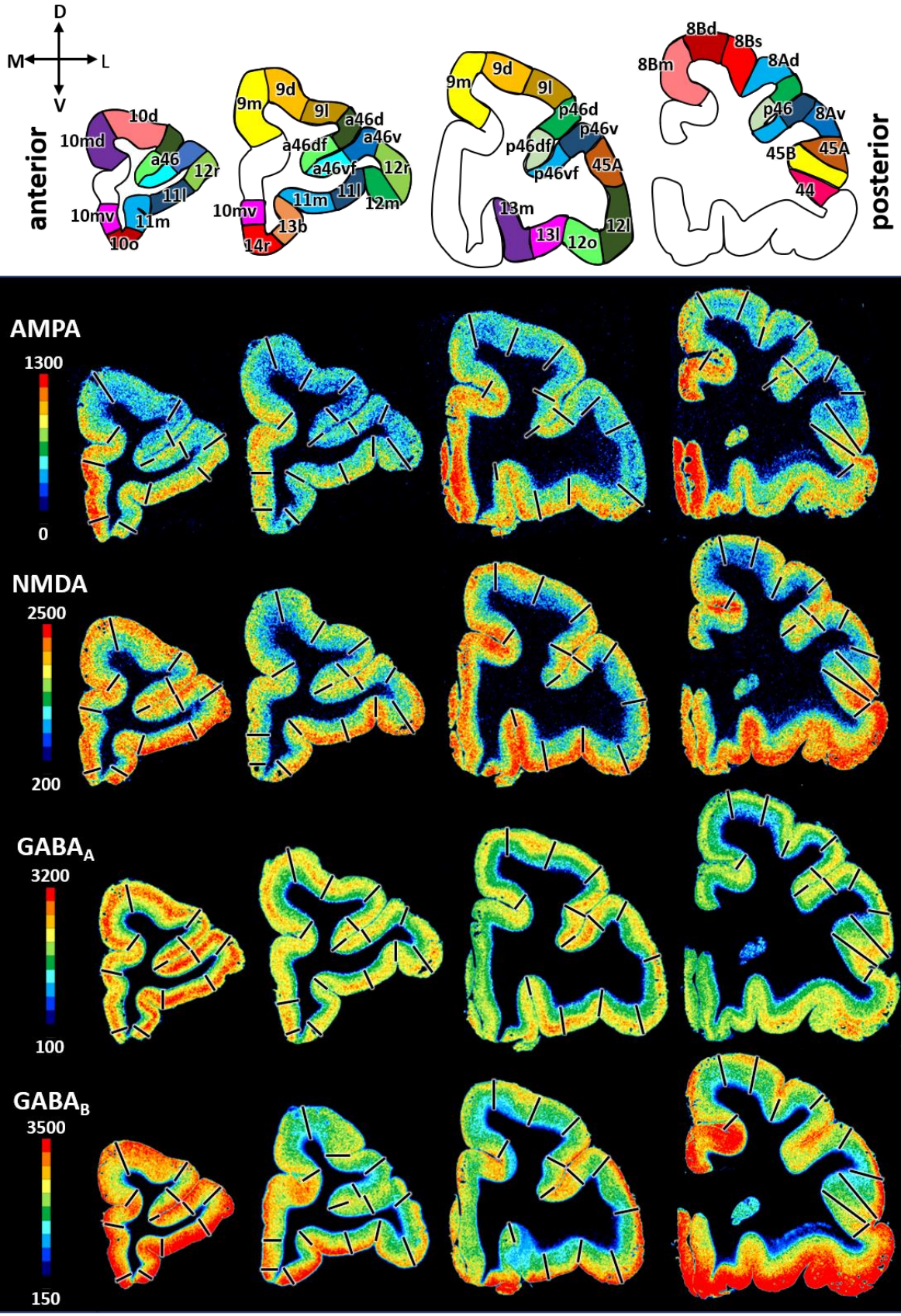

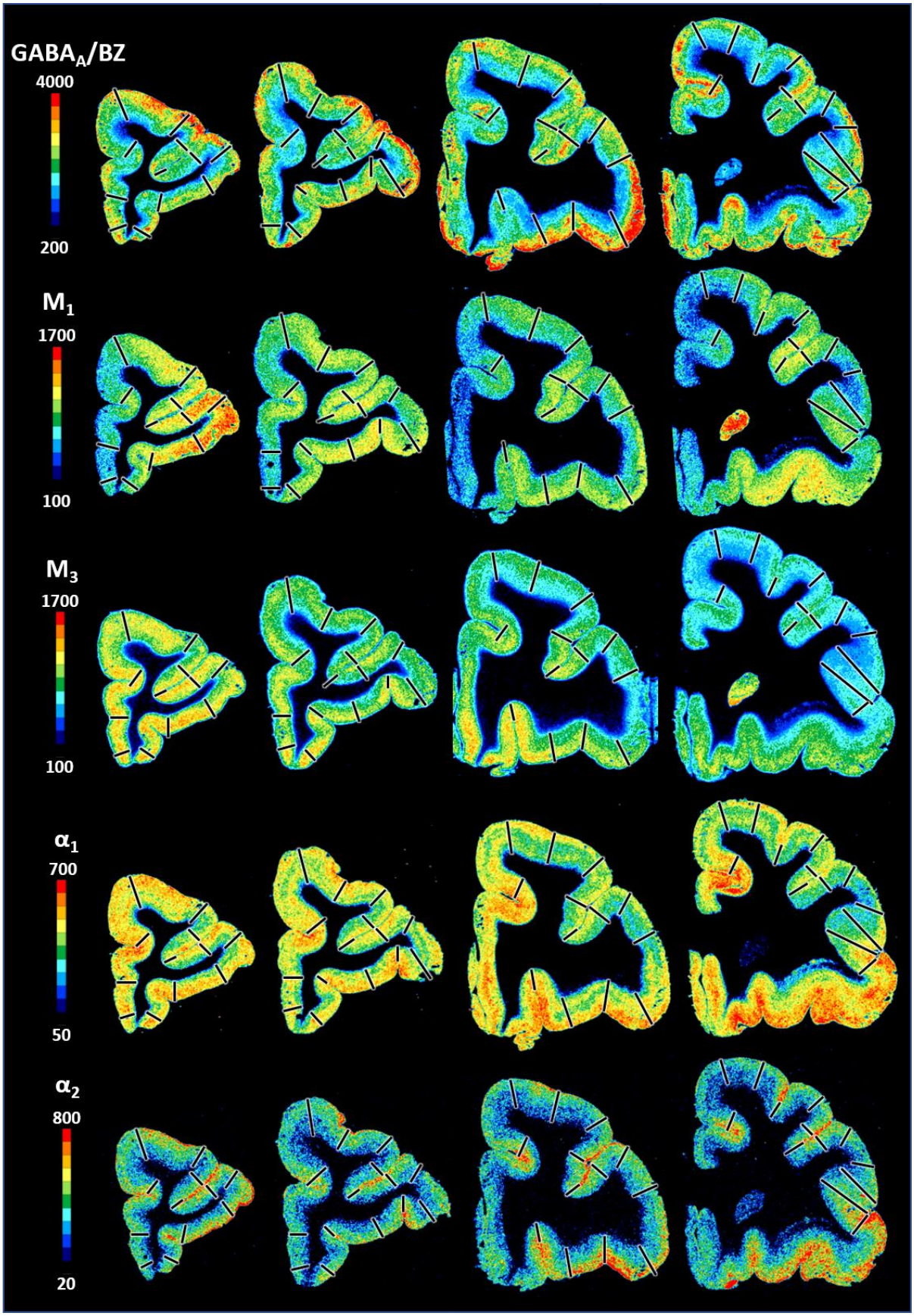

Supplementary Figure 9. Exemplary sections depicting the distribution of the remaining of the receptors that are not shown in Fig. 9, i.e., AMPA, NMDA, $GABA_A$, $GABA_B$, $GABA_A$/BZ, M_1, M_3, α_1, α_2, $5HT_2$ and D_1 receptors in coronal sections through a macaque hemisphere. The color bar positioned left to the autoradiographs codes values of receptor densities in fmol/mg protein and borders are indicated by the black lines. The four schematic drawings at the top represent the distinct rostro-caudal levels and show the position of all prefrontal areas defined. C – caudal; D – dorsal; R – rostral; V – ventral.

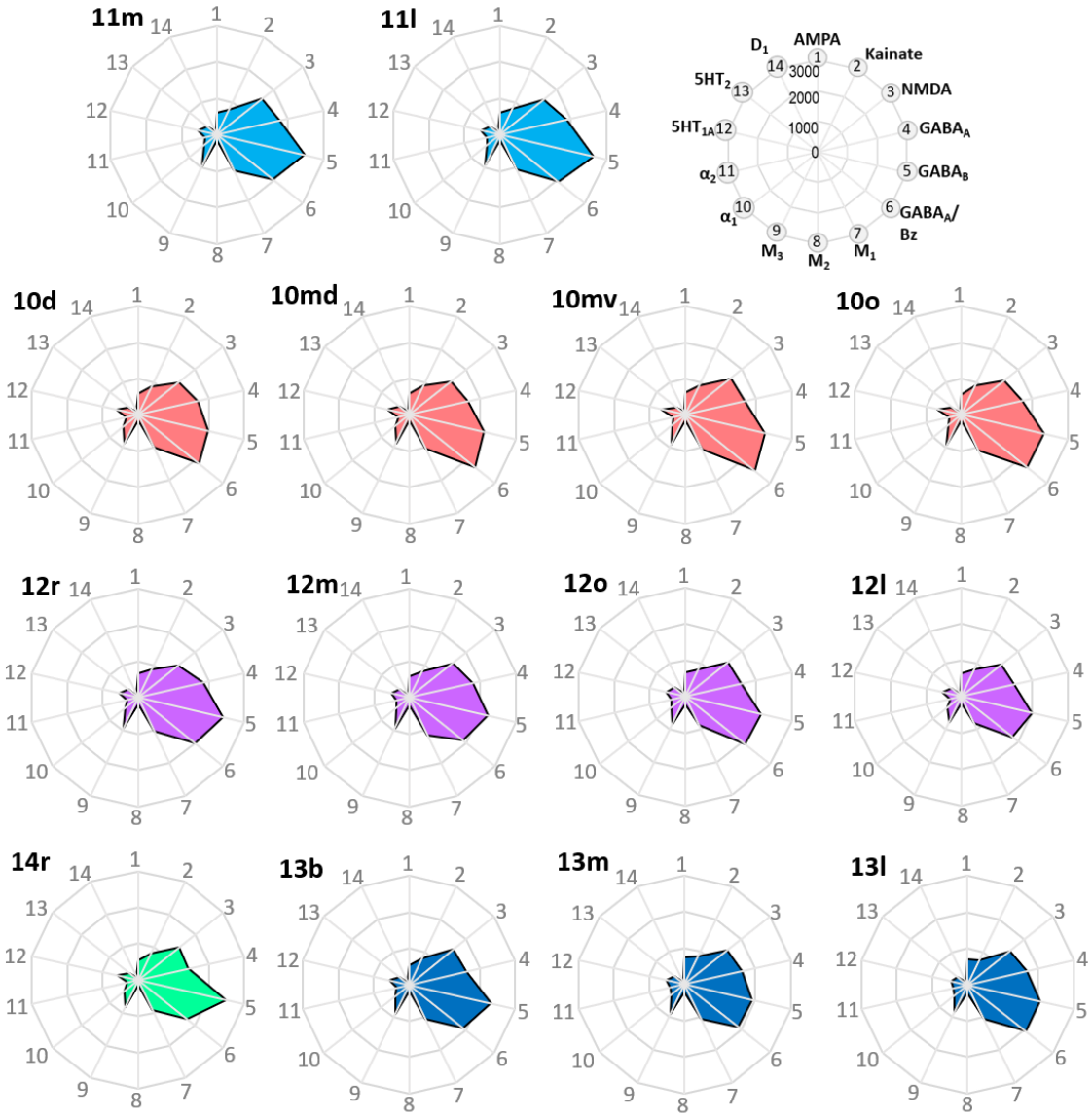

Supplementary Figure 10. Receptor fingerprints of the frontopolar and orbital areas. Absolute receptor densities are given in fmol/mg protein. The positions of the different receptor types and the axis scaling are identical in all areas, and specified in the polar plot on the top of the figure.

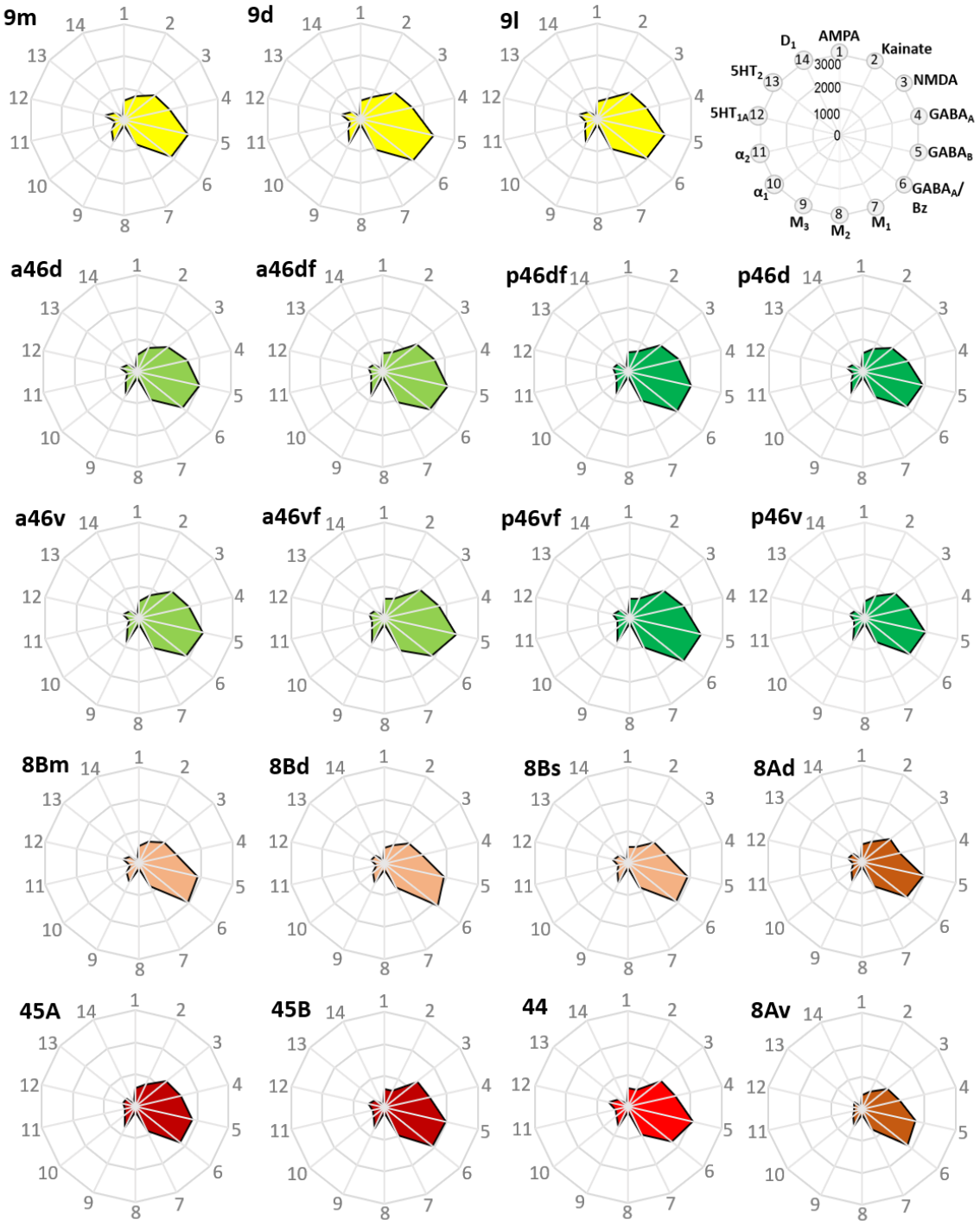

Supplementary Figure 11. Receptor fingerprints of the medial, dorsolateral, lateral and ventrolateral areas. Absolute receptor densities are given in fmol/mg protein. The positions of the different receptor types and the axis scaling are identical in all areas, and specified in the polar plot on the top of the figure.

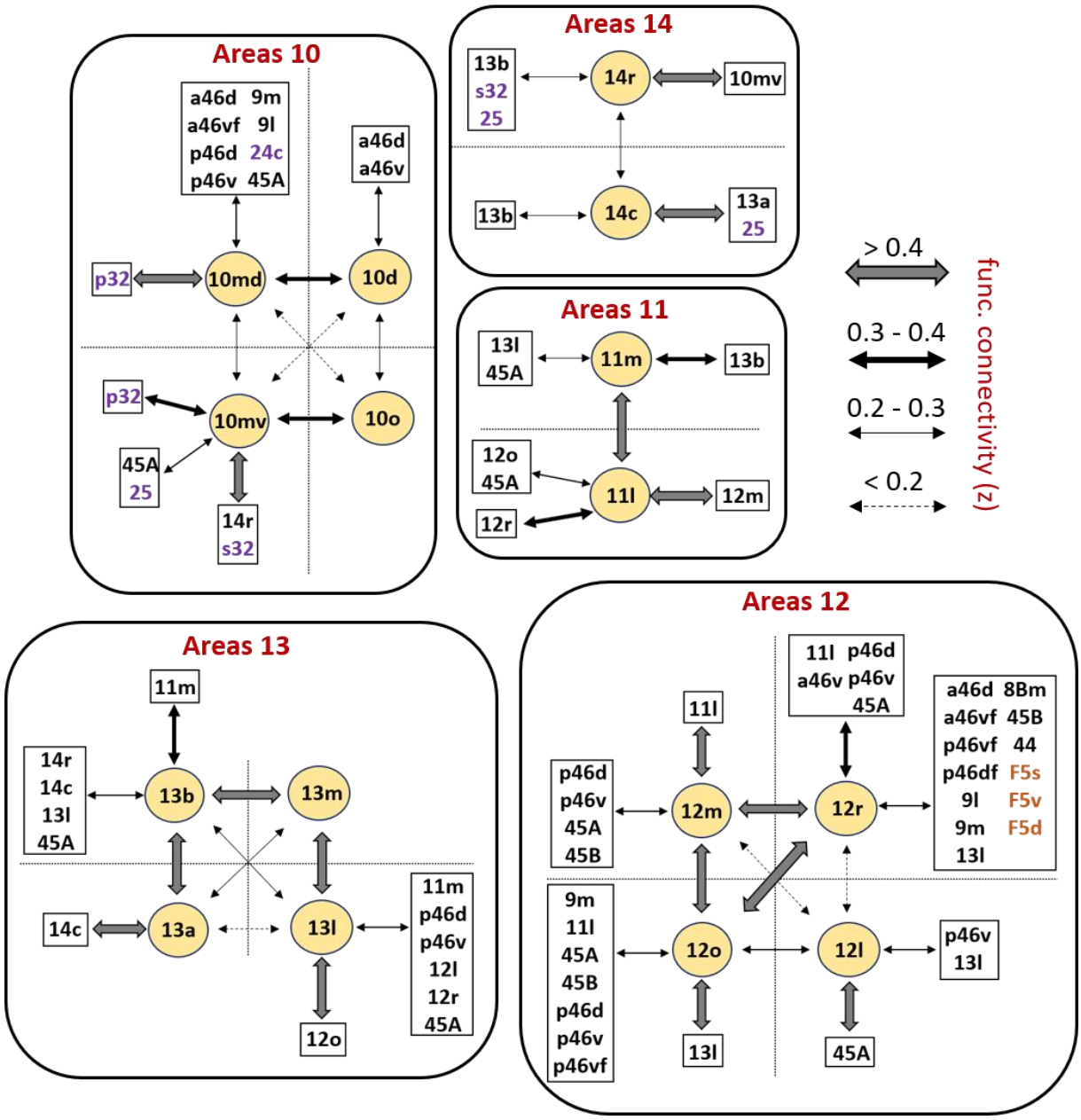

Supplementary Figure 12. Schematic summary of the functional connectivity analysis between subdivisions of areas 10, 14, 11, 13 and 12. The strength of the functional connectivity coefficient (z) is coded by the appearance (wider-thinner-doted) of the connecting arrows.

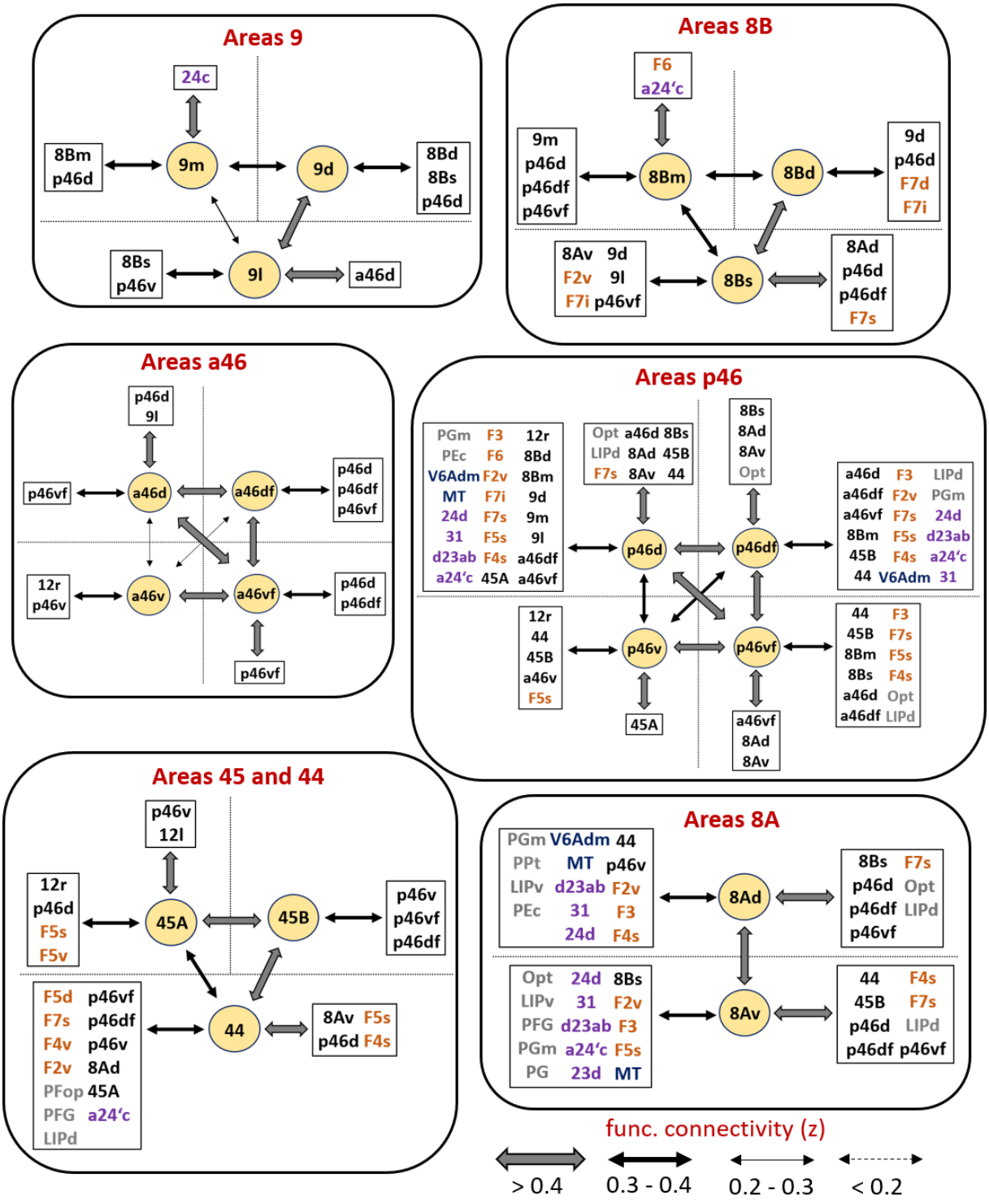

Supplementary Figure 13. Schematic summary of the functional connectivity analysis between subdivisions of areas 9, 8B, 8A, 46, 45 and 44. The strength of the functional connectivity coefficient (z) is coded by the appearance (wider-thinner-doted) of the connecting arrows.